Nonlinear analysis of the model for thermoacoustic instability involving vortex shedding

Mechanical engineering

Intelligent structures and mechanics system engineering

Tokushima University

Wei Wang

Supervisor: Prof. Yoshihiro Deguchi

September 2021

Abstract

In engineering, the combustion chamber with a backward-facing step is very popular, and it is a kind of flame stabilizer. In this type of combustion chamber, there will be shedding vortices at the step due to the instability of the flow field. The shedding vortices will carry reactants to move downstream and burn, resulting in unstable heat release and then pressure and velocity fluctuations of the acoustic field, thereby, finally, forming a combustion-vortex-acoustic interaction process. If a positive feedback loop is formed between the unstable heat release and the pressure fluctuation of acoustic field, combustion instability will occur, and it is also referred to as thermoacoustic oscillation due to vortex shedding. Combustion instability frequently occurs in many practical systems or equipment, and its induced significant pressure oscillations have a serious influence on the normal operation of the equipment. Recently, the combustion instability has been extensively studied experimentally, but the theoretical investigation on its nature is still rare. Since combustion instability is a complicated nonlinear phenomenon, it is necessary to study its nature from the viewpoint of nonlinear dynamics.

Based on the one-dimensional simplified model of thermoacoustic instability involving vortex shedding proposed by Matveev and Culick, the typical nonlinear phenomenon in thermoacoustic oscillation induced by vortex shedding is studied. The study focuses on the initial value sensitivity of the system, the influence of key parameters on thermoacoustic oscillation, and the phenomenon of vortex-acoustic lock-in. Firstly, the Galerkin method is used to approximate the governing equation, and the partial differential equations are reduced to a set of ordinary differential equations. Then, the first ten modes are selected, and the pressure and velocity fluctuations of sound field under different system parameters are obtained by MATLAB program. Finally, the thermoacoustic instability of the system under different initial disturbances, the influences of different steady flow velocity on the thermoacoustic oscillation of the

system, and the phenomenon of vortex-acoustic lock-in in thermoacoustic oscillation are studied in detail. Furthermore, the influences of fluctuation of upstream velocity in combustor on the thermoacoustic oscillation is studied. Besides, the influences of external harmonic excitation on the thermoacoustic system is also studied.

The results show that the system of thermoacoustic oscillation involving vortex shedding is extremely sensitive to initial values, and there are a rich variety of nonlinear phenomena. With steady flow velocity increasing, the amplitude of pressure fluctuation augments generally. However, the similar structures are found in several intervals of steady flow velocity, and the amplitude first decreases and then increases. In particular, it is verified that the system oscillates periodically by integer (f_p/f_s) multiple of the vortex impinging frequency (f_s), that is, the vortex-acoustic frequency locking with the number of revolutions f_p/f_s, which is found in experiment and can be regarded as an important characteristic of periodic thermoacoustic oscillation. Furthermore, the thermoacoustic oscillation of the system can be controlled by the fluctuation of mainstream velocity. When the frequency of fluctuating mainstream velocity is positive integer times of the frequency of steady vortex shedding, the intensity of the thermoacoustic oscillation is significantly weaker than that when the mainstream velocity is stable. Besides, the thermoacoustic oscillation of the system has periodic and quasi-periodic solutions under external sinusoidal excitation. And the thermoacoustic oscillation of the system can be controlled by choosing the frequency and amplitude of the external excitation reasonably. In a word, the phenomenon of thermoacoustic instability and the mechanism of vortex-acoustic lock-in are studied theoretically based on nonlinear dynamics, which is of great significance to avoid the harm of thermoacoustic oscillation and make rational use of it.

KEY WORDS： Combustion instability, Thermoacoustic oscillation, Vortex shedding, Vortex-acoustic lock-in, Nonlinear dynamics

TYPE OF THESIS： Theoretical research

Contents

Chapter 1 Introduction

1.1 Background of the study

The combustion of reactants in a confined volume may be accompanied by the development of significant pressure oscillations. If these pressure oscillations occur as a result of unsteady heat release, the phenomenon is often referred to as combustion instability. Combustion instability occurs in many practical systems, such as power plants, jet engine afterburners, and rocket engines. These instabilities are spontaneously excited by a feedback loop between an oscillatory combustion process and one of the natural acoustic modes of the combustor. In general, the occurrence of combustion instabilities in different kinds of combustors will bring many plaguing problems, for example, the large-amplitude pressure and velocity oscillations will lead to the thrust oscillations of jet engine, the severe vibrations will disturb the operation of the control system, combustion oscillations will increase the thermal stresses on the combustion chamber walls, combustion oscillations will increase the mechanical loads and lead to low cycle or high cycle fatigue of system components, and combustion oscillations may lead to the flameout or flame flashback of combustion chamber [1-3]. These phenomena can lead to premature wear of components, which can lead to catastrophic system or component damage. Therefore, over the past few decades, a great deal of research and development work has been undertaken to clarify the processes that cause these instabilities and to develop ways to prevent them.

The mechanism of combustion instability was explained in reference [1]. Figure 1.1 summarizes the conditions required for a combustion instability to spontaneously occur. The upper portion of Fig. 1.1 shows an unstable combustion chamber with reactants entering from the left and combustion products exiting from the nozzle on the right. The interaction between one of the acoustic mode of the combustion chamber and the heat release oscillations transfers or removes energy from the acoustic mode. The combustion process adds (or removes) energy from the acoustic oscillations locally

depending on the positive (or negative) of the integral in Fig. 1.1, which is often referred to as Rayleigh's integral [4]. The sign of the Rayleigh's integral depends on the phase difference between the heat release and pressure oscillations, and is positive (negative) when the phase difference is less than (greater than) 90 degrees. As shown in Fig. 1.1, combustion instability spontaneously occurs only when the energy provided to the acoustic mode by the combustion process exceeds the energy losses of the mode caused by, such as the radiation and convection of acoustic energy, viscous dissipation and heat transfer. Therefore, as long as the amplitude of the driving exceeds the amplitude of the damping process, the energy of the mode will increase with time. When this occurs, the amplitude of the oscillation initially increases exponentially with time until it saturates at a certain limit cycle oscillation. In this case, the time averages of the driving and damping processes are equal, and no net energy is added to the oscillating process, which is a self-excited oscillation process [1].

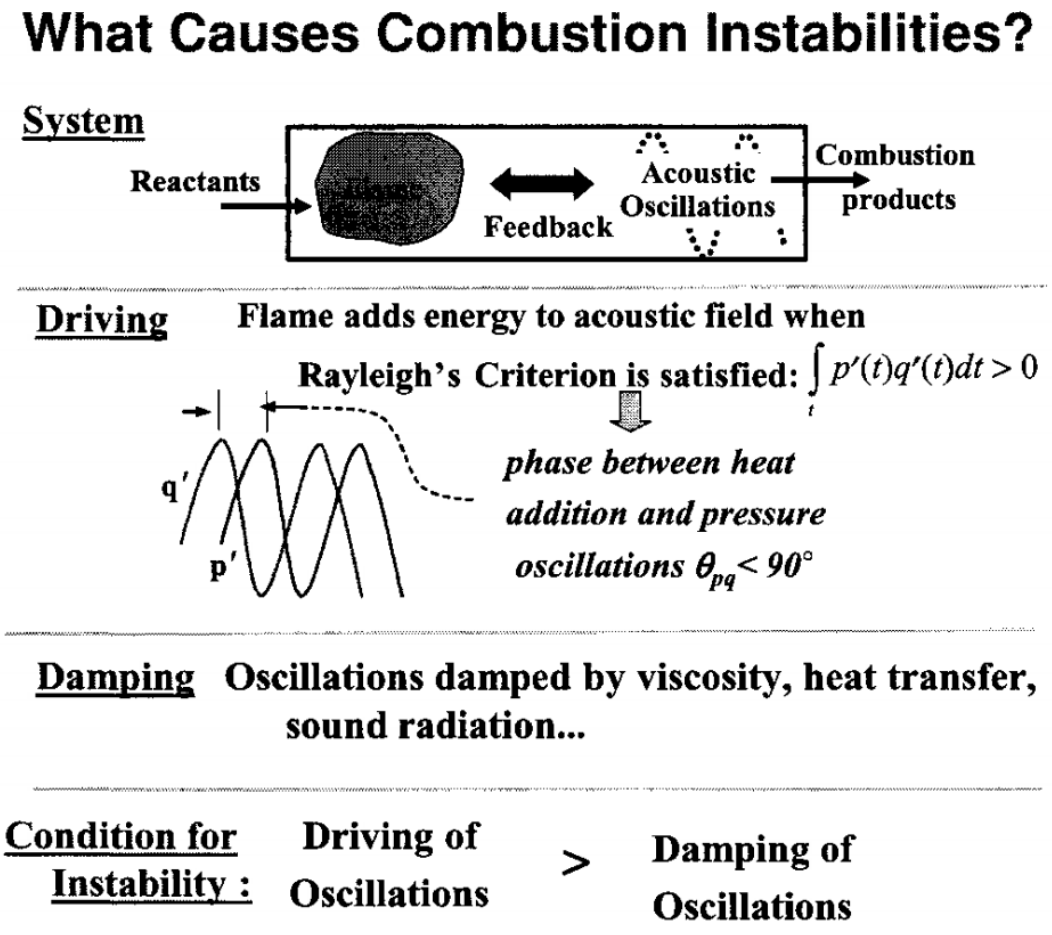

Fig. 1.1 Summary of conditions required for a combustion instability to occur [1].

Combustion instabilities are characterized by rapid fluctuations of heat release and pressure, and large-amplitude oscillations of one or more natural acoustic modes of the combustor [1]. Fluctuations in heat release rate arise due to acoustic fluctuations. Combustion instability is caused when the fluctuating heat release rate and the acoustic field form a positive feedback loop [5], that is, the unstable heat release induced by the combustion of reactant lead to the oscillation of acoustic field, and the oscillation of acoustic field in turn strengthens the fluctuation of heat release, thus forming a positive feedback loop. Because in all cases of combustion instabilities, the acoustic oscillations are excited by thermal sources, the resulting phenomena are often referred to as thermoacoustic instabilities or thermoacoustic oscillations.

Actually, thermoacoustic oscillations are complex phenomena dominated by nonlinear processes. Since the initial amplitudes of most instabilities are usually quite small, their properties can be described by the linear wave equation [6].The frequencies and mode shapes of these oscillations and the conditions for their spontaneous occurrence are determined by the solution of these equations. However, linear analysis cannot predict the magnitude of the limit cycle amplitude attained by the instability, because it is controlled by nonlinear process. In addition, nonlinear processes may allow large-amplitude perturbations whose amplitude exceeds a certain threshold value to trigger the instability of linear stable systems. Therefore, both the characteristics of the limit cycle oscillation and the conditions for the instability triggered by the finite amplitude perturbations can only be determined by solving the nonlinear equations describing the dynamics of the system [7, 8]. Although the Rayleigh's criterion and linear analysis can be used to explain the mechanism of occurrence and maintain of thermoacoustic oscillation, the state of the system after the instability cannot be predicted, and the complex nonlinear phenomena such as mode coupling, frequency lock-in, hysteresis, bifurcation and chaos which may exist in the thermoacoustic oscillation cannot be analyzed. Therefore, it is necessary to use the analysis method based on nonlinear dynamics to study the phenomenon of thermoacoustic instability and reveal the mechanism of its occurrence and development, which is of great

significance to avoid the harm of thermoacoustic oscillation and make rational use of it.

1.2 Overview of previous research

Thermoacoustic instability is a complex phenomenon, and some simplified models must be used to understand its nature. In 1850, Sondhauss first discovered the thermoacoustic phenomenon and designed the Sondhauss tube to demonstrate it. In 1859, Rijke designed the Rijke tube to better demonstrate the thermoacoustic phenomenon, and the Rijke tube gradually became the most convenient and classic model to study the thermoacoustic instability both experimentally and theoretically. After that, many scholars have carried out a lot of studies on the thermoacoustic oscillation based on this model, including some studies using the analysis method based on nonlinear dynamics. Balasubramanian and Sujith [9] investigated the role of non-normality and nonlinearity in thermoacoustic interaction based on a one-dimensional Rijke tube model. Subramanian et al. [10] carried out bifurcation analysis on the dynamical behavior of a horizontal Rijke tube model. They obtained the bifurcation diagrams including the amplitude of the unstable limit cycles by using the method of numerical continuation, and analyzed the subcritical bifurcation for variation of parameters and regions of global stability, global instability and bistability. Dang Nannan et al. [11] numerically studied the relationship between the stability switching behavior of thermoacoustic oscillation and the time delay of heat transfer in Rijke tube under two different acoustic damping cases, namely the heavily damped case and the weakly damped case.

With the above background, this study is based on the model of a Rijke tube with a backward-facing step, which is a kind of flame stabilizer, and is very common in the actual combustion chambers. As early as 1956, Rogers and Marble [12] conducted an experimental study on a small two-dimensional combustion chamber. They observed the periodic vortex shedding at the edge of the flame stabilizer accompanied by high-frequency oscillation, and proposed the mechanism of oscillation. After that, many

scholars studied the role of vortex shedding in thermoacoustic oscillation through a large number of experiments [13-17]. Meanwhile, with the development of computational fluid dynamics (CFD) technology, scholars began to use CFD software to simulate the process of combustion-vortex-acoustic interaction [18, 19]. Nowadays, Large Eddies Simulation (LES) has become the most powerful tool for numerical simulation of combustion process and combustion instability [20-22].

At present, the research on the thermoacoustic oscillation in the combustor with backward-facing step is mainly based on experiment and numerical simulation, but less on the theoretical research and mechanism analysis. Because the experimental and numerical studies consume a lot of resources and time, it is necessary to study the mechanism and evolution of thermoacoustic oscillation involving vortex shedding based on the basic model. In this regard, scholars have done a lot of research. Based on the simplified model of a combustor with backward-facing step, Matveev and Culick [23] derived a reduced order model of the interaction between vortex shedding, acoustic field of combustor and combustion process, and used the model to calculate the frequency locking of thermoacoustic oscillation process, which was verified by comparing with the experimental results. At the same time, they pointed out that the simplified model could simulate many nonlinear phenomena in real combustion chamber, such as mode coupling, frequency lock-in, hysteresis, bifurcation and chaos. Based on the model proposed by Matveev, Tulsyan et al. [24] numerically calculated the time series of thermoacoustic oscillation in the system under different parameters, and compared the influences of system parameters such as initial disturbance and damping coefficient on the thermoacoustic oscillation. Based on the simplified model of thermoacoustic oscillation caused by vortex shedding, nonlinear phenomena in the interaction between vortex shedding, acoustic field and combustion process were studied in references [25-27]. Singaravelu and Mariappan [28] nondimensionalized the governing equations of the model and analyzed the linear stability. They derived the formula for calculating the Poincaré section in the process of thermoacoustic oscillation, and concluded that the stability of the system is related to the eigenvalues of the

Poincaré map, thus quantifying the stability of the thermoacoustic interaction. Singaravelu and Mariappan [29] further studied the phenomenon of vortex-acoustic lock-in in combustion instability based on the non-dimensional governing equation. Using the amplitude of velocity fluctuation in the system from zero to peak as the criterion to judge the Helmholtz number's transition from vortex shedding mode to acoustic mode, they proposed a criterion to judge the vortex-acoustic lock-in and compared it with the experimental results. Chakravarthy et al. [30] experimentally studied the phenomenon of vortex-acoustic lock-in in the combustion chamber with a backward-facing step, and the results showed that vortex-acoustic lock-in is an important indicator of combustion instability.

In the past half century, scholars at home and abroad have carried out a lot of research work on thermoacoustic instability, but these work is mainly focused on experimental research, and the theoretical research is still scarce. At present, based on the thermoacoustic model of vortex shedding proposed by Matveev and Culick [23], the influence of some key parameters on the system are analyzed, and some nonlinear phenomena such as vortex-acoustic lock-in are found. However, the influence of the mainstream velocity on the thermoacoustic oscillation of the system has not been studied, and the mechanism of the vortex-acoustic lock-in phenomenon found in the experiment has not been analyzed from the viewpoint of nonlinear dynamics.

1.3 Content of the study

The study mainly focus on the nonlinear analysis of thermoacoustic instability based on the model involving vortex shedding proposed by Matveev and Culick [23]. In the Chapter 2, the basic concepts and analysis methods of nonlinear dynamical system are introduced briefly. In the Chapter 3, the physical model and the establishment process of the governing equations are introduced, including the Rijke tube model and the model of combustor with backward-facing step. Chapters 4 to 6 are the main work of this study. The similarity and the vortex-acoustic lock-in behaviors with the steady state velocity change are firstly studied in Chapter 4. Then in Chapter 5, the frequency-

locked behaviors under the condition of fluctuating mainstream velocity are studied. Furthermore, the influences of external harmonic excitation on the thermoacoustic system is studied in Chapter 6. Finally, the main conclusions of this study are summarized in Chapter 7.

Chapter 2 Fundamental theories

2.1 Differential dynamical system and phase space

This chapter mainly introduces the basic concepts and analysis methods of nonlinear dynamical system, including the description methods and analysis methods of dynamical system, mainly referring to these books [31-35].

The governing equations of continuous dynamical systems are generally expressed in the form of differential equations. According to whether there are time-dependent terms in the equation, it can be classified into autonomous and non-autonomous differential equations. But common nonlinear ordinary differential equations can be transformed into autonomous first order ordinary differential equations. For example, for the following second order ordinary differential equation,

$$\ddot{x} = f\left(x, \dot{x}\right) \tag{2.1}$$

Let $y = \dot{x}$, then the above formula can be reduced to the following system of first order ordinary differential equations,

$$\begin{cases} \dot{x} = y \\ \dot{y} = f\left(x, y\right) \end{cases} \tag{2.2}$$

For the non-autonomous equation, the explicit time variable t can be regarded as a new variable, that is, the non-autonomous system can be transformed into an autonomous system by introducing $z = t$. For example, the equation

$$\dot{x} = f\left(x, t\right) \tag{2.3}$$

can be transformed into

$$\begin{cases} \dot{z} = 1 \\ \dot{x} = f\left(x, z\right) \end{cases} \tag{2.4}$$

Therefore, common differential dynamical systems can be expressed by first order

autonomous differential equations, which is called the standard form of dynamical equations.

For a dynamical system, it is written in standard form as follows,

$$\dot{\boldsymbol{x}} = \boldsymbol{f}\left(\boldsymbol{x}\right) \tag{2.5}$$

where $\boldsymbol{x}$ is a vector in an n-dimensional Euclidean space, and its component in the i-th direction is x_i. The R^n space formed by the state variable x_i is called phase space, or state space. Through the phase space, the dynamical characteristics of complex system can be displayed by intuitive geometric images.

2.2 Poincaré mapping

In order to intuitively analyze the motion process of multivariable dynamical system, Poincaré proposed a method: in the N-dimensional phase space of N-dimensional system, an $N-1$-dimensional hyperplane (called Poincaré section) was selected to study the motion process of points on this section. Because the dimension of the section is less than that of the phase space, the distribution of these intersection points is more simple and intuitive. Let these intersection points be $P_0, P_1, P_2, \ldots, P_n, \ldots$, respectively, then the continuous equations of motion in phase space can be discretized as the mapping between the intersection points, as follows,

$$P_{n+1} = T\left(P_n\right) \tag{2.6}$$

here T is called Poincaré Mapping.

For the periodic motion of a single variable, its trajectory in phase space is a closed curve. For the system with two periodic variables (such as the coupled oscillator system), its trajectory in the 2×2-dimensional phase space is on a two-dimensional torus, as shown in Fig. 2.1. If the periods of two variables x_1 and x_2 are equal, the trajectories in the phase space always pass through Poincaré section at the same point. If the system has two frequencies ω_1 and ω_2, and the ratio of the two frequencies

$\Omega = \omega_1/\omega_2$ is a rational number, the system is still in periodic motion. Here, the ratio of two frequencies Ω is called the rotation number.

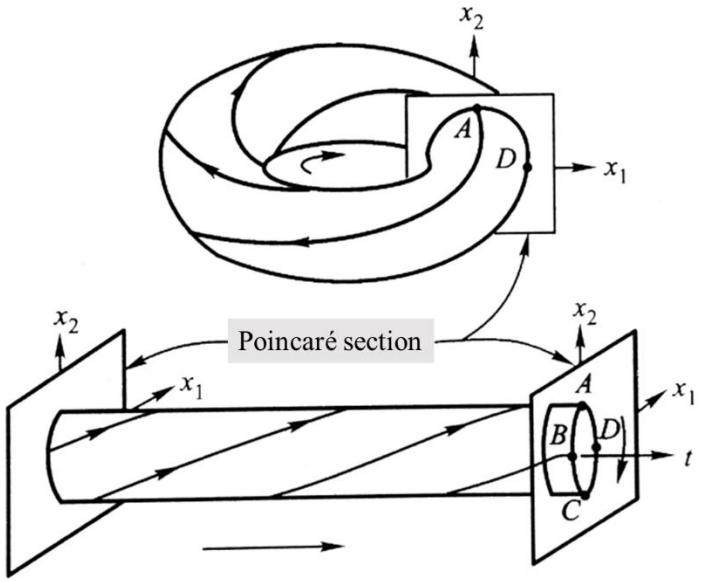

Fig. 2.1 Phase trajectories of periodic motion of two variables.

For quasi periodic motion, the rotation number is an irrational number, and the motion in x_1 and x_2 directions cannot be coordinated. Every time the phase trajectory passes through the intersection point on the Poincaré section, it turns an angular displacement, which is Ω. That is, the intersection of the phase trajectory and the Poincaré section will move on the torus at the angular velocity of Ω. This motion is ergodic to the torus.

Chapter 3 Mathematical and physical model

3.1 Model of Rijke tube

3.1.1 Physical model

Thermoacoustic instability is a complex phenomenon, and to understand its nature some simplified models must be used. In this study, the nonlinear analysis of a thermoacoustic system is performed, by using a simple model for thermoacoustic oscillations in a Rijke tube.

The Rijke tube model used in the study follows Balasubramanian and Sujith [9], and is for the geometry shown in Fig. 3.1. In the horizontal Rijke tube, the influence of natural convention on the mean flow rate can be excluded. It is convenient for studying the fundamental principles of thermoacoustic instabilities to set up a horizontal Rijke tube with an electric heat source. In such a setup, the mean flow is provided by a blower, which sucks air in the tube.

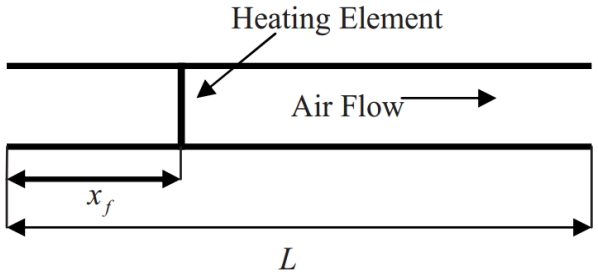

Fig. 3.1 Schematic of a horizontal Rijke tube with an electric heater as source.

3.1.2 Governing equations

Neglecting the effect of mean flow and mean temperature gradient in the duct, the model is governed by the non-dimensional linearized momentum and energy equations for the acoustic field as given below in Eqns. (3.1) and (3.2). The scales for non-dimensionalization are as given in Eqn. (3.3).

$$\gamma M \frac{\partial u'}{\partial t} + \frac{\partial p'}{\partial x} = 0 \tag{3.1}$$

$$\frac{\partial p'}{\partial t} + \gamma M \frac{\partial u'}{\partial x} + \zeta p' = (\gamma - 1)\dot{Q}'(t)\delta\left(x - x_f\right) \tag{3.2}$$

$$x = \frac{\tilde{x}}{L}; t = \frac{c_0}{L}\tilde{t}; u' = \frac{\tilde{u}'}{u_0}; p' = \frac{\tilde{p}'}{\bar{p}}; M = \frac{u_0}{c_0} \tag{3.3}$$

In this model, x is the distance along the axial direction, L is the length of the duct and t is time. The flow has a steady state velocity u_0, pressure $\bar{p}$ and temperature $\bar{T}$. u' is acoustic velocity and p' is acoustic pressure. γ is the ratio of specific heats of the medium, c_0 is the speed of sound and M is the Mach number of the mean flow. ζ is the damping coefficient, x_f is the location of the heat source and $\dot{Q}'$ is the heat release rate fluctuations per unit area due to the electrical heater. Quantities with tilde are dimensional and those without tilde are non-dimensional.

The response of the heat transfer from the wire filament to acoustic velocity fluctuations is quantified using the correlation given by Heckl [36]. The heat release rate fluctuations is given in Eqn. (3.4).

$$\dot{Q}'(t) = \frac{2L_w\left(T_w - \bar{T}\right)}{S\sqrt{3}c_0\bar{p}}\sqrt{\pi\lambda C_V u_0 \bar{\rho}\frac{d_w}{2}}\left[\sqrt{\left|\frac{1}{3} + u_f'\left(t-\tau\right)\right|} - \sqrt{\frac{1}{3}}\right] \tag{3.4}$$

here d_w, L_w and T_w are the diameter, length and temperature of the wire respectively, S is the cross sectional area, $\bar{\rho}$ is the mean density, λ is the thermal conductivity and C_V is the specific heat at constant volume of the medium within the duct. τ is the time lag representing the thermal inertia of the heat transfer.

The non-dimensional partial differential equations Eqn. (3.1) and Eqn. (3.2) can be reduced to a set of ordinary differential equations by expanding the acoustic variables in terms of basis functions using the Galerkin technique. The velocity and pressure field can be written in terms of the duct's natural modes as follows,

$$u'(x,t)=\sum_{j=1}^{N}\eta_j(t)\cos(j\pi x) \tag{3.5}$$

$$p'(x,t)=-\sum_{j=1}^{N}\frac{\gamma M}{j\pi}\dot{\eta}_j(t)\sin(j\pi x) \tag{3.6}$$

Substituting the above expansions into Eqn. (3.1) and Eqn. (3.2), the following evolution equations are obtained,

$$\frac{d\eta_j}{dt}=\dot{\eta}_j \tag{3.7}$$

$$\frac{d\dot{\eta}_j}{dt}+{k_j}^2\eta_j+\zeta_j\dot{\eta}_j=-\frac{2k}{\gamma M}\,j\pi\left[\sqrt{\left|\frac{1}{3}+u'_f\left(t-\tau\right)\right|}-\sqrt{\frac{1}{3}}\right]\sin\left(j\pi x_f\right) \tag{3.8}$$

where

$$k=(\gamma-1)\frac{2L_w\left(T_w-\bar{T}\right)}{S\sqrt{3}c_0\bar{p}}\sqrt{\pi\lambda C_V u_0\bar{\rho}\frac{d_w}{2}} \tag{3.9}$$

here, $k_j=j\pi$ refers to the non-dimensional wave number. The governing equations (3.1) and (3.2) reduce to two ordinary differential equations (ODEs) for each mode j. Then the fourth-order Runge-Kutta algorithm is used to solve the above equations (3.7) and (3.8).

3.2 Model of combustor with backward-facing step

3.2.1 Physical model

Combustion chamber with backward step is a very common type of combustion chamber. Figure 3.2 shows a simplified model of a combustion chamber with a backward-facing step, which is a tube with openings at both ends and a small step inside the tube. In order to study this thermoacoustic system, the coordinate system shown in Fig. 3.2 was established according to the paper of Matveev and Culick [23], and the complex problem was simplified into one-dimensional problem. The total length of the

tube is L, the position of the backward-facing step is X_s, and the position of the downstream wall of the step is X_c. The reactants enter the combustion chamber at a certain mainstream velocity u_0. Because of the instability of the shear layer at the step, vortexes will be generated when the fluid flows through the step. When certain conditions are met, the vortex carried reactants will fall off from the step, move downstream in the concave cavity, and finally hit the downstream wall, resulting in centralized combustion and instantaneous heat release. The unstable heat release caused by vortex shedding will interact with the pressure and velocity fluctuations of acoustic field in the combustion chamber. Under certain conditions, when the unstable heat release forms a positive feedback loop with the periodic oscillation of the pressure and velocity of acoustic field, the oscillation will continue. This process is the thermoacoustic oscillation induced by vortex shedding, which leads to combustion instability.

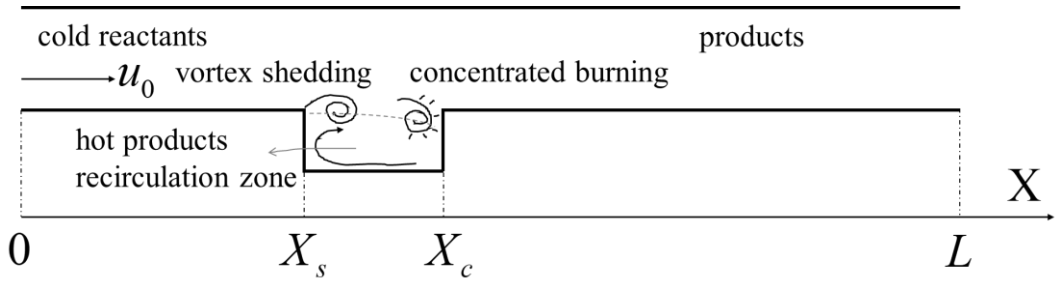

Fig. 3.2 The simplified model of combustor with backward-facing step.

3.2.2 Vortex shedding model

In fact, the governing equations of vortex generation, convection and breakdown in unsteady flow are all nonlinear. In order to facilitate the study, the vortex shedding model developed by Matveev and Culick [23] is introduced. In steady flow, there will be regular vortex shedding behind the bluff body, and the frequency of vortex shedding is expressed as follows,

$$f_{s0} = St\frac{u_0}{d} \tag{3.10}$$

where St is Strouhal number and d is characteristic dimension. In this study, the height of backward-facing step is taken as characteristic dimension. In the thermoacoustic system, the process of vortex shedding is affected not only by the mainstream velocity, but also by the pressure and velocity fluctuations of the acoustic field. Therefore, Matveev and Culick [23] proposed a simplified vortex shedding model in unsteady flow, in which Strouhal number is taken as the value of steady flow. The instantaneous resultant velocity $u(t) = u_0 + u'(t)$, and the growth rate of circulation of the vortex shedding from the step is expressed as follows,

$$\frac{d\Gamma_j}{dt} = \frac{1}{2}u(t)^2 \tag{3.11}$$

where Γ_j is the circulation of the j-th vortex. When the accumulation of the circulation reaches the critical circulation Γ_{sep}, the j-th vortex will fall off from the step. Γ_{sep} can be represented by the instantaneous velocity $u(t)$ as follows,

$$\Gamma_{sep} = \frac{u(t)d}{2St} \tag{3.12}$$

After the j-th vortex shedding, it will move downstream from X_s to X_c along the boundary of the mainstream and the recirculation zone in the cavity at the resultant velocity at the instantaneous position of the vortex. The velocity of the shedding vortex moving downstream can be expressed as follows,

$$\frac{dx_j}{dt} = \alpha u_0 + u'(x_j, t) \tag{3.13}$$

where, x_j is the instantaneous position of the j-th vortex, and $u'(x_j, t)$ is the instantaneous pulsating velocity at x_j. α is a coefficient less than 1, usually 0.4-0.6 [28]. In the cavity of segmented solid rocket motor, α is usually 0.5-0.6 [37].

3.2.3 Thermoacoustic model

According to the paper of Tulsyan et al. [24], Neglecting all direct influences of

temperature gradient, viscous effect and steady flow on the acoustic field, the momentum and energy governing equations of the acoustic field in this system can be expressed as follows,

$$\frac{1}{\rho_0}\frac{\partial p'}{\partial x}+\frac{\partial u'}{\partial t}=0 \tag{3.14}$$

$$\frac{\partial p'}{\partial t}+\gamma p_0\frac{\partial u'}{\partial x}=(\gamma-1)\dot{Q} \tag{3.15}$$

where p' and u' are the pressure fluctuation and velocity fluctuation in the acoustic field respectively, ρ_0 is the average density at steady state, γ is the specific heat capacity ratio, p_0 is the average pressure at the undisturbed state and $\dot{Q}$ is the heat release rate. The $\dot{Q}$ term is the source term in the thermoacoustic system and is the unstable heat release rate induced by vortex shedding. The shedding vortex with the reactants impinges on the downstream wall X_c and burns, accompanied by heat release. Therefore, the heat release rate can be expressed by the delta function in space and time [23], as follows,

$$\dot{Q}=\beta\sum_j \Gamma_j\delta(t-t_j)\delta(x-X_c) \tag{3.16}$$

The sum in the equation is determined by the number of shedding vortices. β is an appropriate heat release coefficient, which relates impingement of vortex to heat release rate. t_j is the time when the j-th vortex with the circulation Γ_j impinges and burns. X_c is the position of vortex impact, that is, the spatial position of instantaneous heat release. It can be seen from the above equation that the heat release rate is approximately proportional to the circulation, and the critical circulation of shedding vortex represents the intensity of heat release in combustion.

The Galerkin method is used to reduce the order of partial differential equations (3.14) and (3.15) to a series of ordinary differential equations. In order to satisfy the acoustic boundary conditions of open tube at both ends, the basis functions of pressure fluctuation and velocity fluctuation are respectively selected as follows,

$$p' = -p_0 \sum_{n=1}^{\infty} \frac{\dot{\eta}_n(t)}{\omega_n} \sin\left(k_n x\right) \tag{3.17}$$

$$u' = \frac{p_0}{\rho_0 c_0} \sum_{n=1}^{\infty} \eta_n(t) \cos\left(k_n x\right) = \frac{c_0}{\gamma} \sum_{n=1}^{\infty} \eta_n(t) \cos\left(k_n x\right) \tag{3.18}$$

where $p_0 = \rho_0 c_0^2/\gamma$, and c_0 is the speed of sound. $k_n = n\pi$ is the wave number of the n-th mode, where $n = \{1,2,\cdots\}$. $\omega_n = c_0 k_n$ refers the angular frequency of the n-th duct mode, and $\eta_n(t)$ is the amplitude of the n-th mode.

Substituting the equations (3.17) and (3.18) into equations (3.14) and (3.15), as follows,

$$-\frac{p_0}{\rho_0} \sum_{n=1}^{\infty} \frac{\dot{\eta}_n(t) k_n}{\omega_n} \cos\left(k_n x\right) + \frac{p_0}{\rho_0 c_0} \sum_{n=1}^{\infty} \frac{d\eta_n(t)}{dt} \cos\left(k_n x\right) = 0 \tag{3.19}$$

$$-p_0 \sum_{n=1}^{\infty} \frac{d\dot{\eta}_n(t)}{dt} \frac{1}{\omega_n} \sin\left(k_n x\right) - p_0 c_0 \sum_{n=1}^{\infty} \eta_n(t) k_n \sin\left(k_n x\right) = \left(\gamma - 1\right)\dot{Q} \tag{3.20}$$

Multiplying each term by $\sin(k_n x)$, as follows,

$$\int \sin\left(k_i x\right)\sin\left(k_n x\right) dx = \begin{cases} \int \sin^2\left(k_n x\right) dx = \int \left[\frac{1}{2} - \frac{1}{2}\cos\left(2k_n x\right)\right] dx \\ \qquad\qquad = \frac{1}{2}x - \frac{1}{4n\pi}\sin\left(2n\pi x\right) = \frac{1}{2}x, \ i = n \\ 0, i \neq n \end{cases}$$

$$-p_0 \frac{d\dot{\eta}_n(t)}{dt} \frac{1}{\omega_n} \int_0^L \sin^2\left(k_n x\right) dx - p_0 c_0 \eta_n(t) k_n \int_0^L \sin^2\left(k_n x\right) dx = \left(\gamma - 1\right) \int \sin\left(k_n x\right) \dot{Q} dx$$

$$-p_0 \frac{d\dot{\eta}_n(t)}{dt} \frac{1}{\omega_n} \frac{L}{2} - p_0 c_0 \eta_n(t) k_n \frac{L}{2} = \left(\gamma - 1\right) \int \sin\left(k_n x\right) \dot{Q} dx$$

A family of ordinary differential equations which are projected onto the basis functions can be obtained, as follows,

$$\ddot{\eta}_n(t) + \omega_n^2 \eta_n(t) = -\frac{2\left(\gamma - 1\right)\omega_n}{L p_0} \int \sin\left(k_n x\right) \dot{Q} dx \tag{3.21}$$

According to the paper of Matveev and Culick [23], the damping coefficient is,

$$\xi_n = \frac{1}{2\pi}\left[c_1 \frac{\omega_n}{\omega_1} + c_2 \sqrt{\frac{\omega_1}{\omega_n}} \right] \tag{3.22}$$

where, c_1 is the damping coefficient of end loss, and c_2 is the damping coefficient of boundary layer loss. By artificially introducing the damping term and substituting the heat source term (3.16) into equation (3.21), the following equations can be obtained,

$$\frac{d\eta_n(t)}{dt} = \dot{\eta}_n(t) \tag{3.23}$$

$$\ddot{\eta}_n(t) + \left(2\xi_n \omega_n \dot{\eta}_n(t)\right) + \omega_n^2 \eta_n(t) = -\frac{2(\gamma-1)\beta}{Lp_0} \omega_n \sin\left(k_n X_c\right) \sum_j \Gamma_j \delta\left(t - t_j\right) \tag{3.24}$$

Equations (3.23) and (3.24) written together represent a kicked oscillator, equation (3.25), which will behave like a damped oscillator at all times, with the jump conditions, equation (3.26), at the time of kicking. Equation (3.25) is as follows,

$$\ddot{\eta}_n(t) + \left(2\xi_n \omega_n \dot{\eta}_n(t)\right) + \omega_n^2 \eta_n(t) = c\omega_n \sin\left(k_n X_c\right) \sum_j \Gamma_j \delta\left(t - t_j\right) \tag{3.25}$$

where $c = -2(\gamma-1)\beta/(Lp_0)$ is called the kicking coefficient. There is no heat release during the time interval between the two vortex impacts and combustion. Therefore, the right end of equation (3.25) equals zero, and the system will behave like a damped oscillator. It is assumed that the instantaneous moments before and after the impact of the j-th vortex are t_j^- and t_j^+, respectively. Neglecting the effect of damping, the following jump conditions can be obtained by integrating equation (3.25) within the time interval $\left[t_j^-, t_j^+\right]$,

$$\begin{aligned} \eta_n^+ &= \eta_n^- \\ \dot{\eta}_n^+ - \dot{\eta}_n^- &= c\Gamma_j \omega_n \sin\left(k_n X_c\right) \end{aligned} \tag{3.26}$$

At the moment of vortex impact, the amplitude of velocity mode $\eta_n(t)$ remains unchanged, while the amplitude of pressure mode $\dot{\eta}_n(t)$ jumps abruptly.

Chapter 4 Similarity and vortex-acoustic lock-in behaviors

4.1 Numerical simulation and verification of numerical results

The calculation of the study is completed by MATLAB program. According to the results of existing studies and the preliminary calculation, the following parameters can be selected to more clearly present the nonlinear characteristics of the model, $L = 1\text{m}, X_s = 0.3\text{m}, X_c = 0.45\text{m}, \alpha = 0.5, \gamma = 1.4, c_0 = 750\text{m/s}, c = -0.0015, St/d = 10\text{m}^{-1}$ [24]. The results of calculation with different numbers of Galerkin modes are compared. When the number of modes is less than 10, the error of numerical simulation is larger. Theoretically, the more the number of modes is, the closer the calculation results are to the real results, and the influence of higher-order modes can be taken into account. However, the more the number of modes is, the greater the amount of calculation is. Matveev and Culick [23] focused on the influence of the number of modes on the calculation results. The results showed that the selection of the first 10 modes could meet the accuracy and convergence of the calculation. Therefore, the first 10 modes is taken in all the calculations in this study.

In the process of calculation, the time step is 10^{-6}s, which can meet the accuracy of calculation. When there is no shedding vortex impinging on X_c (i.e. $t \neq t_j$), the right end of equation (3.25) equals zero. The fourth-order Runge-Kutta integral is used to calculate $\eta_n(t)$ and $\dot{\eta}_n(t)$, and the time step is $dt = 10^{-6}$s. Then, the instantaneous pressure and velocity are calculated according to equations (3.17) and (3.18), and the circulation and critical circulation at X_s are calculated by equations (3.11) and (3.12). If $\Gamma_j \geq \Gamma_{sep}$, the j-th vortex falls off and moves downstream, following the velocity in equation (3.13). At the same time, the circulation at X_s is reset to 0, and the calculation of circulation of the $(j+1)$-th vortex in the next time step is started. When the j-th shedding vortex hits X_c (i.e. $t = t_j$), $\dot{\eta}_n(t)$ jumps abruptly with equation (3.26),

while $\eta_n(t)$ is invariant. By repeating this process in the whole calculation, the pressure and velocity of acoustic field at any time and at any position can be obtained from equations (3.17) and (3.18). The calculation results in the study are all based on the time series of pressure and velocity at the backward-facing step X_c.

In order to verify the accuracy of the calculation, the parameter is first set as $\alpha = 0.4, c_1 = 0.0225, c_2 = 0.0025, u_0 = 50\mathrm{m/s}$, and other parameters are the same as above. Calculations were carried out under initial perturbations $\eta_1(0) = 0.05$ and $\eta_1(0) = 0.07$ (other initial perturbations were all zero, $\eta_{n\neq1}(0) = 0, \dot{\eta}_n(0) = 0$) respectively, and the results were compared with those in the paper of Tulsyan et al. [24]. Figure 4.1 shows the comparison between our results (the upper portion) and those in the existing study, and the numerical results are in good agreement with those of others. The figure on the left shows the result when $\eta_1(0) = 0.05$, and the oscillation decays with time. The figure on the right shows the result when $\eta_1(0) = 0.07$, and the oscillation diverges with time. It can be seen that the difference of initial perturbation is very small, but the oscillation of the system shows very different results.

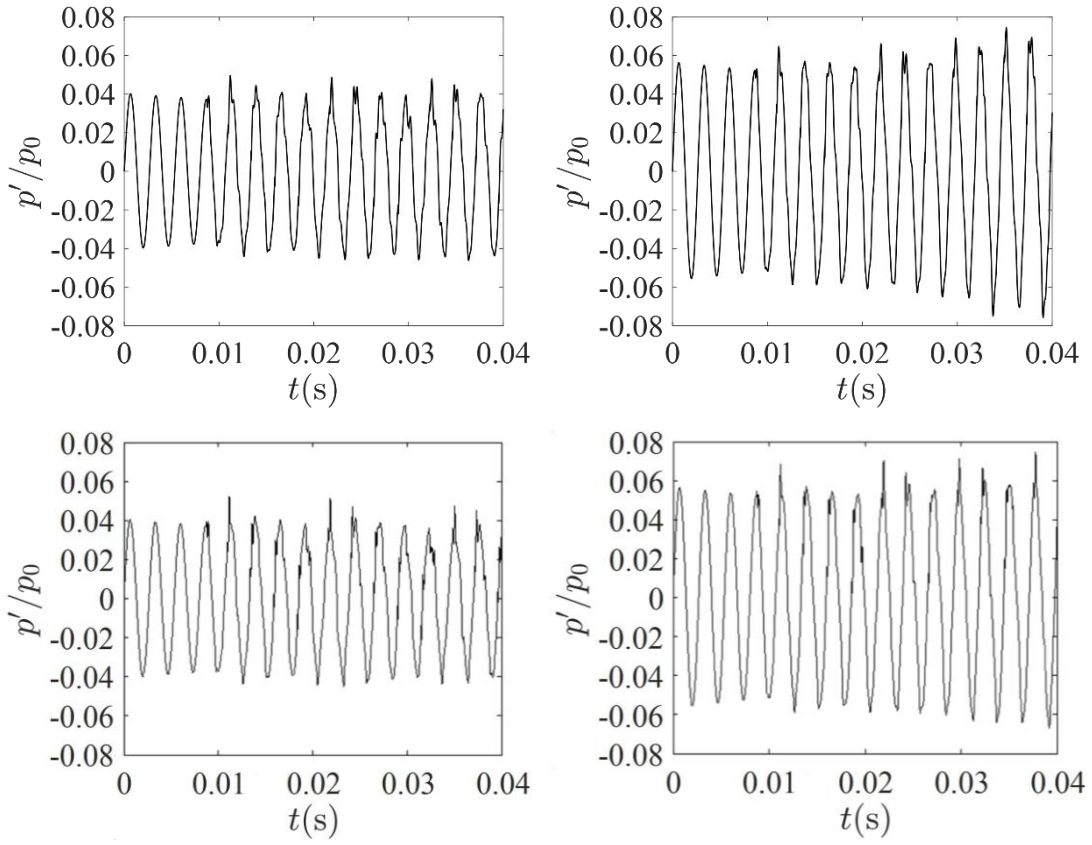

Fig. 4.1 Verification of computation model [24].

4.2 Initial conditions sensitivity of the system

In order to further analyze the multiple solutions of the system, the parameters of the system are set as $\alpha = 0.4, c_1 = 0.03375, c_2 = 0.00375, u_0 = 50\mathrm{m/s}$ [24]. The pressure and velocity fluctuations of the system are calculated under two very close initial perturbations $\eta_1(0) = 0.01240087$ and $\eta_1(0) = 0.01240088$ (other initial perturbations were all zero, $\eta_{n\neq1}(0) = 0, \dot{\eta}_n(0) = 0$) respectively.

Figure 4.2 shows the phase diagram after phase space reconstruction and Poincaré section. The three-dimensional phase diagram of pressure ratio shown in Fig. 4.2 (a) and (c) is obtained by phase space reconstruction of the time series of p'/p_0 after the oscillation is stable. The delay time τ in the phase space reconstruction is taken as 100. The Poincaré section shown in Fig. 4.2 (b) and (d) is the section at $p'/p_0(t) = 0$ in Fig. 4.2 (a) and (c), respectively. Among them, Fig. 4.2 (a) and (b) correspond to the result under $\eta_1(0) = 0.01240087$, and Fig. 4.2 (c) and (d) correspond to the result under $\eta_1(0) = 0.01240088$. From the three-dimensional phase diagram and Poincaré section, it can be seen that when $\eta_1(0) = 0.01240087$, there are a few finite points on the Poincaré section, which indicates that the system eventually tends to periodic oscillation with small amplitude. However, when the initial perturbation is $\eta_1(0) = 0.01240088$, there is no closed curve on the Poincaré section for a long enough time series, and there are a large number of finite points on the Poincaré section, indicating that the system finally tends to the complex periodic oscillation with a slightly larger amplitude.

Figure 4.3 (a) and (b) show the time series of the first 0.2 seconds of the pressure ratio under $\eta_1(0) = 0.01240088$ and $\eta_1(0) = 0.01240088$, respectively. The dotted vertical line in the figure shows the moment of pressure jump caused by the impact and combustion of the shedding vortex. It can be seen that the time series before 0.1 seconds are almost the same under two very close initial perturbations. However,

for the time series after 0.1 seconds, the amplitude in Fig. 4.3(a) decreases while the amplitude in Fig. 4.3(b) increases. This is because the small difference in the initial perturbation leads to the small difference in the frequency of vortex shedding and circulation, and the accumulation of the difference results in nonlinear effect. Since the two initial perturbations are in different regions of attraction, the system eventually tends to two different solution branches, so the system has typical nonlinear characteristics.

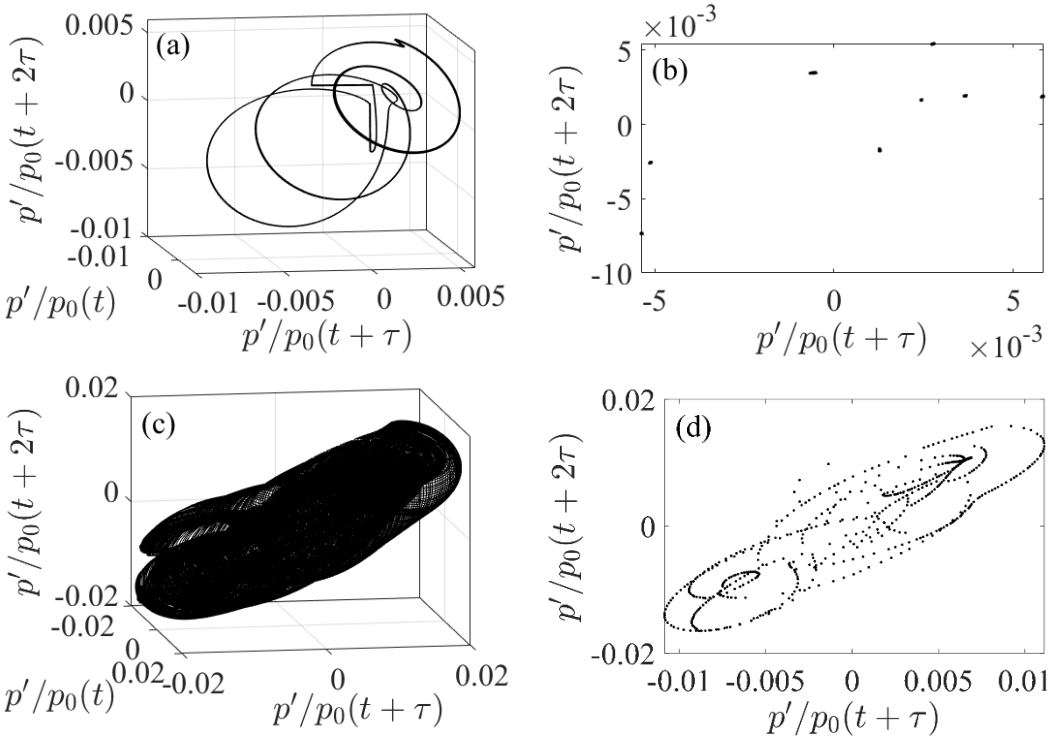

Fig. 4.2 Phase diagram after phase space reconstruction and Poincaré section.

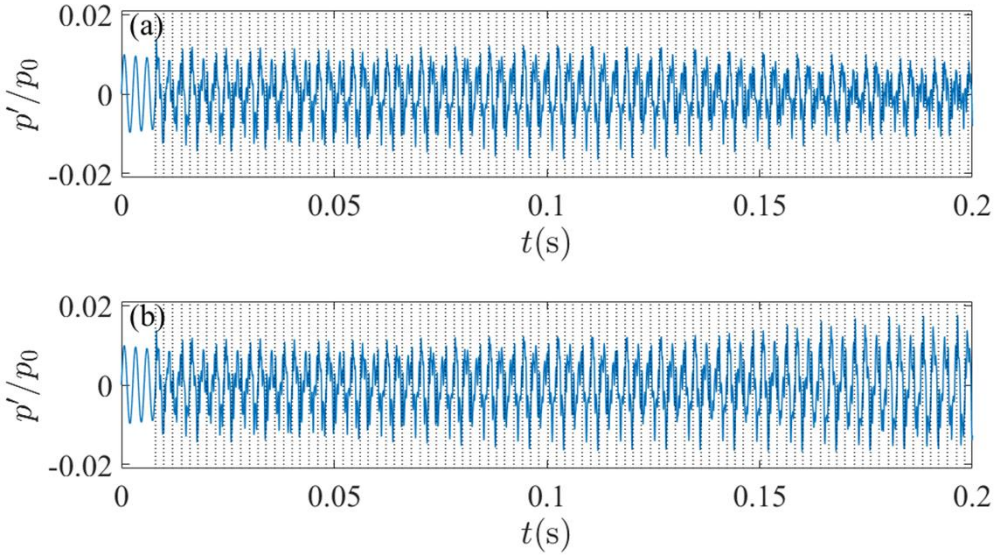

Fig. 4.3 Initial time series of pressure ratios under different initial perturbations.

4.3 Similar structure in the changing process of the amplitude of pressure fluctuation

In order to study the influence of u_0 on the thermoacoustic oscillation of the system, u_0 is uniformly changed within the interval [5,100], and the u' and p' of 381 cases are calculated respectively. In the calculation, the damping coefficients are $c_1 = 0.135, c_2 = 0.015$ [15, 23], other parameters are fixed. The initial perturbation is zero ($\eta_n(0) = \dot{\eta}_n(0) = 0$). After the time series of p' is stable in each case, the maximum and minimum points of the time series of p'/p_0 after 1.4 seconds in each time interval of vortex shedding are obtained, as shown in Fig. 4.4.

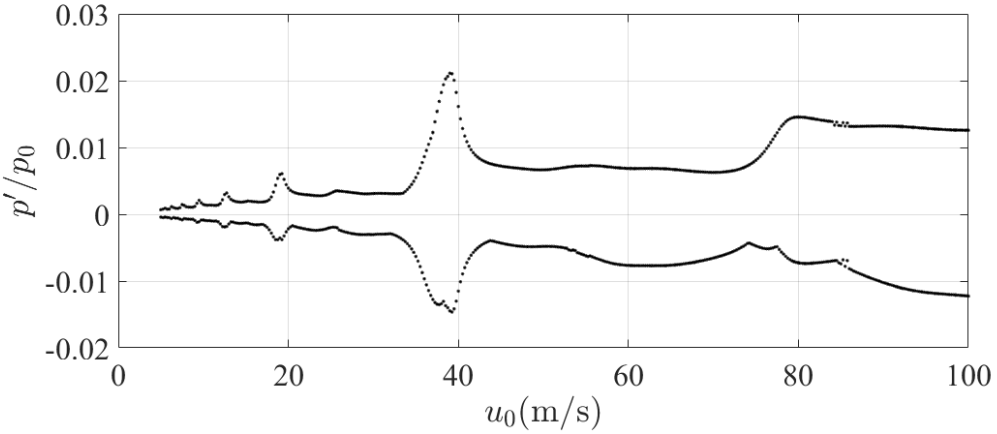

Fig. 4.4 Maximum and minimum pressure ratios at different u_0.

With the increase of u_0, the frequency of vortex shedding in steady state (f_{s0}) increases, but the amplitude of pressure fluctuation does not necessarily increase. Figure 4.4 shows that the amplitude variation of pressure fluctuation has a similar structure under different u_0. Figure 4.5 is a partial enlarged diagram of Fig. 4.4. The curves O1-O2, O2-O3, O3-O4, O4-O5, O5-O6 and O6-O7 are similar. O1, O2, O3, O4, O5, O6 and O7 are the peak points of each curve.

The time series of p'/p_0 from O1 to O6 are shown in Fig. 4.6 (a) to (f), respectively. The dotted vertical line in the figure is the moment of pressure jump caused by the

impact and combustion of the shedding vortex. It can be seen from Fig. 4.6(a) that there are seven decaying periodic oscillations of pressure within the time interval between two vortex impacts in O1 case. From O1 case to O6 case, the number of periodic oscillation of pressure in the time interval between two vortex impacts decreases from 7 times to 2 times. With the increase of u_0, the time of the first impact of vortex keeps moving forward. Meanwhile, the frequency of vortex impact increases, so the frequency of heat release increases. Therefore, the number of periods in the interval between two vortex impacts decreases. Since the velocity fluctuation u' is much less than u_0, Γ_j is mainly dominated by u_0. As u_0 increases, the critical circulation Γ_{sep} increases and the circulation of shedding vortex increases. Further, the pressure jump shown by equation (3.26) increases. In other words, the intensity of heat release increases, and more energy is added to the acoustic field by the combustion process. Therefore, the amplitude of pressure oscillation increases from O1 case to O6 case. Meanwhile, by observing the six peak points in Fig. 4.6 (a) to (f), it can be found that each pressure jump (heat release) occurs at the peak of the pressure oscillation, which will make the oscillation strengthen continuously. From the previous vortex impacts in Fig. 4.6(f), it is obvious that the oscillation is strengthened and the amplitude increases until it becomes stable.

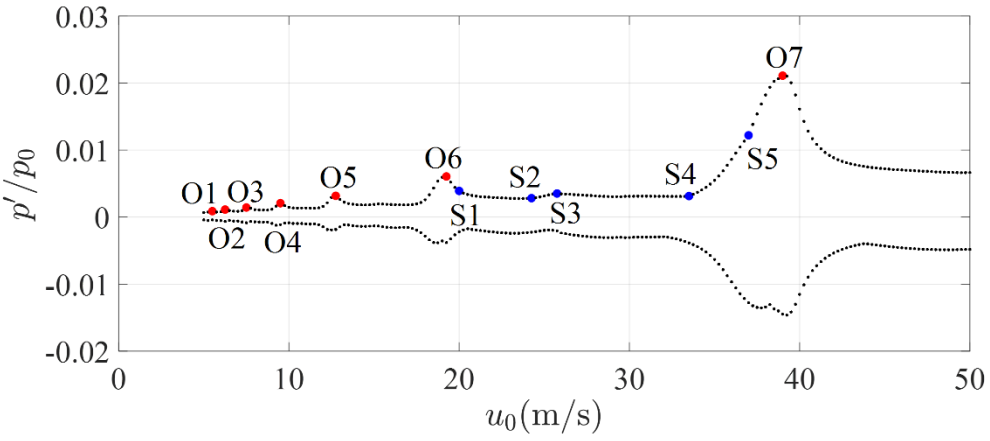

Fig. 4.5 Partial enlarged diagram of Figure 4.4.

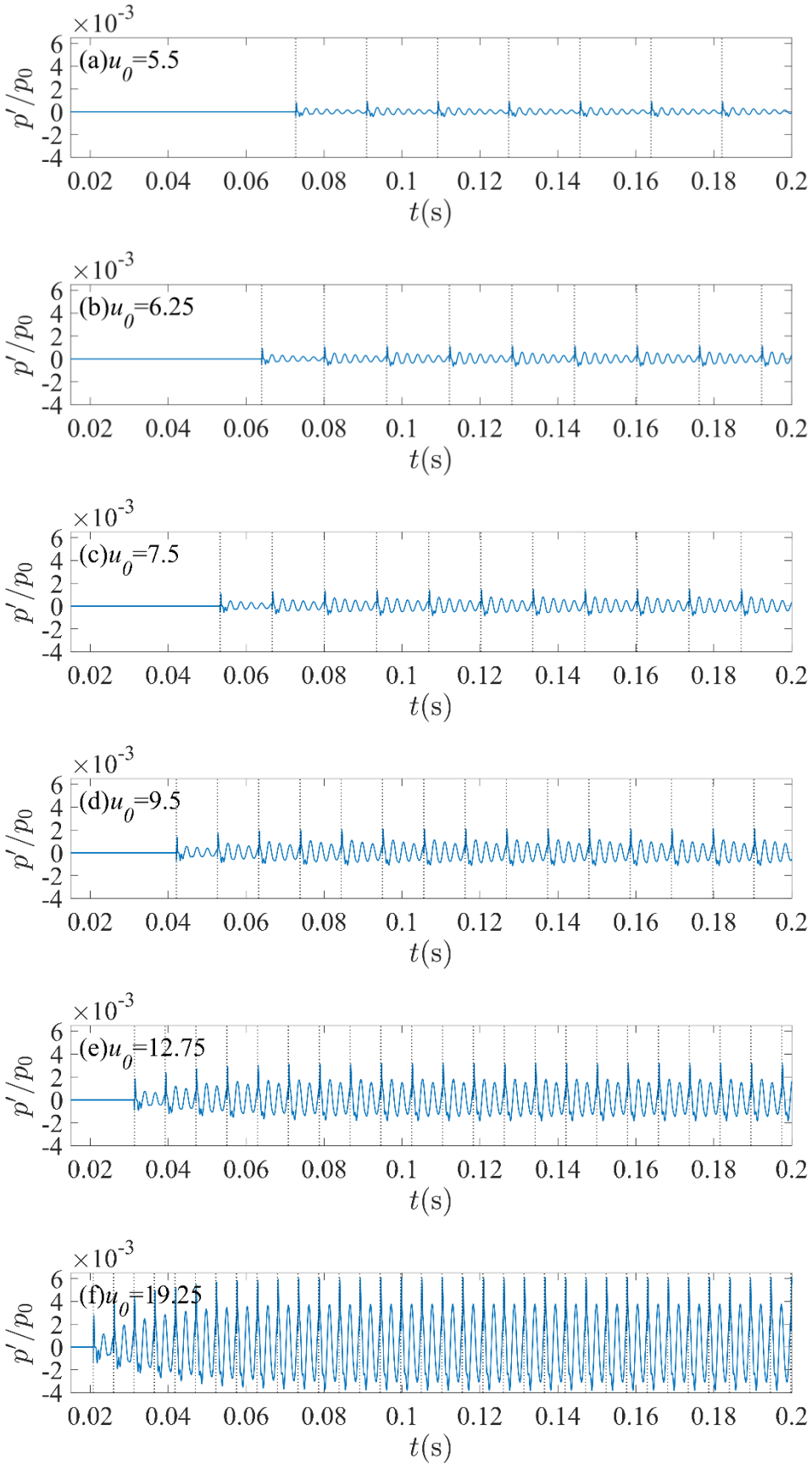

Fig. 4.6 p'/p_0 time series of O1, O2, O3, O4, O5, O6 cases.

In order to study the process in which the amplitudes of different cases on each similar curve first decreased and then increased, the time series of p'/p_0 of S1, S2, S3, S4, S5 and O7 cases on O6-O7 curve are obtained in Fig. 4.7 (a) to (f), respectively. The dotted vertical line in Fig. 4.7 is the moment of pressure jump caused by the impact and combustion of the shedding vortex. The u_0 in the six cases are 20 m/s, 24.25 m/s, 25.75 m/s, 33.5m /s, 37 m/s and 39 m/s, respectively. With the increase of u_0, the circulation of shedding vortex and the intensity of heat release increase. However, the amplitude of pressure fluctuation presents a process from decreasing to increasing.

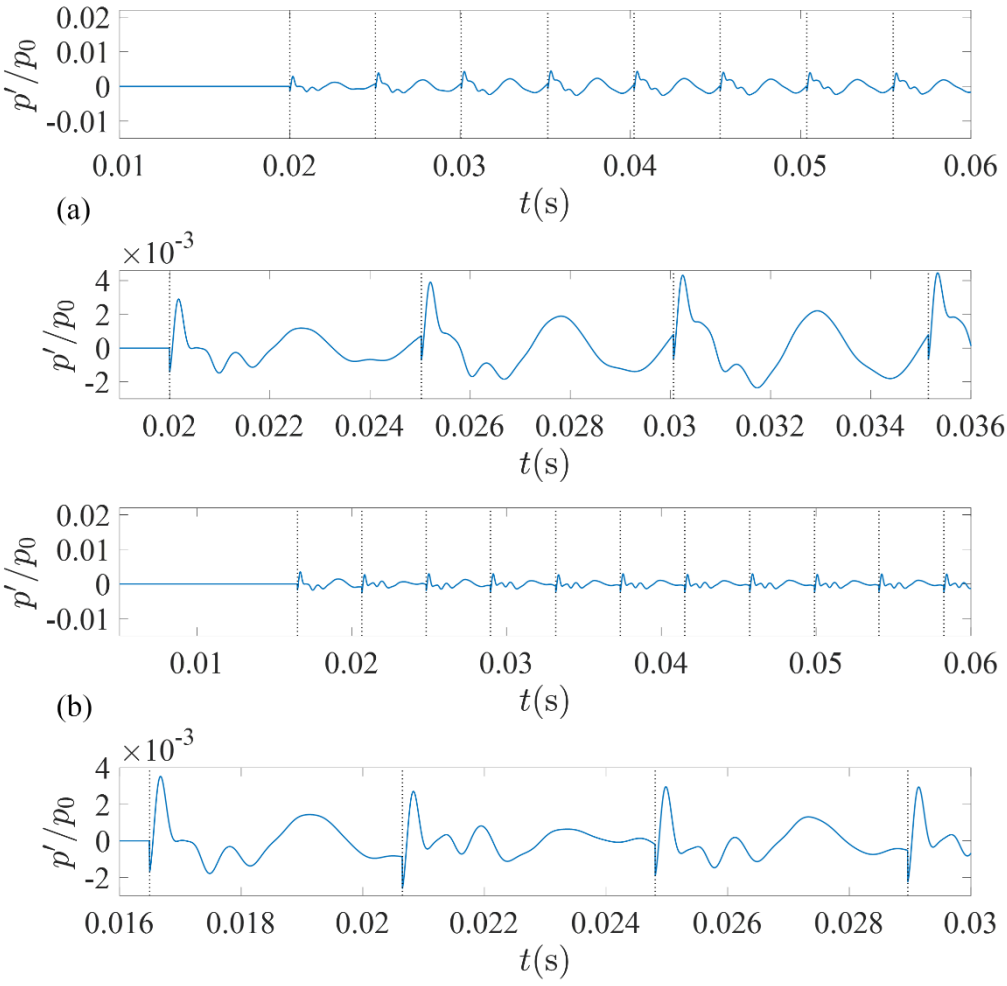

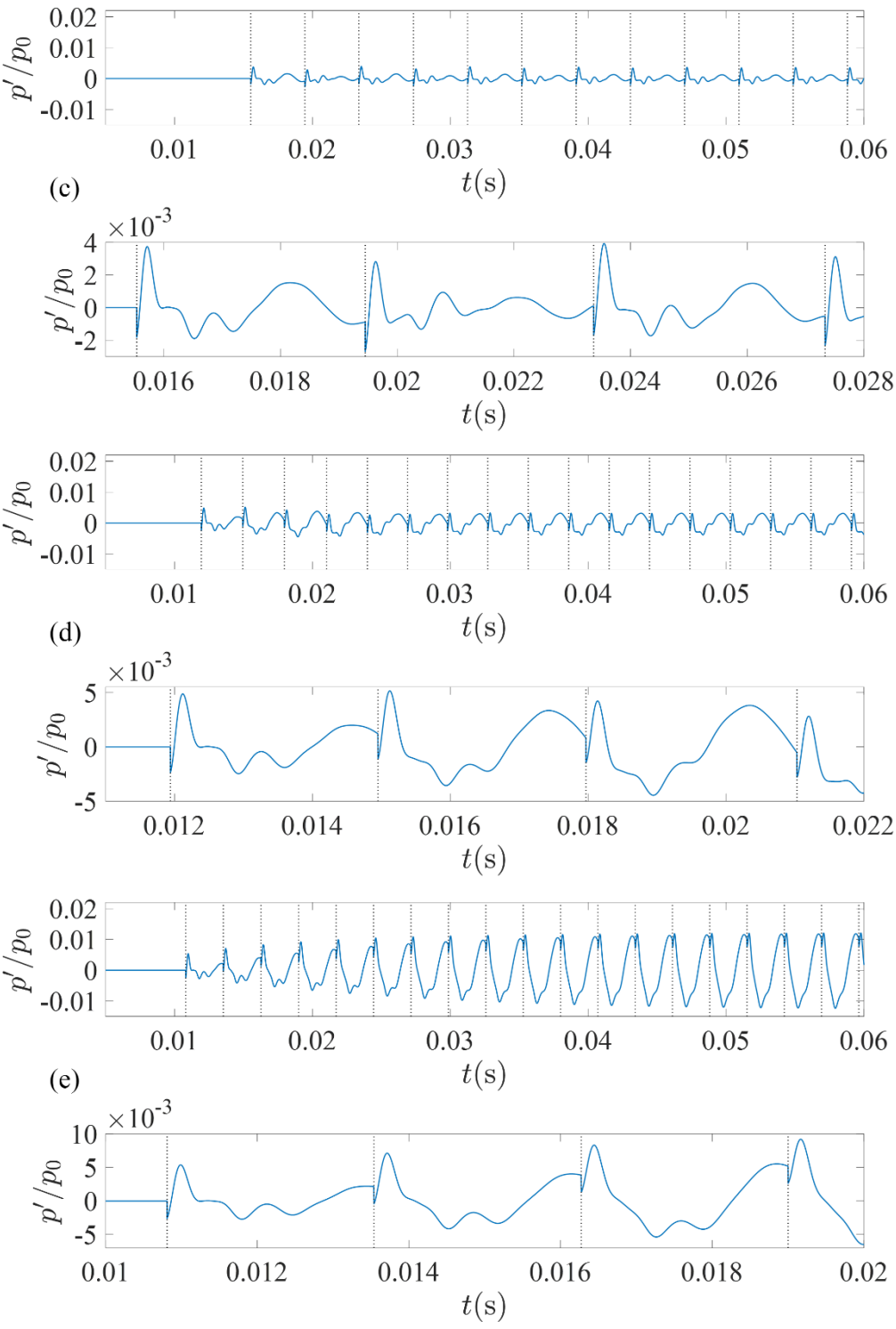
0.02
0.01
0
-0.01
p'/p_0
0.01
0.02
0.03
0.04
0.05
0.06
t(s)
(c)
$\times 10^{-3}$
4
2
0
-2
p'/p_0
0.016
0.018
0.02
0.022
0.024
0.026
0.028
t(s)
0.02
0.01
0
-0.01
p'/p_0
0.01
0.02
0.03
0.04
0.05
0.06
t(s)
(d)
$\times 10^{-3}$
5
0
-5
p'/p_0
0.012
0.014
0.016
0.018
0.02
0.022
t(s)
0.02
0.01
0
-0.01
p'/p_0
0.01
0.02
0.03
0.04
0.05
0.06
t(s)
(e)
$\times 10^{-3}$
10
5
0
-5
p'/p_0
0.01
0.012
0.014
0.016
0.018
0.02
t(s)

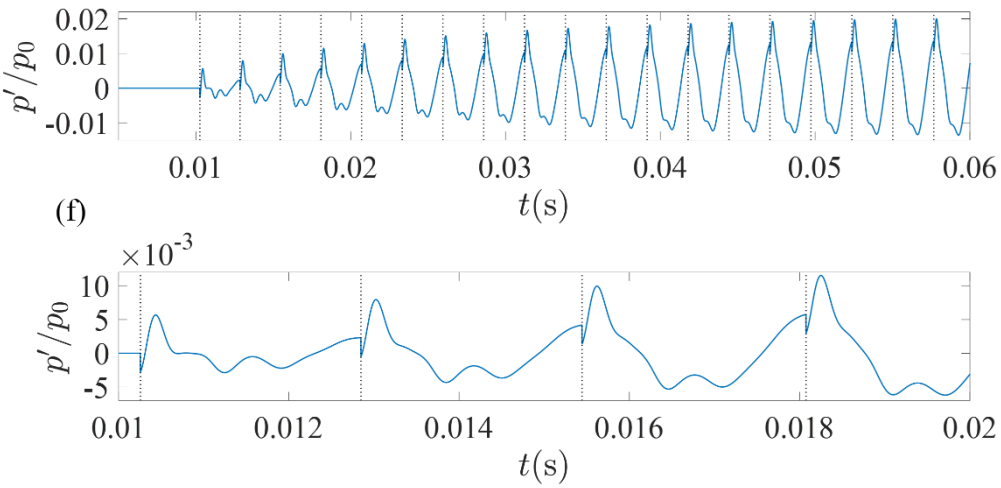

Fig. 4.7 p'/p_0 time series of S1, S2, S3, S4, S5, O7 cases.

By observing the enlarged view of the time series of the first four vortex impacts in Fig. 4.7 (a) to (f), it can be seen that there is a phase difference between the moment of vortex impact and the pressure fluctuation. In S1 case in Fig. 4.7(a), the heat release (pressure jump) occurs before the peak of pressure oscillation, so the amplitude is smaller than that of O6 case. As u_0 increases, the frequency of vortex impact increases, and the time of heat release moves forward. In Fig. 4.7 (b) and (c), the time of heat release in S2 and S3 cases is close to the trough of pressure oscillation, and the oscillation is weakened, so the amplitude is small. In S4 case in Fig. 4.7(d), the heat release occurs at the antinode of the pressure oscillation, and the amplitude is still small. In the S5 case in Fig. 4.7(e), since the time of heat release is close to the previous peak of pressure oscillation, the oscillation begins to strengthen and the amplitude gradually increases. Similarly, in the O7 case in Fig. 4.7(f), since the heat release occurs at the previous peak of pressure oscillation, the oscillation is strengthened and the amplitude increases. The change process conforms to Rayleigh's criterion, that is, when the heat is added at the highest point or removed at the lowest point of the pressure fluctuation, the oscillation is strengthened; on the contrary, the oscillation is weakened.

As u_0 increases, the similar structure presented by the amplitude change of pressure fluctuation will continue. The increase of u_0 leads to the increase of the frequency of vortex impact, and then the increase of the frequency of heat release. Therefore, the number of period of pressure fluctuation within the interval between two vortex impacts

decreases and will eventually be reduced to 1, that is, the frequency ratio of vortex shedding and pressure fluctuation becomes 1:1. On each similar curve, the amplitude changes from decrease to increase, which is because the increase of u_0 changes the time of vortex impact and combustion. The time of heat release moves from the peak of pressure oscillation to the previous trough, and then to the previous peak, that is, the phase difference between heat release and pressure oscillation changes. According to Rayleigh's criterion, the change of phase difference leads to a similar structure from decrease to increase in the change process of the amplitude of pressure fluctuation.

4.4 Vortex-acoustic lock-in behaviors

Fast Fourier transform (FFT) was performed for p'/p_0 time series after stable oscillation in 381 cases in Section 4.3, and the dominant frequency corresponding to the maximum amplitude after FFT was taken as the dominant frequency of pressure fluctuation (f_p). According to equation (3.10), the frequency of vortex shedding in steady state is f_{s0}, and the actual frequency of vortex shedding is f_s. The results shown in Fig. 4.8 can be obtained from the frequency ratios f_{s0}/f_p and f_s/f_p.

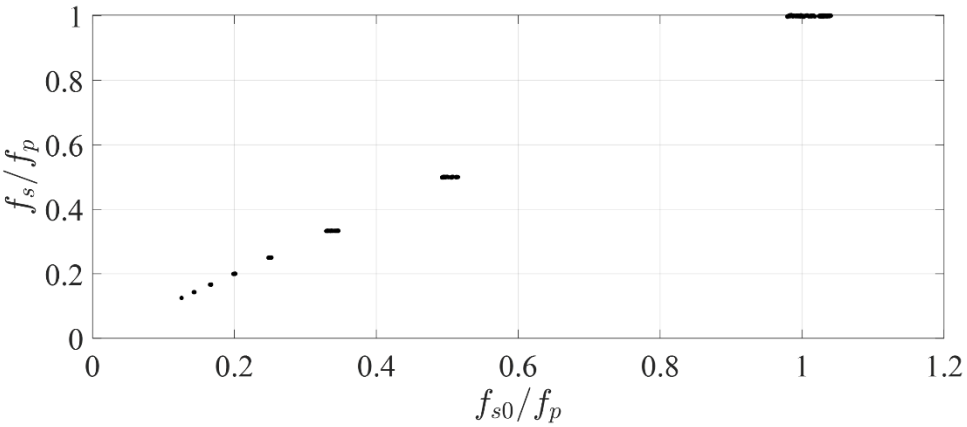

Fig. 4.8 Vortex-acoustic frequency lock-in.

It can be seen from Fig. 4.8 that there is a frequency locking relationship between the dominant frequency of pressure fluctuation f_p and the frequency of vortex shedding f_s, forming a triangular frequency lock-in region as shown in the figure. In Fig. 4.8, there are 8 steps from the upper right to the lower left, and f_s/f_p is 1, 1/2, 1/3,

1/4, 1/5, 1/6, 1/7 and 1/8 in turn. The phenomenon is called vortex-acoustic frequency lock-in, which can be used as an important indicator of periodic combustion oscillation. This phenomenon is essentially due to the stable self-excited oscillation. The thermoacoustic oscillation is a process of interaction between the unstable heat release rate and the fluctuation of acoustic field in the combustion chamber. After the combustion oscillation is stable, a self-sustaining positive feedback loop is formed between the heat release caused by the impact and combustion of the shedding vortex and the fluctuation of the pressure and velocity of the acoustic field, thus forming a stable self-excited oscillation. In the calculation model, the unsteady heat release is caused by vortex shedding, so the frequency of vortex shedding is the key factor affecting the thermoacoustic oscillation. With the change of u_0, the frequency of vortex shedding changes, and then the frequency of heat release changes. When stable self-excited oscillation occurs between heat release and pressure fluctuation, stable thermoacoustic oscillation will appear. Meanwhile, the frequency of vortex shedding and the frequency of pressure fluctuation present frequency locking phenomenon.

Figure 4.9 shows the relationship between f_p and f_s and the variation of f_s/f_p with u_0. It can be seen from the figure that with the increase of u_0, the frequency of vortex shedding (f_s) increases, and the dominant frequency of pressure fluctuation (f_p) develops towards high frequency, while f_s/f_p is close to 1. The increase of u_0 leads to the increase of the frequency of vortex shedding, and then the frequency of heat release increases. From the analysis in Section 4.3, it can be found that the number of period of pressure fluctuation within the interval between two vortex impacts will eventually decrease to 1, so the frequency ratio of vortex-acoustic lock-in eventually tends to 1, which is also in agreement with the explanation in Section 4.3.

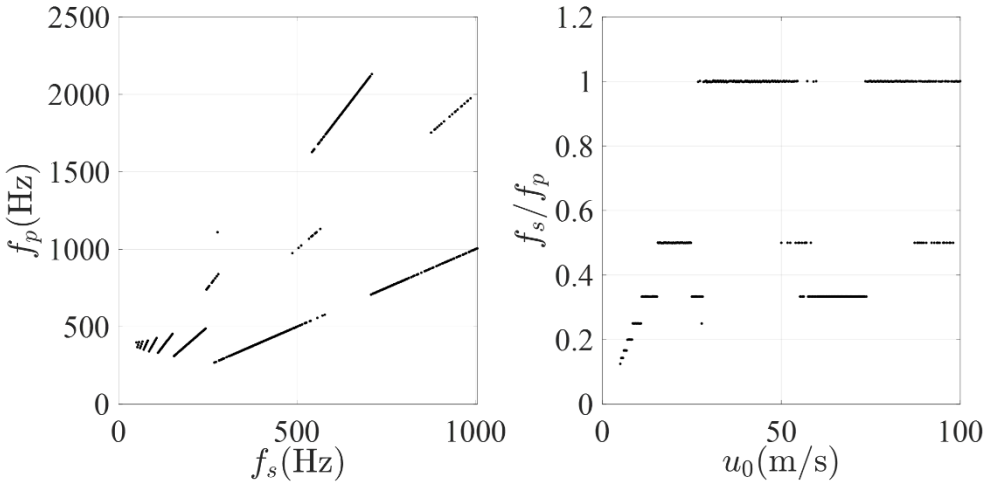

Fig. 4.9 The relationship between f_p and f_s and the variation of f_s/f_p with u_0.

Figure 4.10 shows the $u' - p'/p_0$ phase diagram in six different cases of O1, O2, O3, O4, O5 and O6 in Fig. 4.6. The short vertical line in the phase diagram shows the moment when the shedding vortex impacts and burns, that is, the pressure jumps suddenly, while the velocity remains unchanged. In Fig. 4.10 (a) to (f), f_s/f_p is approximately equal to 1/7, 1/6, 1/5, 1/4, 1/3 and 1/2 respectively. Corresponding, the phase trajectory in $u' - p'/p_0$ phase diagram rotates 7, 6, 5, 4, 3 and 2 times respectively. This phenomenon is in agreement with Fig. 4.6. From Fig. 4.6 (a) to (f), the damped oscillator (pressure fluctuation) experiences 7, 6, 5, 4, 3 and 2 periodic oscillations respectively between the two adjacent shedding vortices impacting and burning. After the oscillation of the system is stable, the damping oscillator is forced by the periodic vortex impact and combustion, and the system can be regarded as coupling of two oscillators. At this point, the system can be treated as discrete system and treated with discrete map. When the two oscillators are coupled, their trajectory in the three-dimensional phase space will be limited to a two-dimensional torus. Phase angle and frequency are the key factors to determine the motion properties of coupled oscillators. Therefore, the proper Poincaré section is selected on torus, and only the Poincaré map on the circle is considered, that is, the circle map. When the second oscillator rotates one cycle on the two-dimensional torus, the number of turns of the first oscillator is the ratio of the frequency of the first oscillator to that of the second

oscillator.

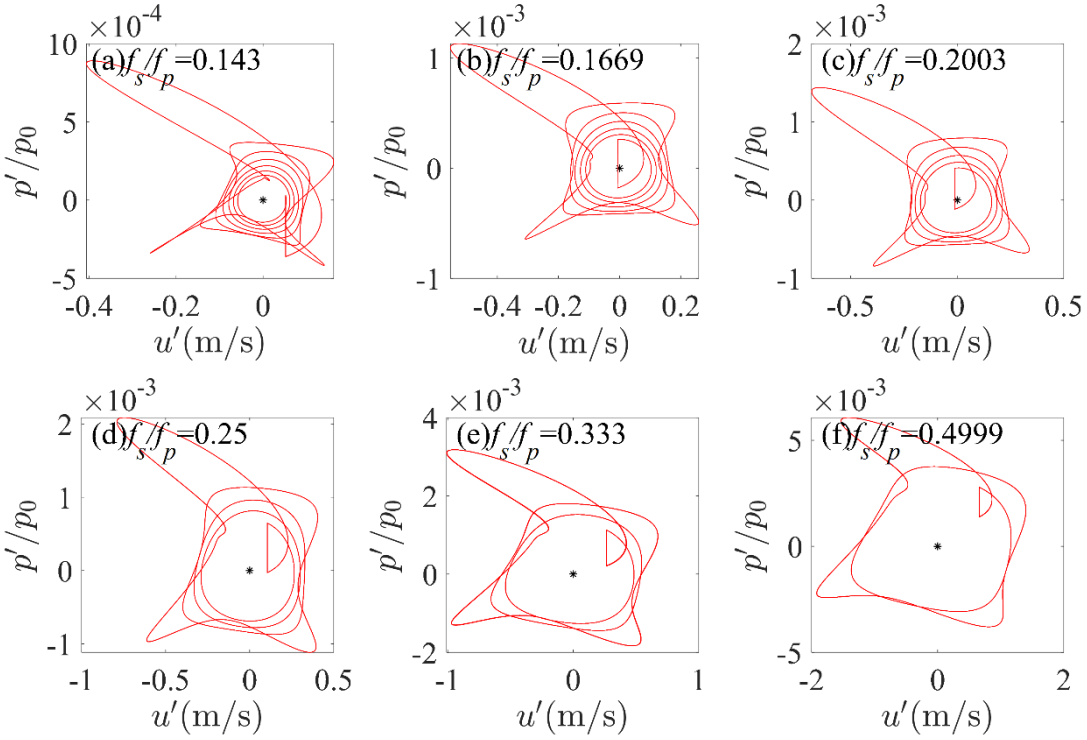

Fig. 4.10 $u' - p'/p_0$ phase diagram at six different frequency ratios.

In this thermoacoustic oscillation system, the number of periodic oscillations of the damping oscillator in the time interval between two vortex impacts is the number of turns of the damping oscillator, in the case that the periodic forced oscillator (vortex impact) rotates for one cycle on the two-dimensional torus. The number of turns of the damping oscillator is the ratio (f_p/f_s) of the dominant frequency of pressure fluctuation (f_p) to the frequency of vortex shedding (f_s). The ratio is also in agreement with the number of turns of the phase trajectory in Fig. 4.10. Meanwhile, the ratio is an integer, so the result of mapping on the selected Poincaré section remains unchanged. The thermoacoustic system oscillates periodically by integer (f_p/f_s) multiple of the frequency (f_s) of the periodic forced oscillator (the vortex impinging frequency), that is, the frequency locking (also called phase locking or mode locking) with the number of revolutions f_p/f_s.

Chapter 5 Frequency-locked behaviors under the condition of fluctuating mainstream velocity

5.1 Numerical simulation

In practice, the mainstream velocity u_0 of the combustion chamber is not necessarily constant. Considering the fluctuation of upstream velocity in combustion chamber, the fluctuation term $u_a \sin(2\pi f_a t)$ is added to the mainstream velocity, among them, u_a is the amplitude of fluctuation and f_a is the frequency of velocity fluctuation. In this section, the influence of fluctuation of upstream velocity in combustion chamber on the thermoacoustic oscillation is studied.

Figure 5.1 shows the combustion chamber with a backward-facing step. Replace u_0 in all equations in Section 3.2 with $u_0 + u_a \sin(2\pi f_a t)$, and other physical quantities remain the same. The calculation process is the same as the numerical simulation in Section 4.1. In the calculation, the damping coefficients are $c_1 = 0.135, c_2 = 0.015$ [15, 23], other parameters are the same as those in Section 4.1. The initial perturbation is zero ($\eta_n(0) = \dot{\eta}_n(0) = 0$).

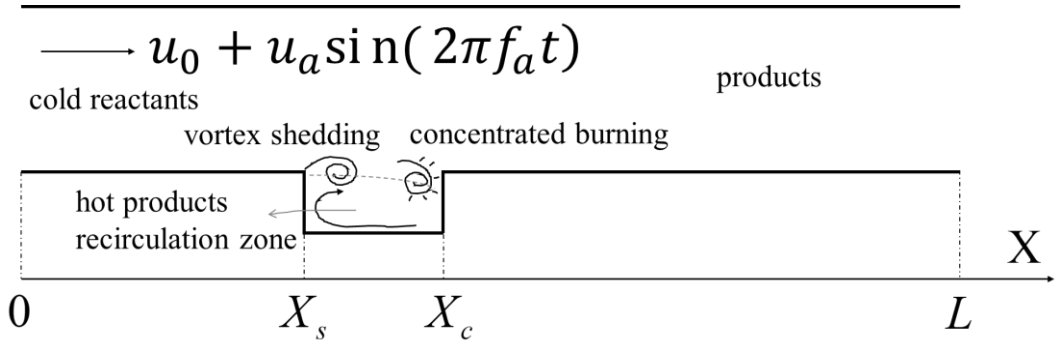

Fig. 5.1 Schematic of the combustion chamber with a backward-facing step.

5.2 Frequency-locked behaviors

In order to study the influence of the frequency (f_a) of velocity fluctuation in the

upstream of combustor on the thermoacoustic system, the mainstream velocity is set to $u_0 + u_a \sin(2\pi f_a t)$. After setting the steady flow velocity $u_0 = 40\text{m/s}$ and the amplitude of fluctuation $u_a = 4\text{m/s}$ as 10% of u_0, 101 cases under the uniform change of f_a from 200Hz to 2200Hz were calculated respectively. According to equation (3.10), the frequency of steady vortex shedding can be obtained as follows, $f_{s0} = 400\text{Hz}$. The actual frequency (f_s) of vortex shedding can be obtained from the average value of the frequency of vortex shedding after the oscillation becomes stable. Figure 5.2 shows the frequency-locked relationship between vortex shedding frequency f_s and the frequency of mainstream velocity fluctuation f_a, as well as the variation of f_s/f_a with f_a. Figure 5.2(b) is a larger version of Fig. 5.2(a). It can be seen that there are five steps in Fig. 5.2(a), and the frequency-locked phenomena with the ratios of f_s and f_a being 1, 1/2, 1/3, 1/4 and 1/5 respectively appear. The corresponding five frequency-locked regions (shown in the gray line in the figure) are respectively close to 1, 2, 3, 4 and 5 times of f_a being f_{s0}. It can be seen from Fig. 5.2(c) that the frequency of vortex shedding does not continuously increase with the frequency of mainstream velocity fluctuation, as f_a tends to high frequency and f_s/f_a tends to 0. In a word, the frequency of vortex shedding does not increase with the increase of the frequency of fluctuating mainstream velocity. When the frequency of fluctuating mainstream velocity (f_a) is a positive integer multiple of the frequency of steady vortex shedding (f_{s0}), a frequency-locked region will appear nearby.

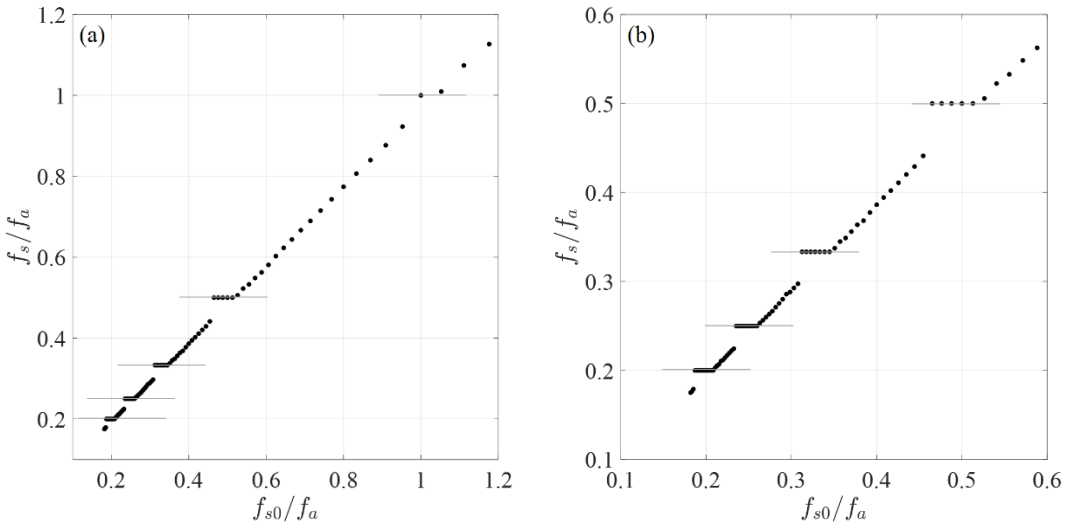

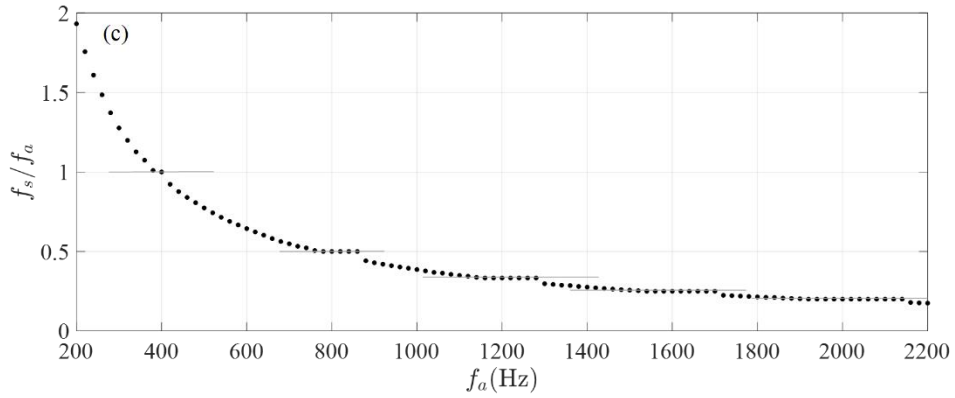

Fig. 5.2 Frequency-locked phenomenon.

The fast Fourier transform (FFT) was carried out for the time series of p'/p_0 after oscillation becomes stable in 101 cases respectively, and the dominant frequency corresponding to the maximum amplitude after FFT was taken as the dominant frequency of pressure fluctuation (f_p). Figure 5.3 shows the influence of the frequency of fluctuating mainstream velocity (f_a) on the frequency of vortex shedding (f_s) and the dominant frequency of pressure fluctuation (f_p).It can be seen that with the increase of f_a, f_s only changes slightly in the range of 380Hz to 440Hz without a continuous increase. When f_a is a positive integer multiple of f_{s0}, f_s is strictly equal to $f_{s0} =$ 400Hz, and a segmented frequency-locking region (shown by the gray slash in the figure) appears near this frequency. In each lock-in region, f_s strictly monotonically increases with the increase of f_a. However, between the frequency-locked regions, f_s hardly changes. In conclusion, when the frequency of fluctuating mainstream velocity is a positive integer multiple of the frequency of steady vortex shedding, the actual frequency of vortex shedding is strictly equal to the frequency of steady vortex shedding. The frequency of vortex shedding increases slightly with the increase of the frequency of fluctuating mainstream velocity only in each lock-in region. Comparing Fig. 5.3 (a) and (b), it can be found that f_p and f_s is almost equal, and they change with f_a in the same way. Because vortex shedding in the thermoacoustic system leads to unstable heat release, the frequency of vortex shedding affects the frequency of unstable heat release. When stable self-excited oscillation occurs between the unsteady heat release and the pressure fluctuation of acoustic field, stable thermoacoustic oscillation occurs.

Therefore, there is a frequency-locked relationship between the frequency of vortex shedding and the frequency of pressure fluctuation in acoustic field. When $u_0 = 40\mathrm{m/s}$, the frequency ratio of the vortex-acoustic lock-in is approximately 1. Therefore, the frequency of pressure fluctuation in the acoustic field in Fig. 5.3 is almost equal to the frequency of vortex shedding.

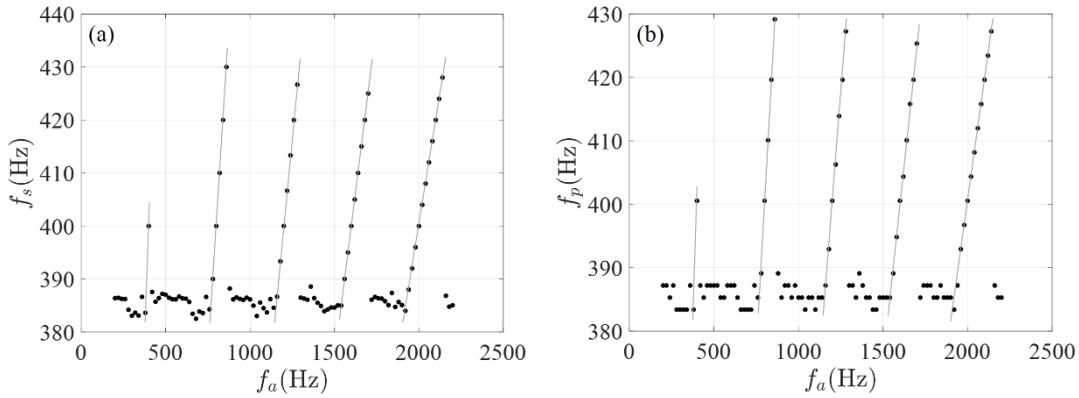

Fig. 5.3 Influence of the frequency of fluctuating mainstream velocity.

5.3 Comparison of results under the conditions of constant and fluctuating mainstream velocity

In order to further study the influence of the mainstream velocity fluctuation on the thermoacoustic oscillation, the two cases of steady mainstream velocity (mainstream velocity equals u_0) and the fluctuating mainstream velocity (mainstream velocity equals $u_0 + u_a \sin(2\pi f_a t)$) were compared. After setting the steady flow velocity $u_0 = 40\mathrm{m/s}$ and the amplitude of fluctuation $u_a = 4\mathrm{m/s}$, the amplitude (Amp) of the stabilized p'/p_0 time series under 101 different f_a in Section 5.2 was calculated respectively, and the change of Amp with f_a was obtained as shown in Fig. 5.4. In the figure, the red dotted line parallel to the X-axis is the amplitude of the mainstream velocity without fluctuation ($u_0 = 40\mathrm{m/s}$), and the region marked by the gray slash is the frequency-locked region. It can be seen that when f_a is a multiple frequency of f_{s0}, the amplitude is almost the same, and much smaller than that when the mainstream velocity is stable. In each individual frequency-locked region, when f_a is small, the amplitude is larger than that when the mainstream velocity is stable. With the increase

of f_a, the amplitude decreases sharply. When f_a is larger than the multiple frequency of f_{s0}, the amplitude further decreases. As f_a develops towards high frequency, the frequency-locked region becomes wider and wider. When the frequency is greater than the multiple frequency of f_{s0}, more f_a can lead to the amplitude of pressure fluctuation much smaller than that when the mainstream velocity is stable.

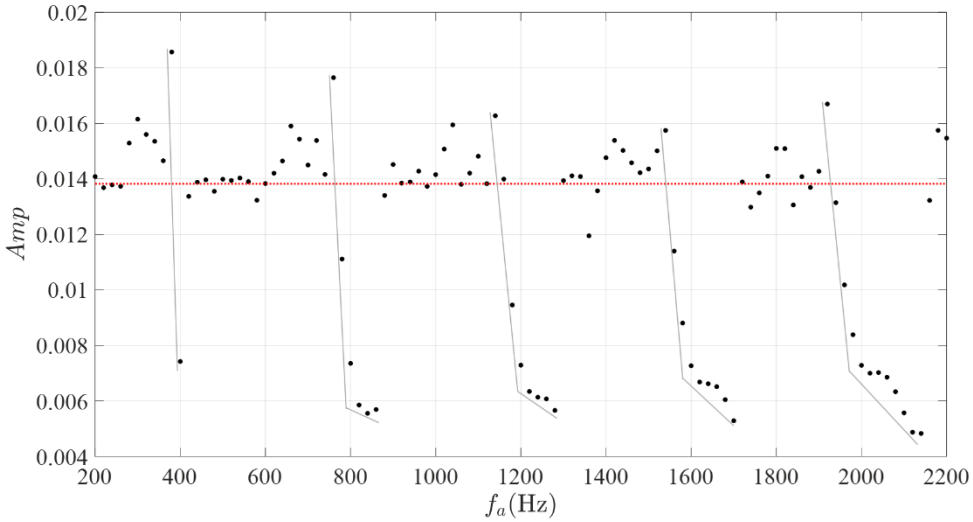

Fig. 5.4 The variation of amplitude with the frequency of fluctuating mainstream velocity.

Figure 5.5 shows the comparison of p'/p_0 time series under the conditions of constant and fluctuating mainstream velocity. Figure 5.5(a) shows the time series when $u_0 = 40\mathrm{m/s}$, and the frequency of vortex shedding is 386Hz. Figure 5.5(b) shows the time series when f_a is 2000Hz, the frequency of vortex shedding is 400Hz, and f_a is 5 times the frequency of steady vortex shedding. Figure 5.5 (c) and (d) are the local enlarged images corresponding to Fig. 5.5 (a) and (b) respectively, in which the black dotted vertical line is the moment when pressure jump caused by the impact and combustion of the shedding vortex. It can be seen that when f_a is the multiple frequency of the frequency of steady vortex shedding, the amplitude of thermoacoustic oscillation is significantly reduced compared with that when the mainstream velocity is stable. Compared with (c) and (d) in Fig. 5.5, the small difference in the frequency of the shedding vortex at the initial stage of the oscillation results in the difference in the phase difference between the heat release and the pressure fluctuation. Meanwhile, the

mainstream velocity added the fluctuation term leads to a small change in the critical circulation, which leads to a small difference in the intensity of heat release. In the two cases of constant and fluctuating mainstream velocity, the amplitude increases continuously to stable, and the amplitude first increases and then decreases until stable, respectively.

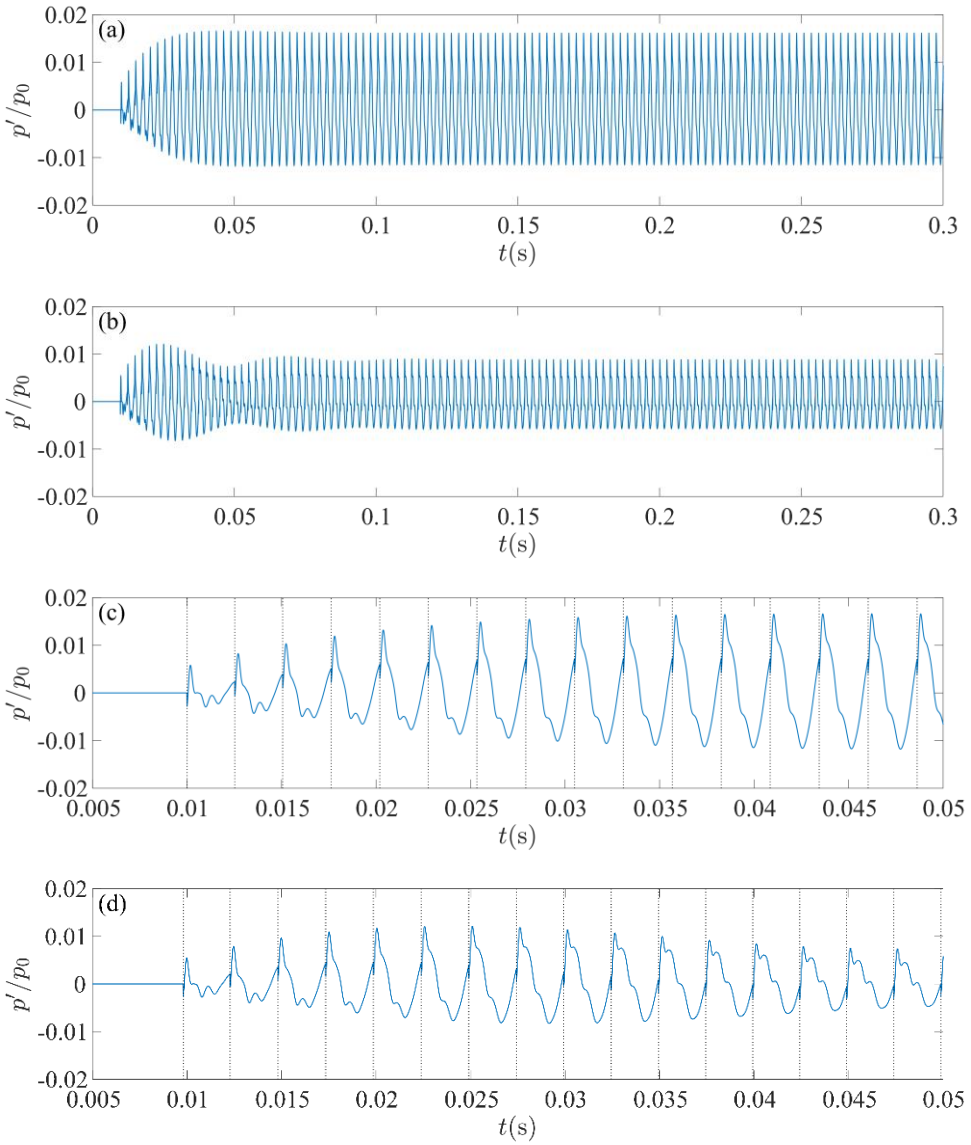

Fig. 5.5 Comparison of time series between steady and fluctuating mainstream velocity.

From the above results, it can be found that the velocity fluctuation in upstream of the combustor has a certain weakening effect on the thermoacoustic oscillation. Adding fluctuation term to the mainstream velocity can be regarded as external excitation. When f_a is the multiple frequency of the frequency of steady vortex shedding (f_{s0}),

the intensity of thermoacoustic oscillation will be weakened. If f_a is larger than the multiple frequency of f_{s0}, and is in the frequency-locked region, the amplitude of thermoacoustic oscillation will be further reduced.

Chapter 6 Study on the influences of harmonic excitation on the thermoacoustic system

6.1 Non-dimensionalization of governing equations

In order to study the influence of parameters on the characteristics of the system more conveniently, the governing equations are non-dimensionalized first. The physical dimensions of model are total length of the tube (L), position of the backward-facing step (X_s), position of the downstream wall of the step (X_c) and the height of the backward-facing step (d). The steady state quantities are mainstream velocity (u_0), average pressure (p_0), average density (ρ_0) and the speed of sound (c_0). The other dimensional quantities are denoted with a tilde above them. In case of non-dimensional quantities the tildes are dropped. Equations (3.10) to (3.16) are expressed by dimensional quantities as follows,

$$\tilde{f}_{s0} = St\frac{u_0}{d} \tag{6.1}$$

$$\frac{d\tilde{r}_j}{d\tilde{t}} = \frac{1}{2}\tilde{u}^2\left(\tilde{t}\right) \tag{6.2}$$

$$\tilde{r}_{sep} = \frac{\tilde{u}\left(\tilde{t}\right)d}{2St} \tag{6.3}$$

$$\frac{d\tilde{x}_j}{d\tilde{t}} = \alpha u_0 + \tilde{u}'\left(\tilde{x}_j,\tilde{t}\right) \tag{6.4}$$

$$\frac{1}{\rho_0}\frac{\partial\tilde{p}'}{\partial\tilde{x}} + \frac{\partial\tilde{u}'}{\partial\tilde{t}} = 0 \tag{6.5}$$

$$\frac{\partial\tilde{p}'}{\partial\tilde{t}} + \gamma p_0\frac{\partial\tilde{u}'}{\partial\tilde{x}} = \left(\gamma-1\right)\tilde{Q} \tag{6.6}$$

$$\tilde{Q} = \beta\sum_j \tilde{r}_j\delta\left(\tilde{t}-\tilde{t}_j\right)\delta\left(\tilde{x}-X_c\right) \tag{6.7}$$

To proceed further, the variables in the above equations governing the vortex shedding process and the acoustic flow field are non-dimensionalized as follows,

$$\begin{aligned} &M = \frac{u_0}{c_0};\ u' = \frac{\tilde{u}'}{u_0};\ p' = \frac{\tilde{p}'}{\gamma M p_0};\ x = \frac{\tilde{x}}{L}; \\ &t = \frac{c_0}{L}\tilde{t};\ f = \frac{L}{c_0}\tilde{f};\ \Gamma_j = \frac{\tilde{\Gamma}_j}{c_0 L};\ \Gamma_{sep} = \frac{\tilde{\Gamma}_{sep}}{c_0 L} \end{aligned} \tag{6.8}$$

where M is the Mach number. Therefore, in case of a steady state flow, the non-dimensional vortex shedding frequency (f_{s0}) is given by,

$$f_{s0} = St\frac{M}{(d/L)} \tag{6.9}$$

The non-dimensional time period of steady-state vortex shedding (t_{s0}) is given by,

$$t_{s0} = \frac{1}{St}\frac{(d/L)}{M} \tag{6.10}$$

The non-dimensional rate of circulation production is expressed as follows,

$$\begin{aligned} &\frac{d\Gamma_j}{dt} = \frac{d\Gamma_j}{d\tilde{t}_j}\frac{d\tilde{t}_j}{d\tilde{t}}\frac{d\tilde{t}}{dt} = \frac{1}{c_0 L}\frac{1}{2}\tilde{u}^2(\tilde{t})\frac{L}{c_0} = \frac{1}{2c_0^2}\left[u_0 + \tilde{u}'(\tilde{t})\right]^2 \\ &= \frac{u_0^2}{2c_0^2}\left[1 + u'(X_s/L, t)\right]^2 = \frac{M^2}{2}\left[1 + u'(X_s/L, t)\right]^2 \end{aligned} \tag{6.11}$$

The non-dimensional critical circulation (Γ_{sep}) is given by,

$$\Gamma_{sep} = \frac{1}{c_0 L}\frac{\tilde{u}(\tilde{t})d}{2St} = \frac{1}{c_0 L}\frac{\left[u_0 + \tilde{u}'(\tilde{t})\right]d}{2St} = \frac{(d/L)}{2St}M\left[1 + u'(X_s/L, t)\right] \tag{6.12}$$

The non-dimensional velocity of the shedding vortex moving downstream can be expressed as follows,

$$\frac{dx_j}{dt} = \frac{dx_j}{d\tilde{x}_j}\frac{d\tilde{x}_j}{d\tilde{t}}\frac{d\tilde{t}}{dt} = \frac{1}{L}\left[\alpha u_0 + \tilde{u}'(\tilde{x}_j, \tilde{t})\right]\frac{L}{c_0} = M\left[\alpha + u'(x_j, t)\right] \tag{6.13}$$

Equations (6.5) and (6.6) can be rewritten as,

$$\frac{1}{\rho_0}\frac{\partial p'}{\partial p'}\frac{\partial p'}{\partial x}\frac{\partial x}{\partial t}+\frac{\partial u'}{\partial u'}\frac{\partial u'}{\partial t}\frac{\partial t}{\partial t}=0 \tag{6.14}$$

$$\frac{\partial p'}{\partial p'}\frac{\partial p'}{\partial t}\frac{\partial t}{\partial t}+\gamma p_0\frac{\partial u'}{\partial u'}\frac{\partial u'}{\partial x}\frac{\partial x}{\partial t}=(\gamma-1)\tilde{Q} \tag{6.15}$$

where heat release rate ($\tilde{Q}$) is given by,

$$\begin{aligned}\tilde{Q}&=\beta\sum_j \Gamma_j\delta(t-t_j)\delta(x-X_c)=\beta\sum_j c_0 L\Gamma_j\delta\left[\frac{L}{c_0}(t-t_j)\right]\delta\left[L(x-X_c/L)\right]\\&=\beta c_0 L\frac{c_0}{L}\frac{1}{L}\sum_j\Gamma_j\delta(t-t_j)\delta(x-X_c/L)=\beta\frac{c_0^2}{L}\sum_j\Gamma_j\delta(t-t_j)\delta(x-X_c/L)\end{aligned} \tag{6.16}$$

Since $p_0=\rho_0 c_0^2/\gamma$, the non-dimensional momentum and energy equations, which govern the acoustic field of the system, are expressed as follows,

$$\frac{1}{\rho_0}\gamma M p_0\frac{\partial p'}{\partial x}\frac{1}{L}+u_0\frac{\partial u'}{\partial t}\frac{c_0}{L}=0$$

$$\frac{\partial p'}{\partial x}+\frac{\partial u'}{\partial t}=0 \tag{6.17}$$

$$\gamma M p_0\frac{\partial p'}{\partial t}\frac{c_0}{L}+\gamma p_0 u_0\frac{\partial u'}{\partial x}\frac{1}{L}=(\gamma-1)\tilde{Q}$$

$$\frac{\gamma M p_0 c_0}{L}\left(\frac{\partial p'}{\partial t}+\frac{\partial u'}{\partial x}\right)=(\gamma-1)\beta\frac{c_0^2}{L}\sum_j\Gamma_j\delta(t-t_j)\delta(x-X_c/L)$$

$$\frac{\partial p'}{\partial t}+\frac{\partial u'}{\partial x}=\frac{(\gamma-1)}{\gamma}\frac{\beta}{M}\frac{c_0}{p_0}\sum_j\Gamma_j\delta(t-t_j)\delta(x-X_c/L) \tag{6.18}$$

By artificially introducing the damping term, equation (6.18) can be written as,

$$\frac{\partial p'}{\partial t}+\frac{\partial u'}{\partial x}+\zeta p'=\frac{(\gamma-1)}{\gamma}\frac{B}{M}\sum_j\Gamma_j\delta(t-t_j)\delta(x-X_c/L) \tag{6.19}$$

where is ζ an artificially added acoustic damping term, and B is an appropriate coefficient of non-dimensional heat release rate.

The non-dimensional partial differential equations (6.17) and (6.19) are reduced to a

set of ordinary differential equations (ODEs) by projecting them onto the space expanded by basis functions using the Galerkin technique. The acoustic mode in the absence of heat source is selected as the basis functions. In order to satisfy the acoustic boundary conditions of open tube at both ends, the Galerkin decomposition of velocity fluctuation (u') and pressure fluctuation (p') are respectively selected as follows,

$$u'(x,t) = \sum_{n=1}^{N} \cos(k_n x) U_n(t) \tag{6.20}$$

$$p'(x,t) = \sum_{n=1}^{N} \sin(k_n x) P_n(t) \tag{6.21}$$

where U_n, P_n are the amplitude of the n-th Galerkin modes and $k_n = n\pi$ is the non-dimensional wave number of the n-th mode. $n = \{1,2,\cdots N\}$, where N is the number of Galerkin modes. The non-dimensional angular frequency of the n-th duct mode is $\omega_n = n\pi$.

Substituting the equations (6.20) and (6.21) into equations (6.17) and (6.19), the following set of ODEs can be obtained,

$$\dot{U}_n + k_n P_n = 0 \tag{6.22}$$

$$\dot{P}_n + 2\zeta_n \omega_n P_n - k_n U_n = 2\frac{(\gamma-1)}{\gamma}\frac{B}{M}\sin\left[k_n (X_c/L)\right]\sum_j \Gamma_j \delta(t-t_j) \tag{6.23}$$

In equation (6.23), the damping term ζ is rewritten as a frequency-dependent damping term ζ_n as follows,

$$\zeta_n = \frac{1}{2\pi}\left[c_1 \frac{\omega_n}{\omega_1} + c_2\sqrt{\frac{\omega_1}{\omega_n}}\right] \tag{6.24}$$

where, c_1 is the damping coefficient which is responsible for the end loses, and c_2 is the damping coefficient which is responsible for the loses due to boundary layers. Substituting $\omega_n = n\pi$ into equation (6.24) gives,

$$\zeta_n = \frac{1}{2\pi}\left[c_1 n + c_2\sqrt{\frac{1}{n}}\right] \tag{6.25}$$

The system of coupled first order differential equations (6.22) and (6.23) can be rewritten as a second order differential equation in U_n as follows,

$$\ddot{U}_n + 2\zeta_n\omega_n\dot{U}_n + k_n^2 U_n = -2k_n\frac{(\gamma-1)}{\gamma}\frac{B}{M}\sin\left[k_n\left(X_c/L\right)\right]\sum_j \Gamma_j\delta\left(t-t_j\right) \tag{6.26}$$

Equation (6.26) represents a kicked oscillator, which behaves like a damped oscillator when the kicks are absent, with the jump conditions at the time of kicking. There is no heat release during the time interval between the two impacts and combustion of vortex. Therefore, the right end of equation (6.26) equals zero, and the system will behave like a damped oscillator. It is assumed that the time instants just before and after the breakdown of the j-th vortex are t_j^- and t_j^+, respectively. Neglecting the effect of damping, the following jump conditions can be obtained by integrating equations (6.22) and (6.23) within the time interval $\left[t_j^-, t_j^+\right]$,

$$\begin{aligned} U_n^+ - U_n^- &= 0 \\ P_n^+ - P_n^- &= 2\frac{(\gamma-1)}{\gamma}\frac{B}{M}\Gamma_j\sin\left[k_n\left(X_c/L\right)\right] \end{aligned} \tag{6.27}$$

When a vortex impinges on the combustor wall, the amplitude of velocity mode U_n remains unchanged, while the amplitude of pressure mode P_n jumps abruptly. The strength of the j-th kick for a fixed geometric configuration is given by $B\Gamma_j/M$.

6.2 Influences of system parameters on the thermoacoustic system

The free parameters of the system can be classified into geometric parameters $\{X_s, X_c, d, L\}$ and flow parameters $\{c_1, c_2, \alpha, St, M, B\}$. In this study, the geometry of the combustor is fixed and only the flow parameters are varied. α is fixed to be 0.6 for all the following cases [37]. The values of the damping coefficients are set as $c_1 =$

$0.315, c_2 = 0.015$, which are same as those given in Sterling and Zukoski [38]. The chosen geometric and flow parameters are shown in Table 6.1. The geometry of the configuration is similar to the one investigated by Chakravarthy et al. [39]. The Mach number investigated is $M \leq 1$, because of the approximation of low Mach number in the study.

Parameter	Symbol	Value
Length of combustor	L	1
Location of vortex separation	X_s	0.3
Location of vortex breakdown	X_c	0.4
Step height	d	0.0224
Vortex convection coefficient	α	0.6
Strouhal number	St	0.14
Damping coefficient	c_1	0.315
Damping coefficient	c_2	0.015

Table 6.1 System parameters chosen for the study.

For the simulation in this chapter, the number of Galerkin modes is set as $N = 32$, which is higher than the number chosen in Chapter 4 and 5. Firstly, the influences of different time steps on the numerical simulation results are studied. The Mach number is set as $M = 0.029$, and the coefficient of non-dimensional heat release rate is set to be $B = 0.048$. The parameters of the system are same as those given in Fig. 4(a,b) in reference [28], so as to verify the validity of the code in this study. Figure 6.1 shows the comparison of the results at different time steps, which are set to be $dt = 10^{-3}, 10^{-4}, 10^{-5}$, respectively. It can be seen from Fig. 6.1 that the time step has a great influence on the simulation results. As the time step increases from 10^{-4} to 10^{-5}, the computed u' and p' change very little. Therefore, 10^{-4} is selected as the time step in all subsequent simulations.

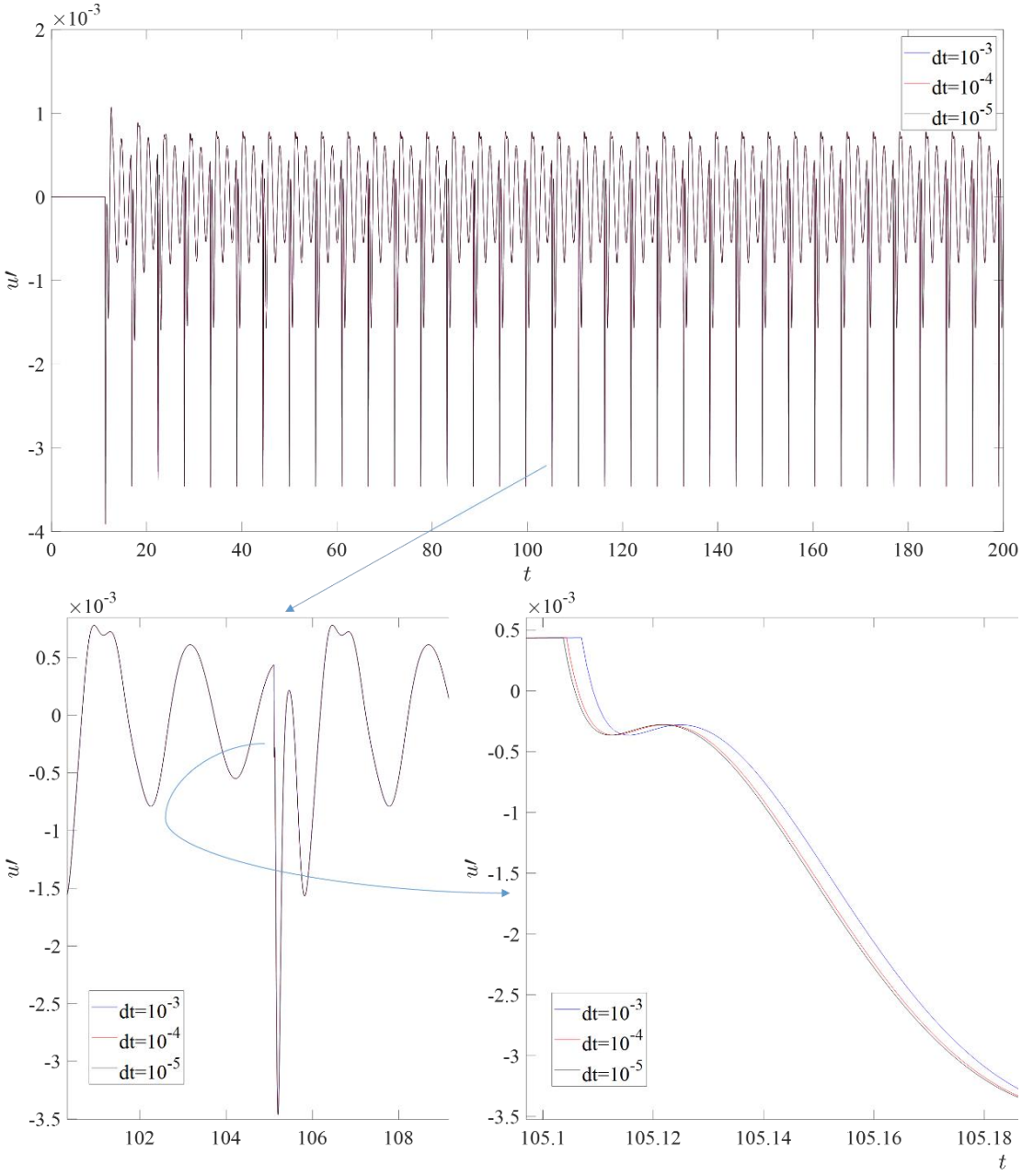

(a) $u' - t$ series

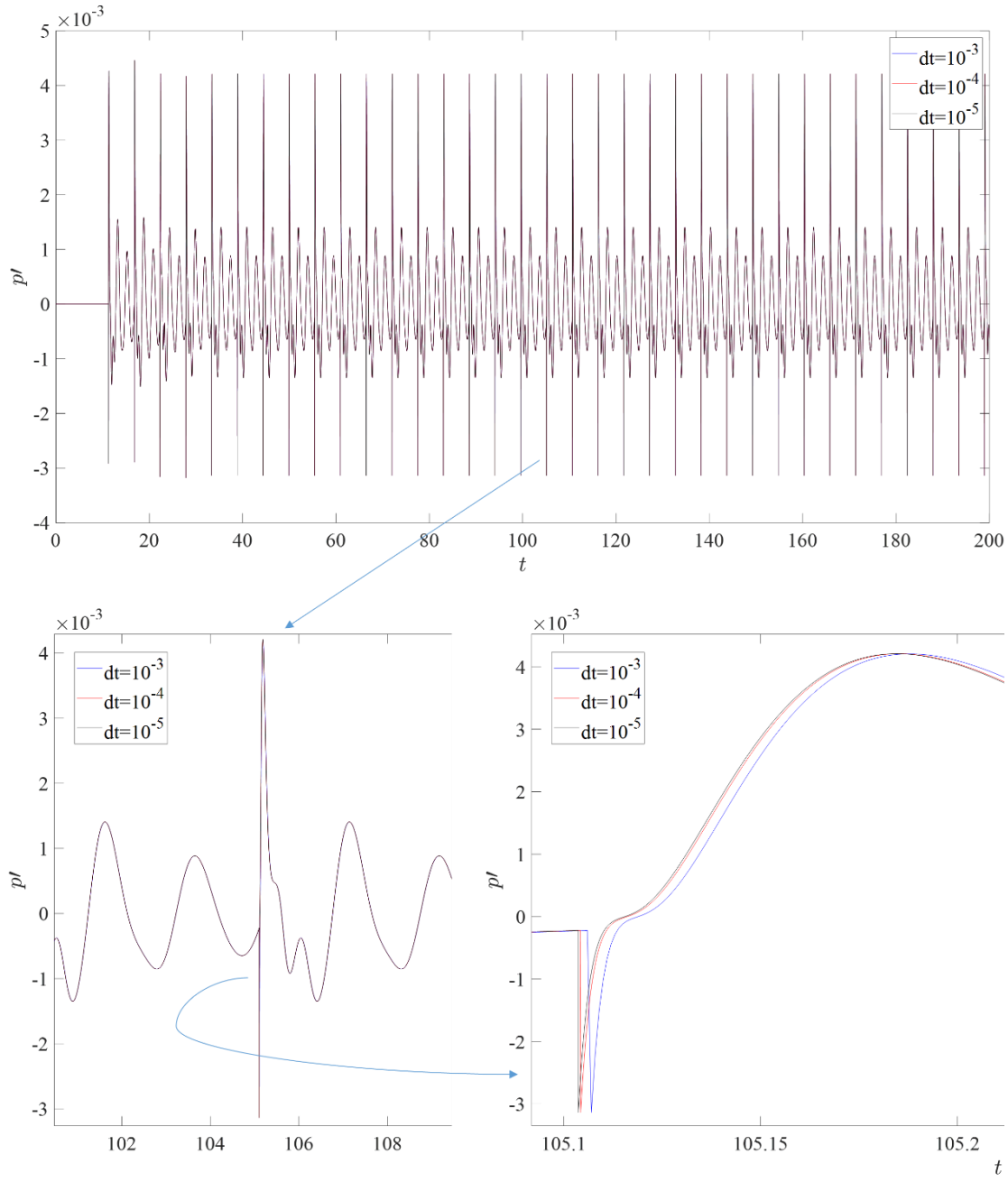

(b) $p' - t$ series

Fig. 6.1 Comparison of the results at different time steps ($dt = 10^{-3}, 10^{-4}, 10^{-5}$).

Next, the influences of different number of Galerkin modes on the numerical simulation results are discussed. Figure 6.2 shows the comparison of the results at different number of Galerkin modes, which are set to be $N = 5,10,15,20,25,32,40,48$, respectively. It can be seen from Fig. 6.2(a) that the computed u' change very little, as the number of Galerkin modes $N \geq 15$. However, the computed u' at the moment of

vortex breakdown is quite different under different number of modes. In Fig. 6.2(b), the computed p' change very little, as the number of Galerkin modes $N \geq 20$. However, different number of modes lead to different computed p' at the moment of vortex breakdown. Except at the moment of vortex breakdown, the simulation results will not be affected, as the mode number $N \geq 20$. Therefore, in this chapter, the mode number is set as $N = 32$ in the simulations.

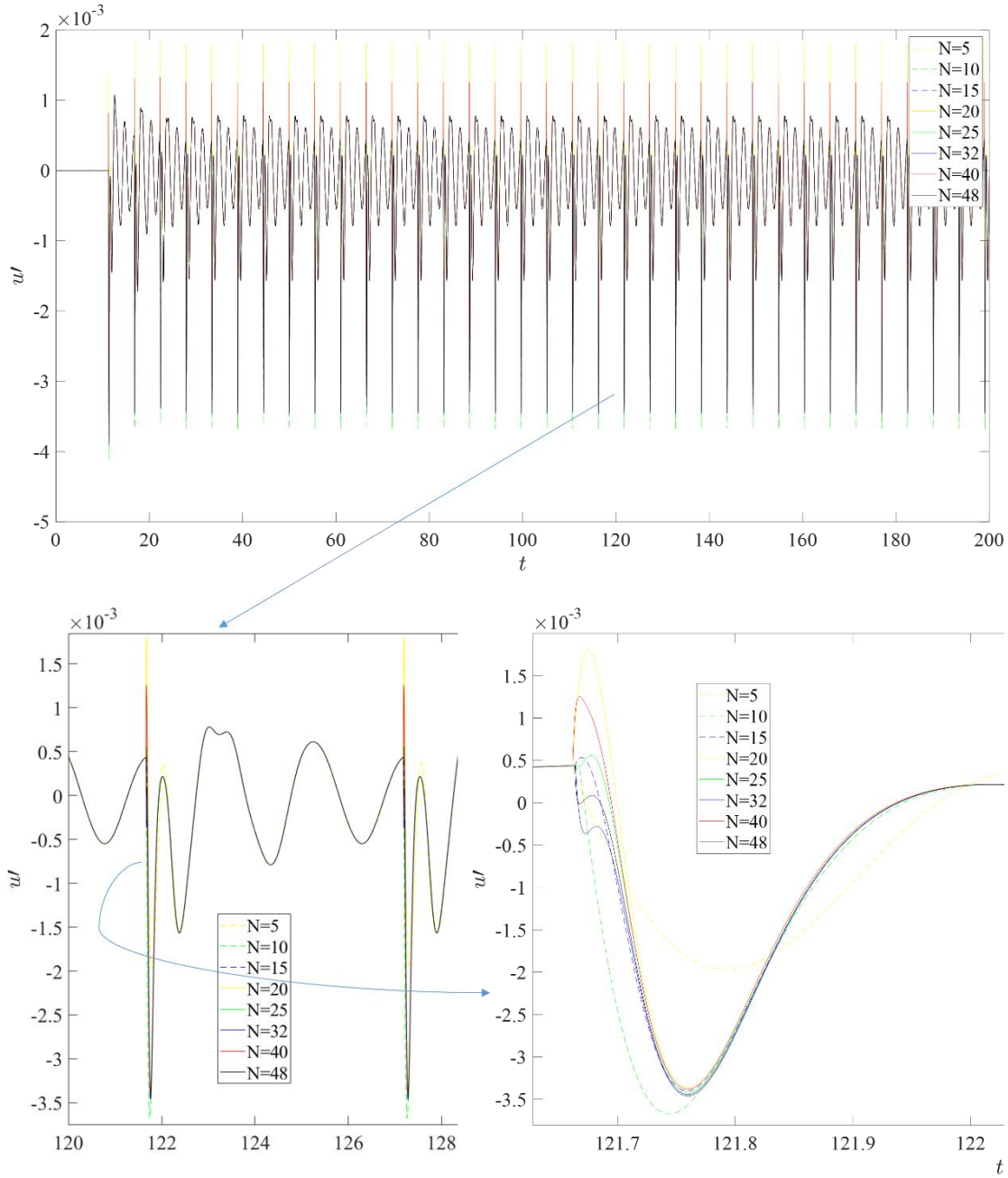

(a) $u' - t$ series

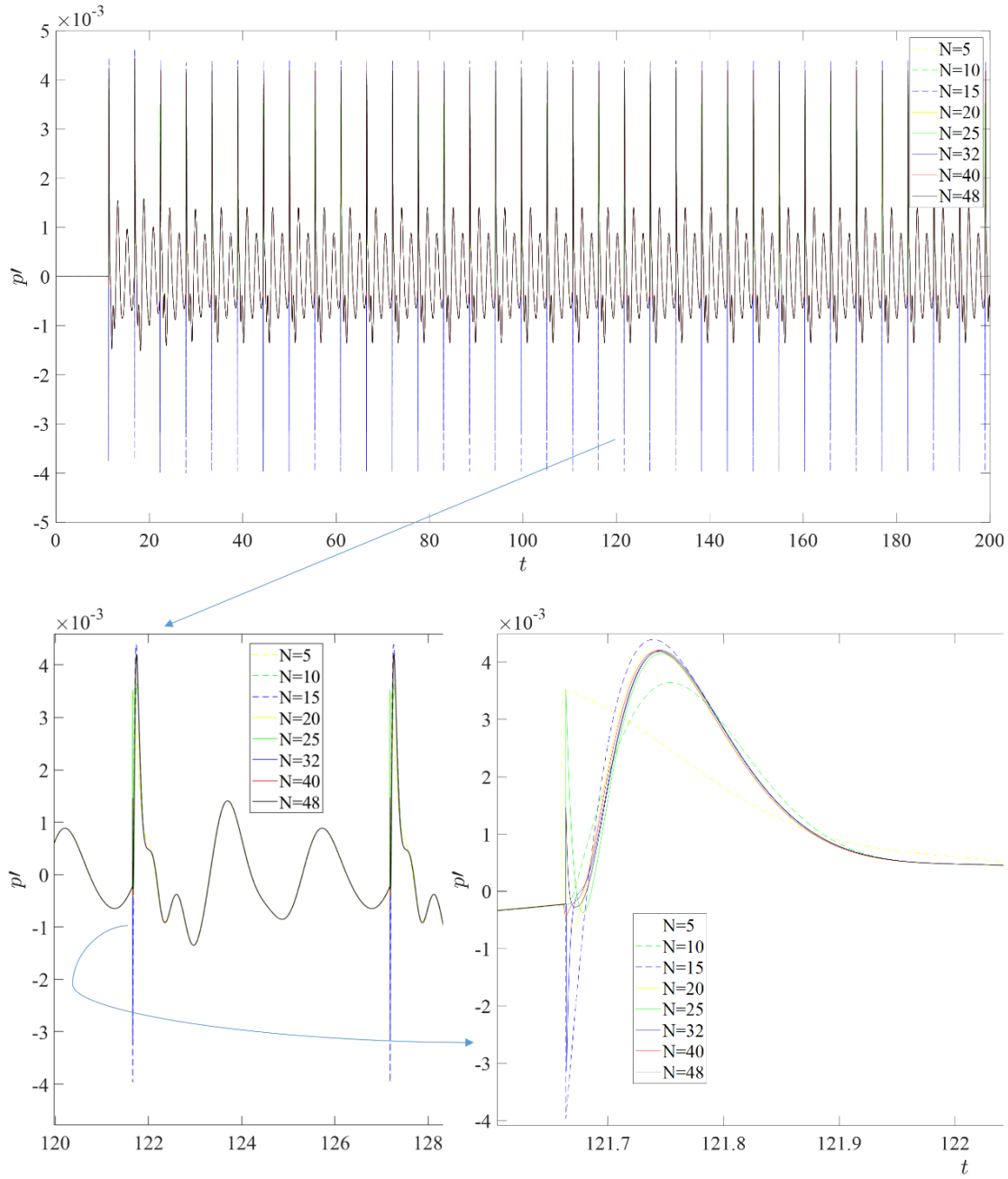

(b) $p' - t$ series

Fig. 6.2 Comparison of the results at different number of Galerkin modes ($N = 5,10,15,20,25,32,40,48$).

M and B are two key parameters of the system, so their influences on the system is discussed in this section. B is fixed at 0.5, and $M = 0.01, 0.02, 0.03, 0.04, 0.05, 0.06, 0.07, 0.08, 0.09, 0.1$, respectively. Figure 6.3 shows the $u' - t$ series at different M. We can see that the value of M mainly affects the

frequency of the thermoacoustic oscillation, but hardly affects the amplitude of the thermoacoustic oscillation. The conclusion is agreement with Section 4.3. M mainly determines the frequency of vortex shedding. The steady-state frequency of vortex shedding increases with the increase of M.

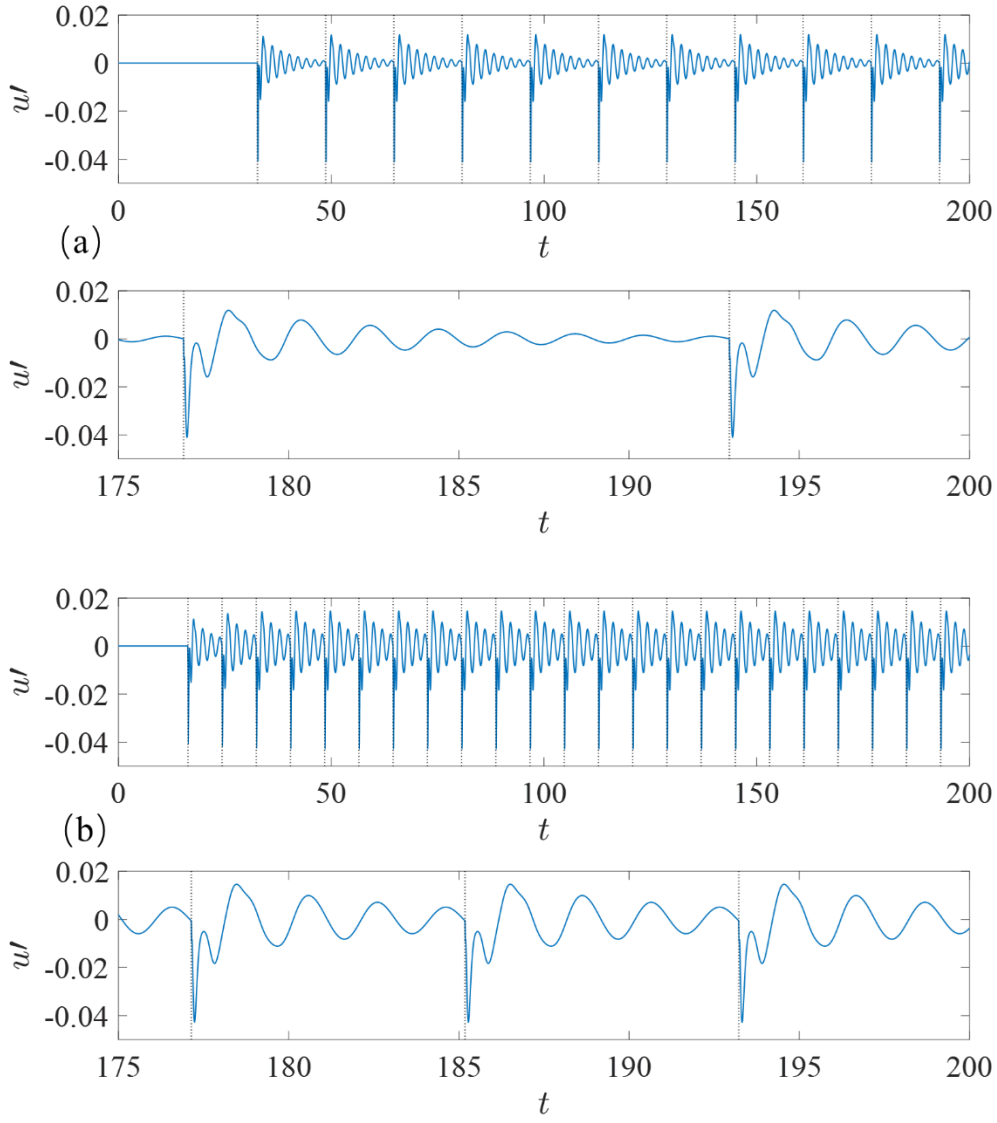

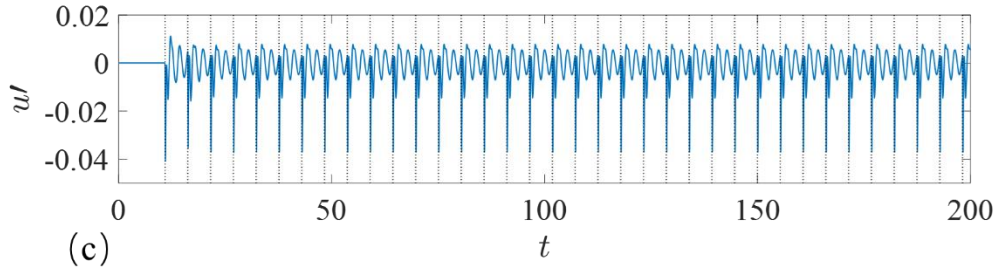
0.02
0
-0.02
-0.04
u
0
50
100
150
200
t

(c)

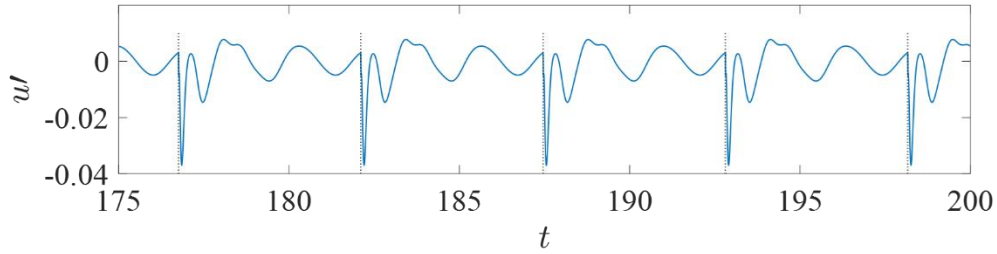
0
-0.02
-0.04
u
175
180
185
190
195
200
t

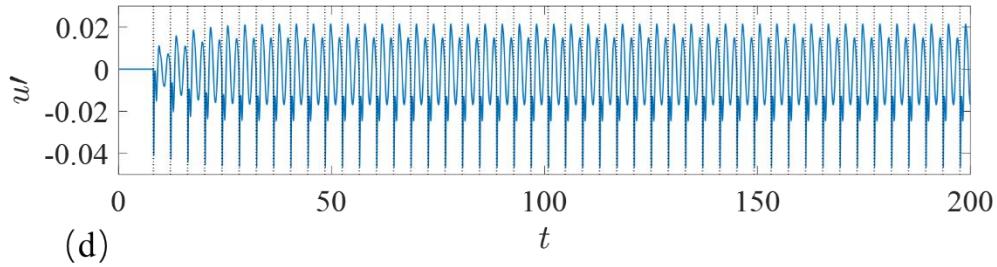
0.02
0
-0.02
-0.04
u
0
50
100
150
200
t

(d)

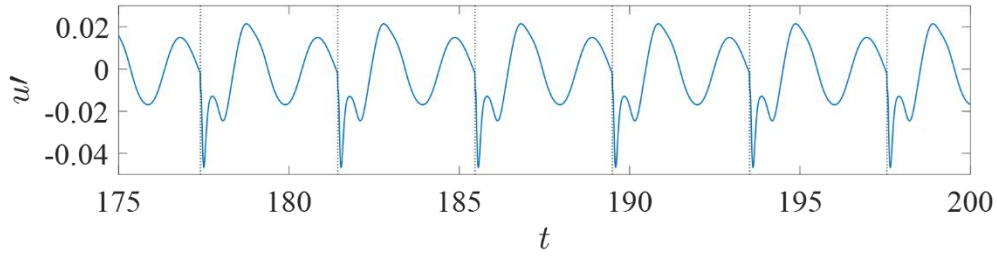
0.02
0
-0.02
-0.04
u
175
180
185
190
195
200
t

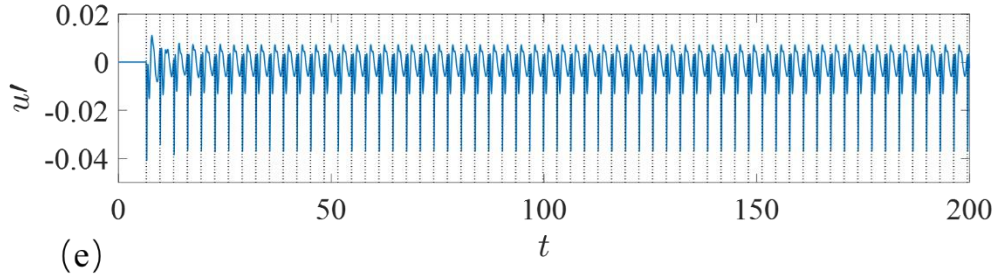
0.02
0
-0.02
-0.04
u
0
50
100
150
200
t

(e)

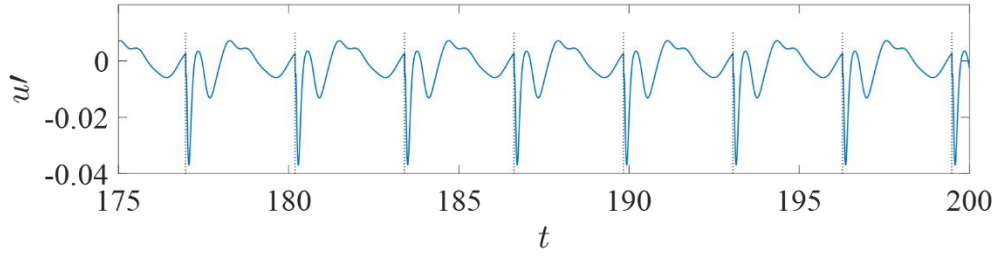
0
-0.02
-0.04
u
175
180
185
190
195
200
t

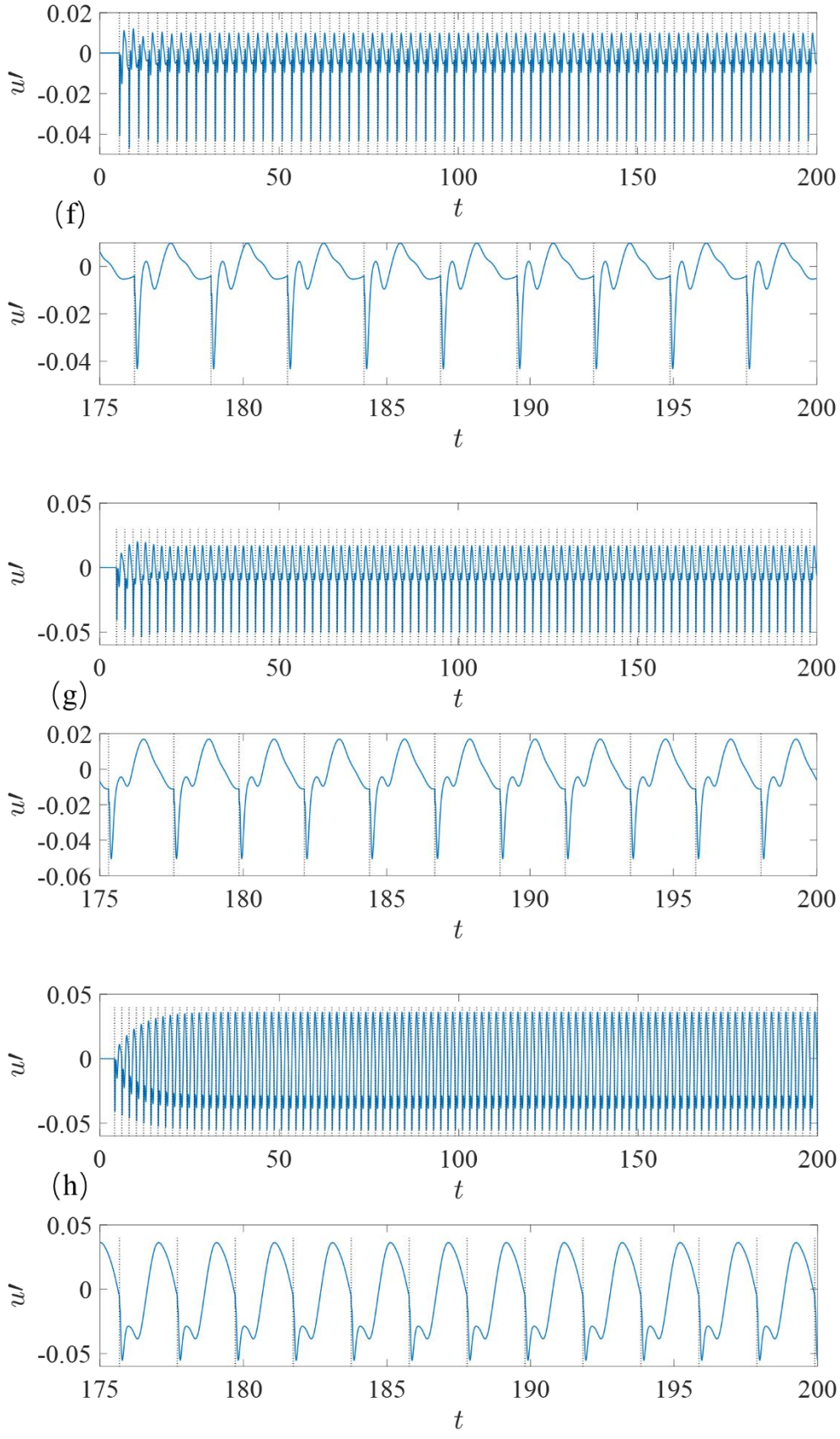
0.02
0
-0.02
-0.04
0
50
100
150
200
t
(f)
0
-0.02
-0.04
175
180
185
190
195
200
t
0.05
0
-0.05
0
50
100
150
200
t
(g)
0.02
0
-0.02
-0.04
-0.06
175
180
185
190
195
200
t
0.05
0
-0.05
0
50
100
150
200
t
(h)
0.05
0
-0.05
175
180
185
190
195
200
t

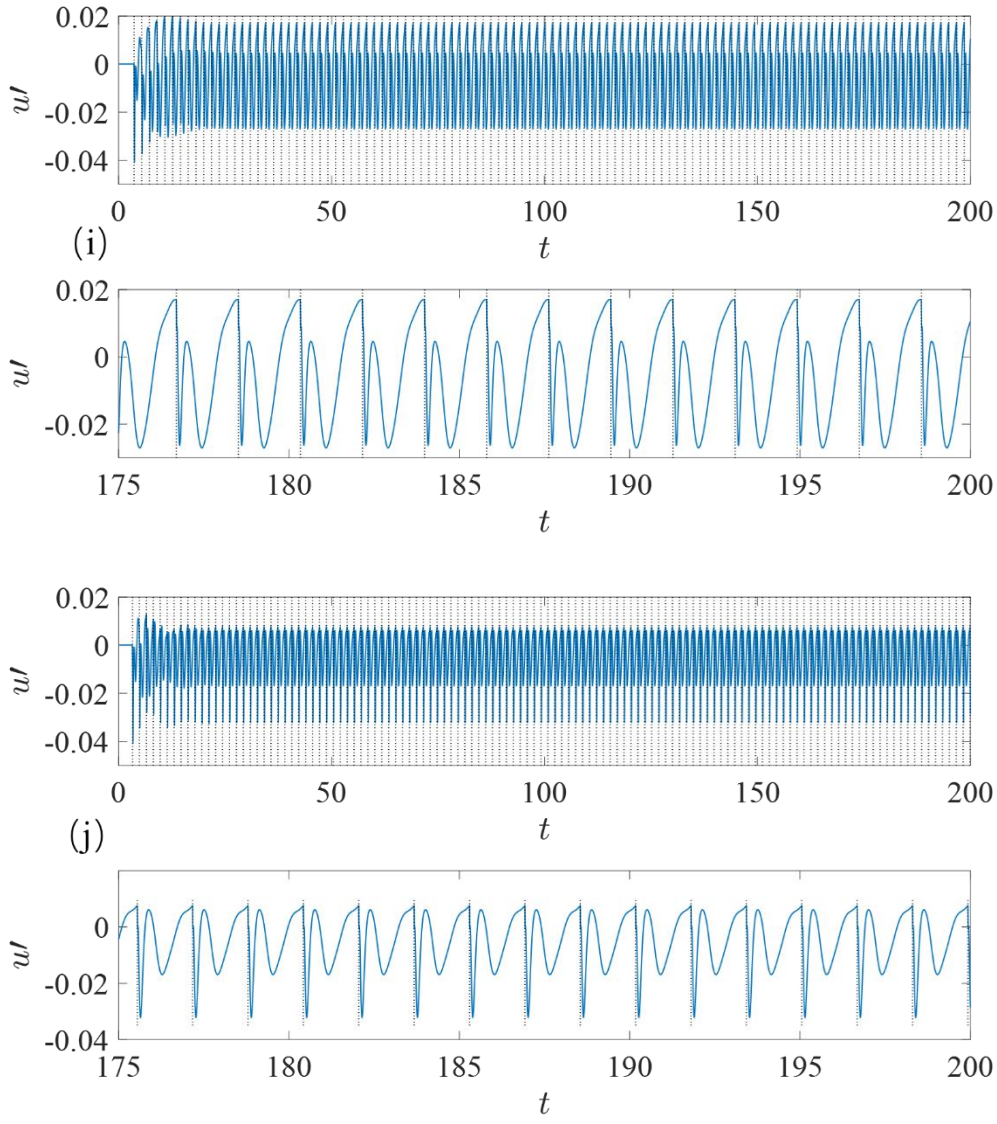

Fig. 6.3 The $u' - t$ series at different M (M =(a)0.01, (b)0.02, (c)0.03, (d)0.04, (e)0.05, (f)0.06, (g)0.07, (h)0.08, (i)0.09, (j)0.1).

Next, M is fixed at 0.05, and $B = 0.01, 0.05, 0.1, 0.25, 0.5, 0.75, 1, 1.33, 1.66, 2$, respectively. Figure 6.4 shows the $u' - t$ series and $p' - t$ series at different B. We can see that the value of B mainly affects the heat release as the vortex breakdown, but hardly affects the frequency of the thermoacoustic oscillation. In other words, B mainly affects the amplitude of pressure jump. The larger B is, the more heat is released, and the greater the amplitude of pressure jump is.

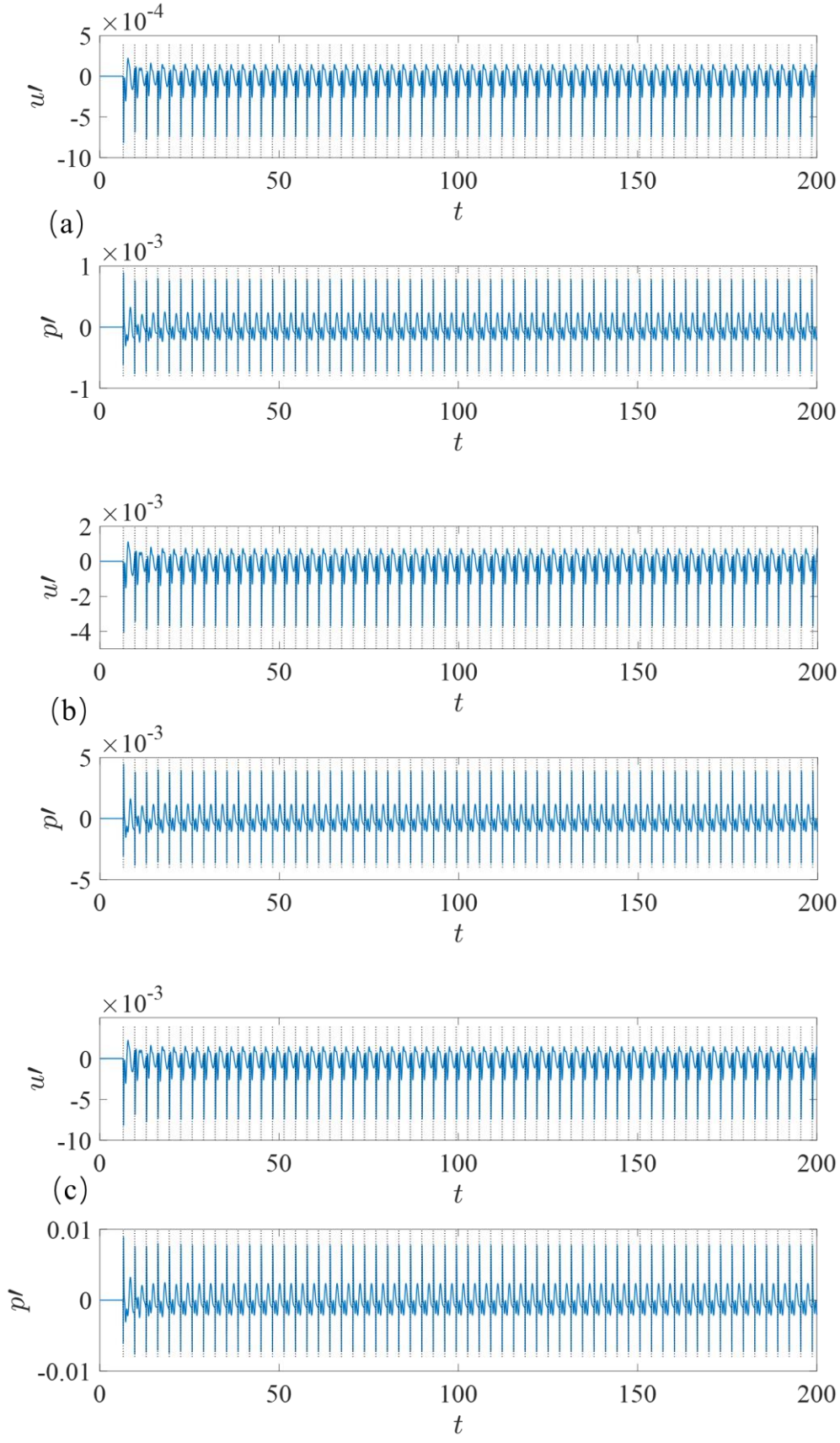
×10^-4
5
0
-5
-10
u′
0
50
100
150
200
t
(a)
×10^-3
1
0
-1
p′
0
50
100
150
200
t
×10^-3
2
0
-2
-4
u′
0
50
100
150
200
t
(b)
×10^-3
5
0
-5
p′
0
50
100
150
200
t
×10^-3
0
-5
-10
u′
0
50
100
150
200
t
(c)
0.01
0
-0.01
p′
0
50
100
150
200
t

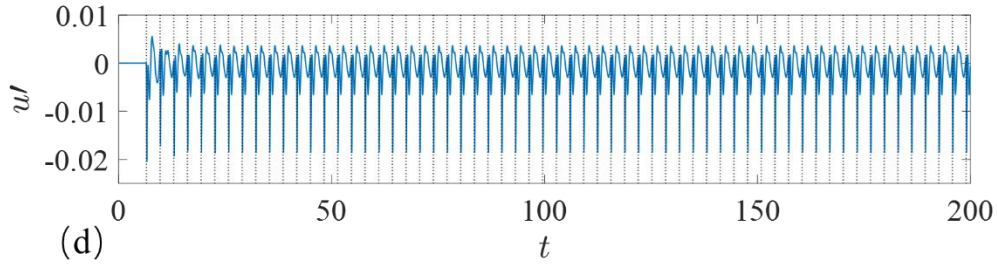
0.01
0
-0.01
-0.02
u′
0
50
100
150
200
t

(d)

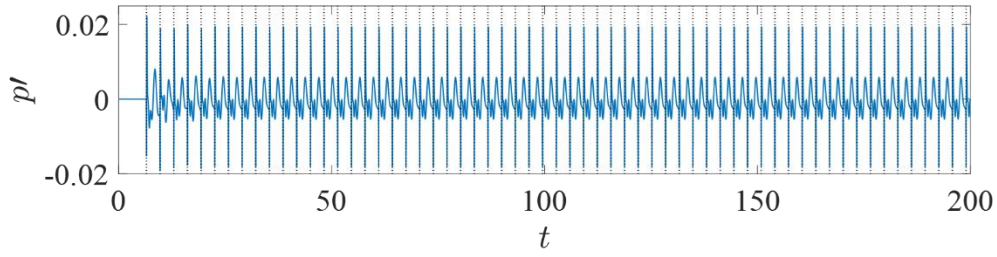
0.02
0
-0.02
p′
0
50
100
150
200
t

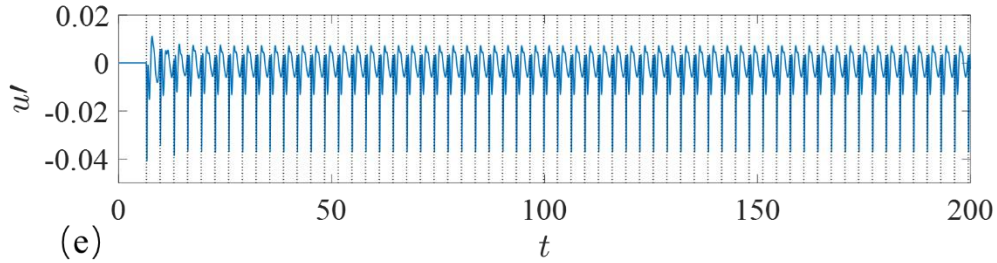
0.02
0
-0.02
-0.04
u′
0
50
100
150
200
t

(e)

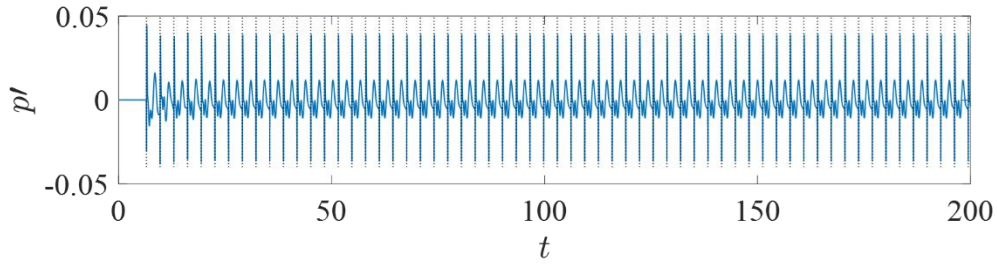
0.05
0
-0.05
p′
0
50
100
150
200
t

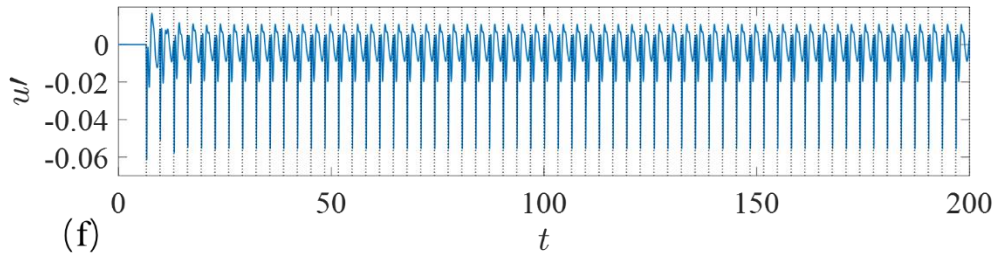
0
-0.02
-0.04
-0.06
u′
0
50
100
150
200
t

(f)

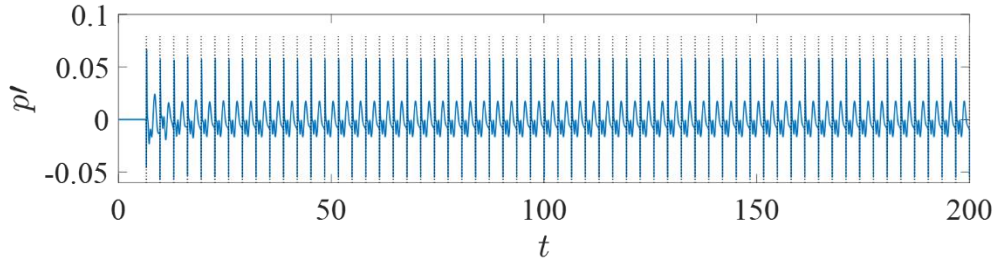
0.1
0.05
0
-0.05
p′
0
50
100
150
200
t

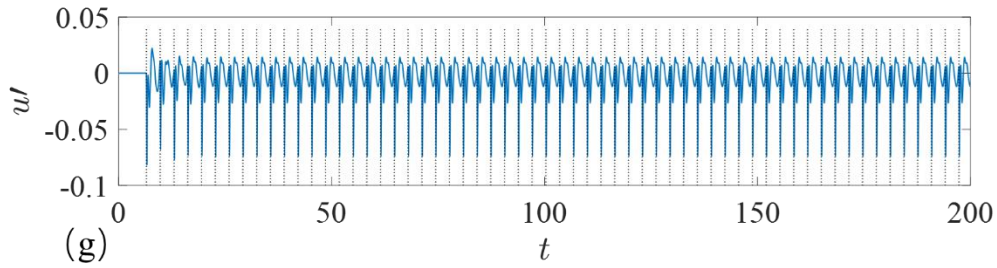
0.05
0
-0.05
-0.1
u′
0
50
100
150
200
t

(g)

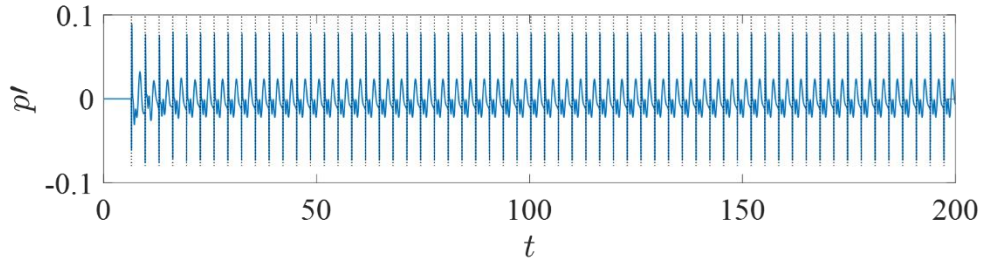
0.1
0
-0.1
p′
0
50
100
150
200
t

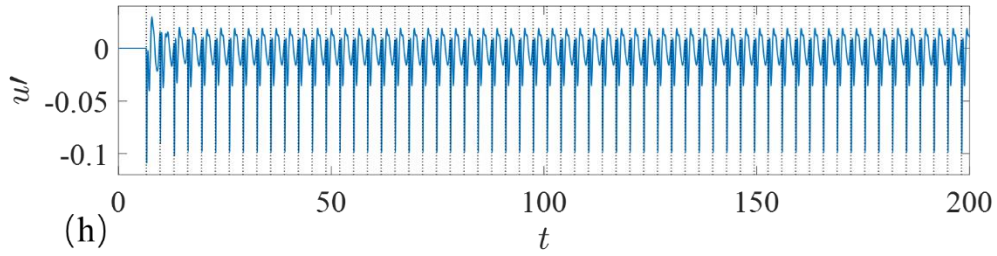
0
-0.05
-0.1
u′
0
50
100
150
200
t

(h)

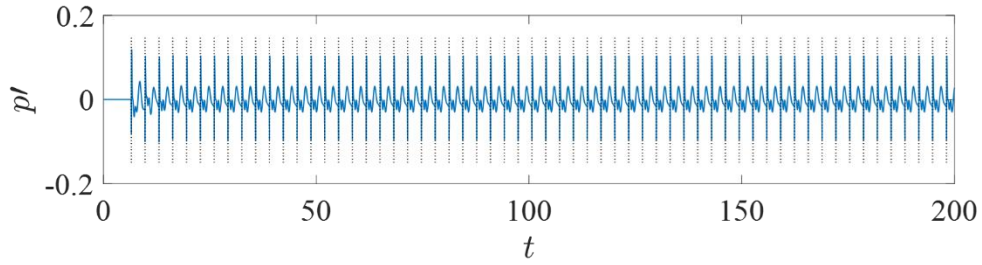
0.2
0
-0.2
p′
0
50
100
150
200
t

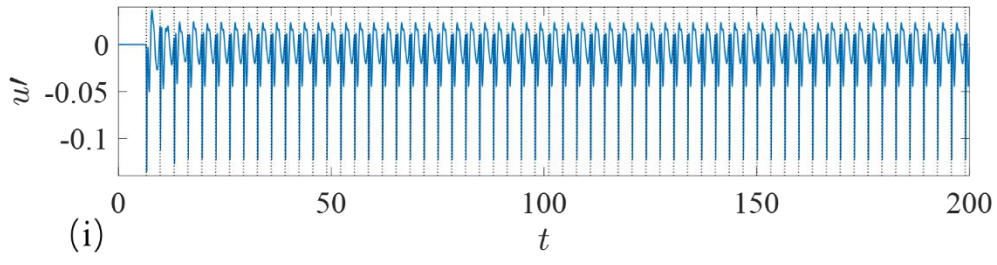
0
-0.05
-0.1
u′
0
50
100
150
200
t

(i)

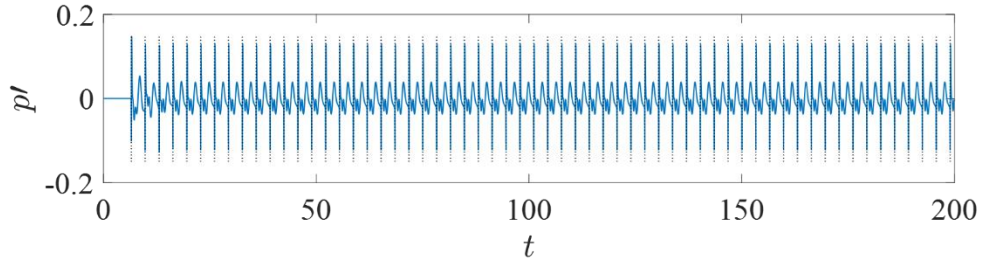
0.2
0
-0.2
p′
0
50
100
150
200
t

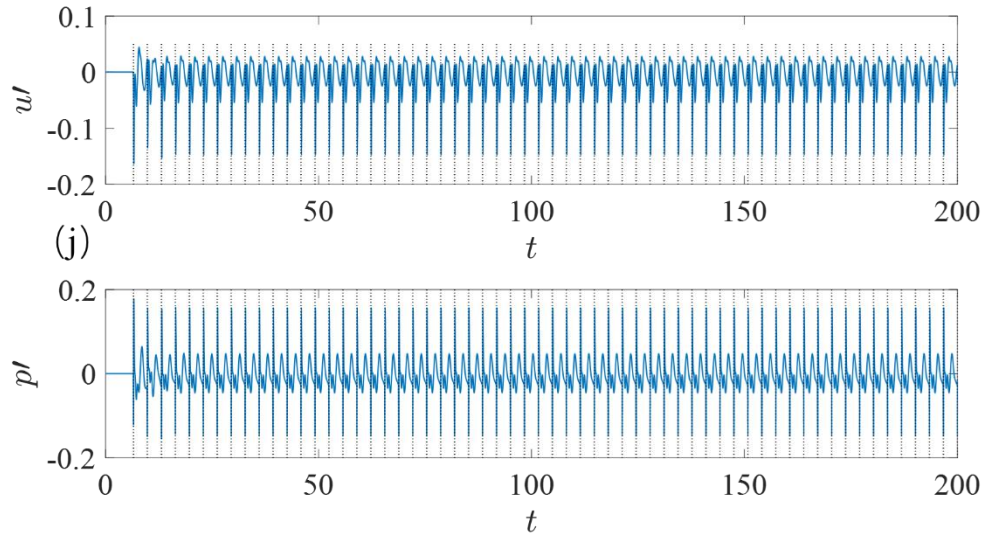

Fig. 6.4 The $u'-t$ series and $p'-t$ series at different B (B =(a)0.01, (b)0.05, (c)0.1, (d)0.25, (e)0.5, (f)0.75, (g)1, (h)1.33, (i)1.66, (j)2).

6.3 Influences of harmonic excitation on the thermoacoustic system

In the early stage, Kashinath and Waugh [40, 41] studied the horizontal Rijke tube with external excitation and proposed how to add external excitation to the mathematical model. Kashinath et al. showed that this excitation could be achieved by placing a loudspeaker in the Rijke tube. Gopalakrishnan [42] verified that the model is in good agreement with the experimental results. Similar to the horizontal Rijke tube with external excitation, the governing equation of the model with external excitation is as follows,

$$\dot{U}_n + k_n P_n = 0 \tag{6.28}$$

$$\begin{aligned} &\dot{P}_n + 2\zeta_n \omega_n P_n - k_n U_n \\ &= 2\frac{(\gamma-1)}{\gamma}\frac{B}{M}\sin\left[k_n\left(X_c/L\right)\right]\sum_j \Gamma_j \delta\left(t-t_j\right) + A_n \sin\left(2\pi f_e t + \phi_e\right) \end{aligned} \tag{6.29}$$

The system of coupled first order differential equations (6.28) and (6.29) can be rewritten as a second order differential equation in U_n as follows,

$$\ddot{U}_n + 2\zeta_n \omega_n \dot{U}_n + k_n^2 U_n = -2k_n \frac{(\gamma-1)}{\gamma} \frac{B}{M} \sin\left[k_n (X_c/L)\right] \sum_j \Gamma_j \delta(t-t_j) - k_n A_n \sin(2\pi f_e t + \phi_e) \tag{6.30}$$

where A_n, f_e and ϕ_e denote the non-dimensional amplitude, frequency and initial phase of the harmonic excitation, respectively. Neglecting the effect of damping, the same jump conditions as equation (6.27) can be obtained by integrating equations (6.28) and (6.29) within the time interval $\left[t_j^-, t_j^+\right]$.

In the simulation of this section, the selection of system parameters is the same as that in Table 6.1. The Mach number is set as $M = 0.05$, and B is set to be 1. The influence on each mode is different, as the excitation is placed in different positions in the tube. For the convenience of the study, the non-dimensional amplitude of the harmonic excitation $A_1 = A$, $A_n = 0 (n \neq 1)$. Actually, it can be achieved by placing the loudspeaker in the middle of the tube. The initial phase of the harmonic excitation is set as $\phi_e = 0$. Firstly, the influences of the frequency of sinusoidal excitation on the thermoacoustic system is studied. A is fixed at 0.1, and $f_e = 0.1, 0.5, 1, 1.5, 3, 5$, respectively. Figure 6.5 shows the $u' - t$ series at different f_e. We can see that the frequency of vortex shedding is almost constant with the change of frequency f_e, at this amplitude $A = 0.1$. Comparing Fig. 6.5 (a) (c) (d) with Fig. 6.4 (g), it can be seen that the amplitude of u' under these three frequencies of excitation is slightly larger than that without excitation. While, comparing Fig. 6.5 (e) (f) with Fig. 6.4 (g), it can be seen that the amplitude of u' under these two frequencies of excitation is almost the same as that without excitation. Especially, it can be seen from Fig. 6.5 (b) and Fig. 6.4 (g) that the amplitude of u' at this frequency of excitation is obviously larger than that without excitation, and the thermoacoustic oscillation is enhanced at this frequency of excitation.

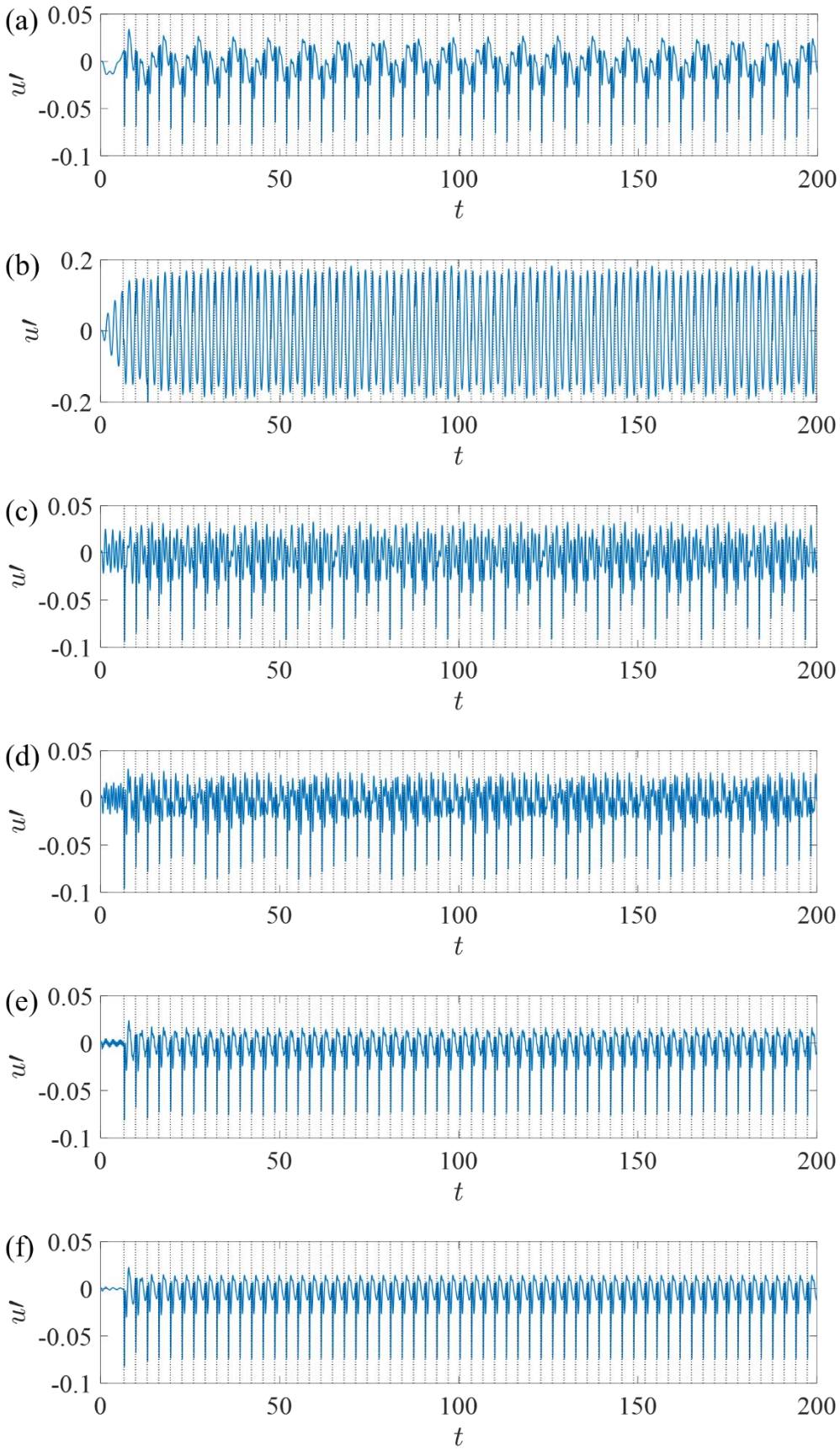

Fig. 6.5 The $u'-t$ series at different f_e (f_e =(a)0.1, (b)0.5, (c)1, (d)1.5, (e)3, (f)5).

Figure 6.6 shows the $p' - u'$ phase diagram at different f_e and the corresponding Poincaré section. In Fig. 6.6, the pictures on the left is the $p' - u'$ phase diagram, and the pictures on the right is the Poincaré section, which is taken at intervals of $1/f_e$. In Fig. 6.6 (a) (d) (e) (f), with the increase of time, the points on the Poincaré section will eventually form a closed curve, which indicates that the system of thermoacoustic oscillation has a quasi-periodic solution. While in Fig. 6.6 (b) and (c), with the increase of time, there are finite points on the Poincaré section, which indicates that the system of thermoacoustic oscillation has periodic solution. It can be seen from Fig. 6.6 that the system changes from quasi-periodic oscillation to periodic oscillation, and then to quasi-periodic oscillation, with the increase of frequency of excitation.

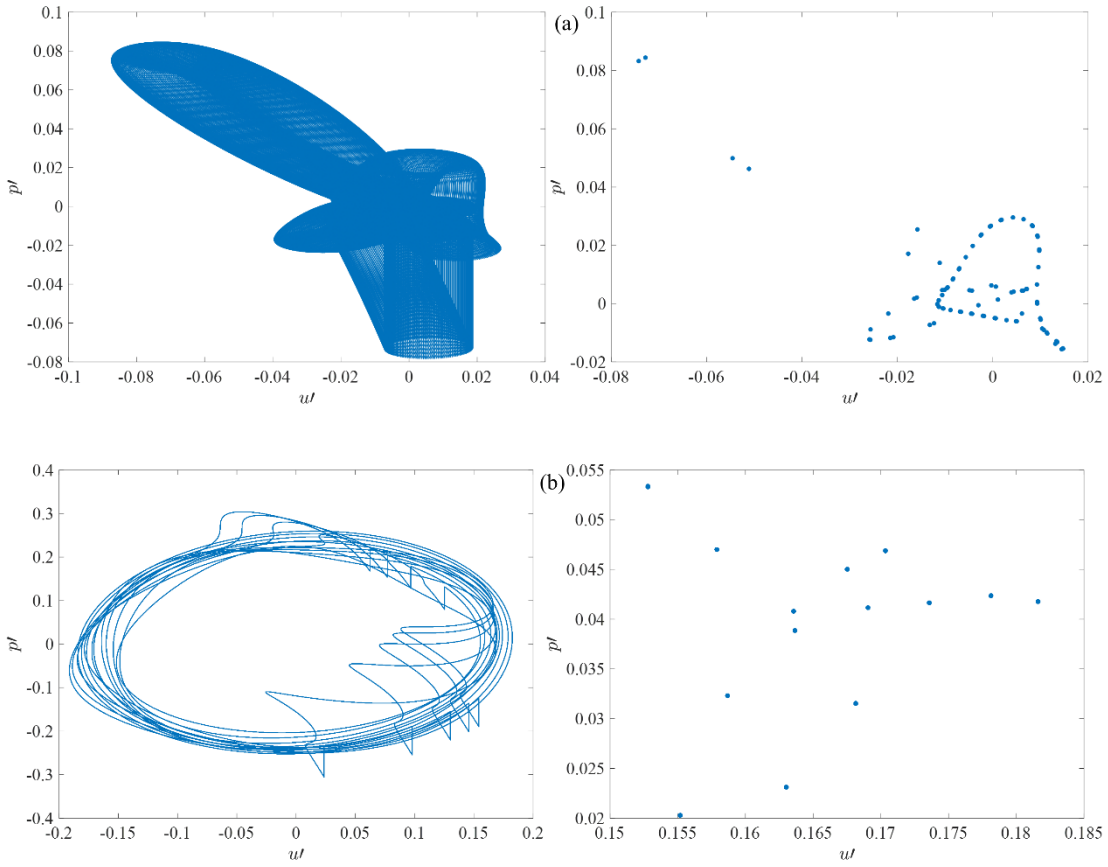

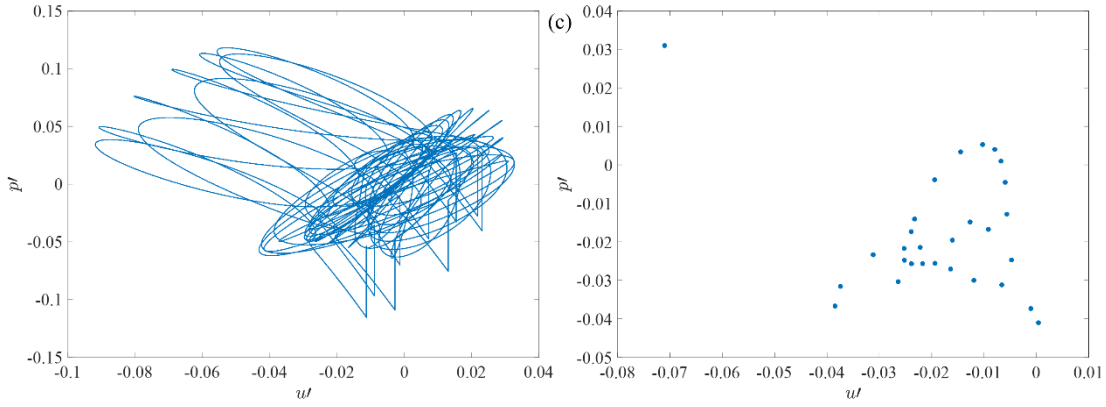
(c)
p′
u′

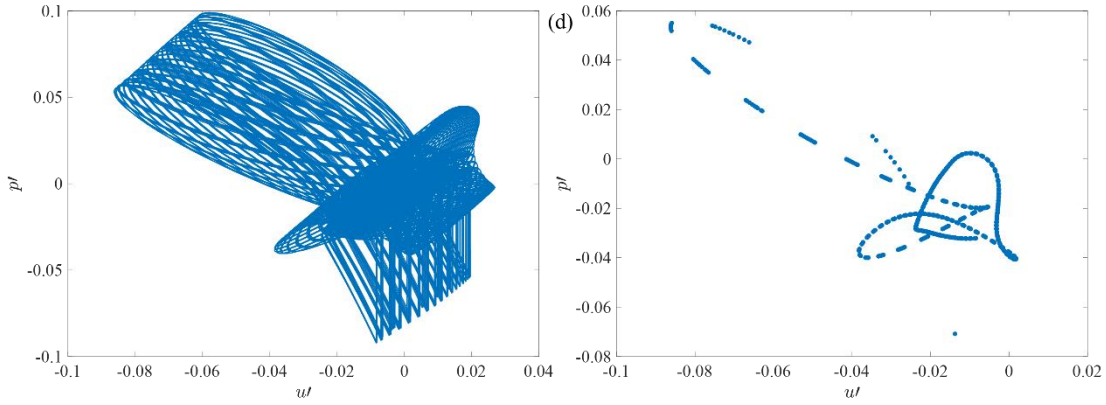
(d)
p′
u′

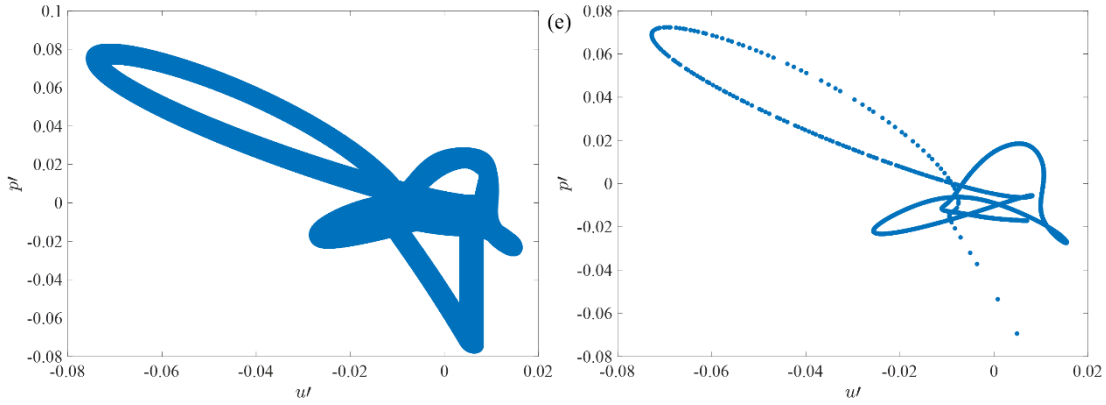
(e)
p′
u′

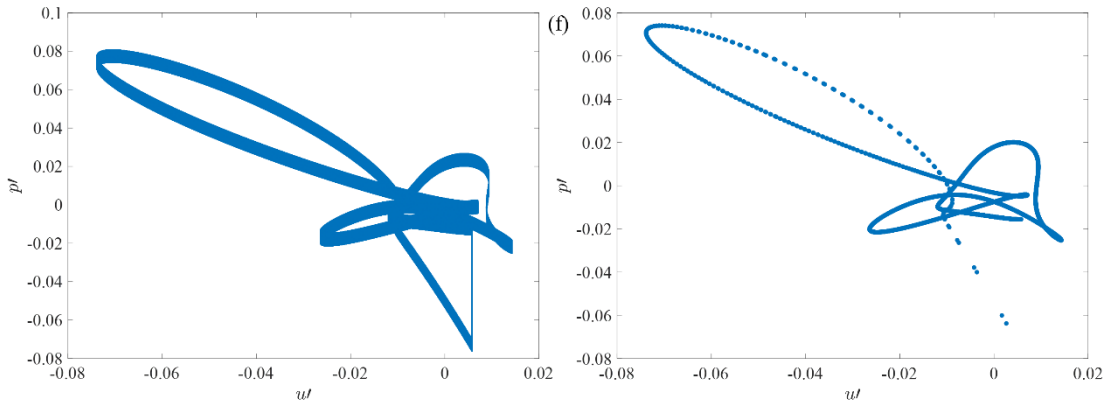
(f)
p′
u′

Fig. 6.6 The $p'-u'$ phase diagram at different f_e and the corresponding Poincaré section (f_e =(a)0.1, (b)0.5, (c)1, (d)1.5, (e)3, (f)5).

Next, the influences of the non-dimensional amplitude of sinusoidal excitation on the thermoacoustic system is studied. Fixed $f_e = 1.5$, $A = 0.05, 0.1, 0.5, 1, 1.5, 3$ respectively, the results in Fig. 6.7 can be obtained. Figure 6.7 shows the $u'-t$ series at different A. Comparing Fig. 6.7 (a) (b) with Fig. 6.4 (g), it can be seen that the amplitude of u' under these two amplitudes of excitation is slightly larger than that without excitation. While, comparing Fig. 6.7 (c)-(f) with Fig. 6.4 (g), it can be seen that the amplitude of u' under these four amplitudes of excitation is obviously larger than that without excitation, and the thermoacoustic oscillation is enhanced under these four amplitudes of excitation. And the amplitude of thermoacoustic oscillation increases with the increase of the amplitude of excitation.

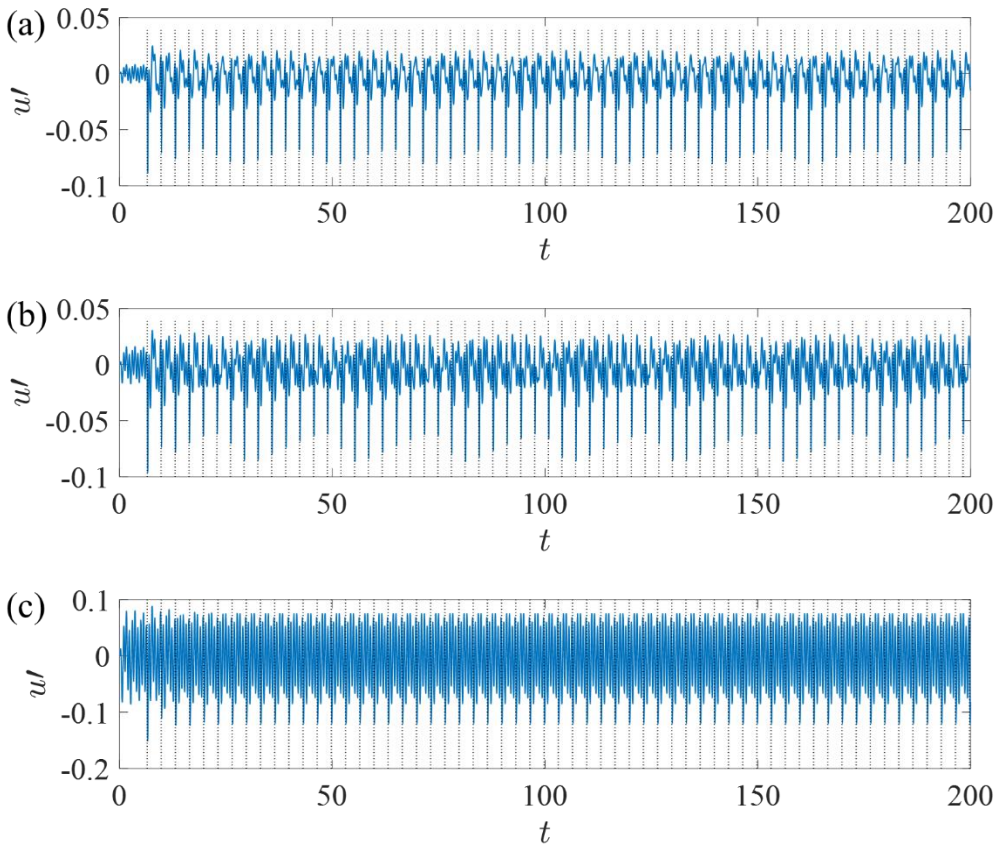

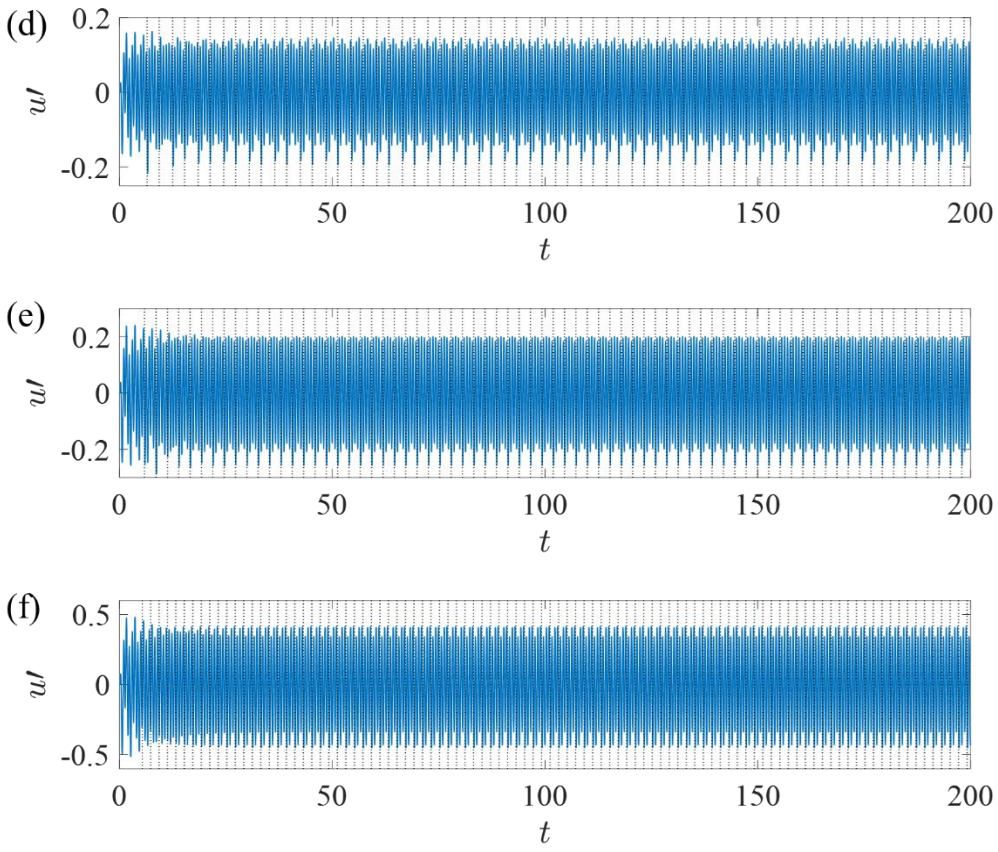

Fig. 6.7 The $u'-t$ series at different A (A =(a)0.05, (b)0.1, (c)0.5, (d)1, (e)1.5, (f)3).

Figure 6.8 shows the $p'-u'$ phase diagram at different A, at $f_e = 1.5$ and the corresponding Poincaré section. In Fig. 6.8, the pictures on the left is the $p'-u'$ phase diagram, and the pictures on the right is the Poincaré section, which is taken at intervals of $1/f_e$. In Fig. 6.8 (a) and (b), with the increase of time, the points on the Poincaré section will eventually form a closed curve, which indicates that the system of thermoacoustic oscillation has a quasi-periodic solution. While in Fig. 6.8 (c)-(f), with the increase of time, there are finite points on the Poincaré section, which indicates that the system of thermoacoustic oscillation has periodic solution. It can be seen from Fig. 6.8 that the system changes from quasi-periodic oscillation to periodic oscillation, with the increase of the amplitude of excitation.

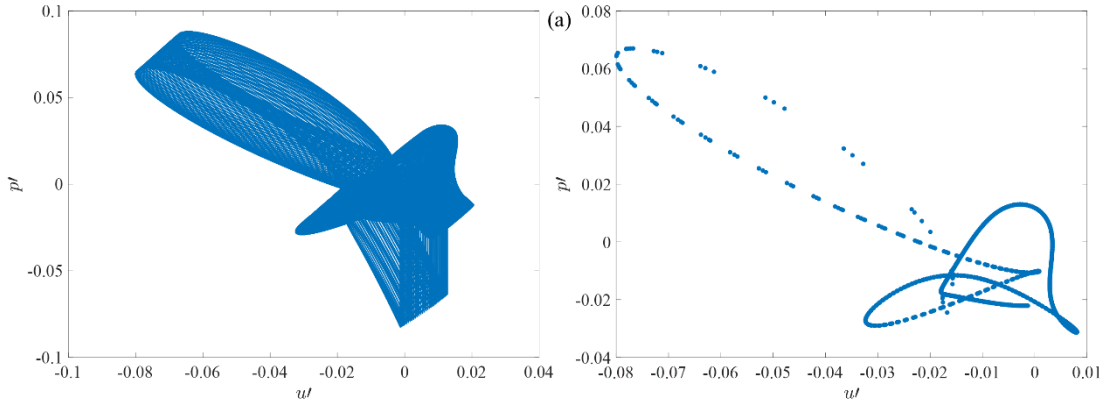
(a)
p′
u′

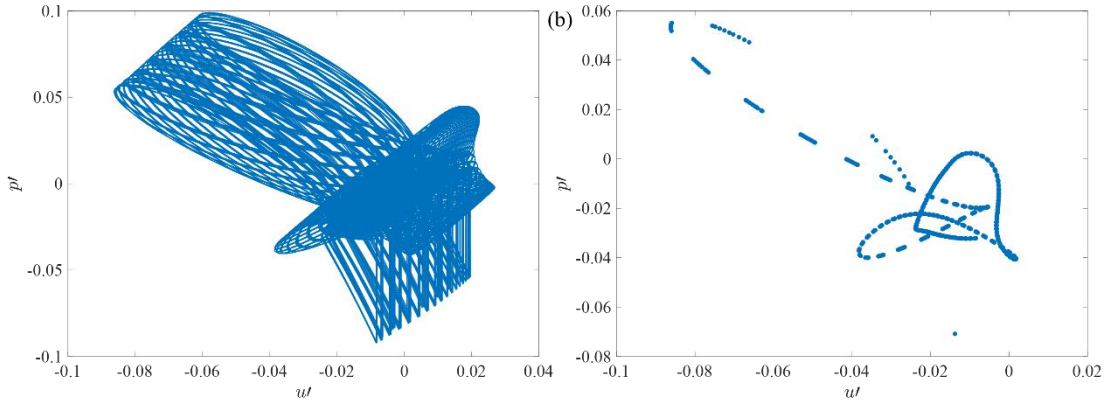
(b)
p′
u′

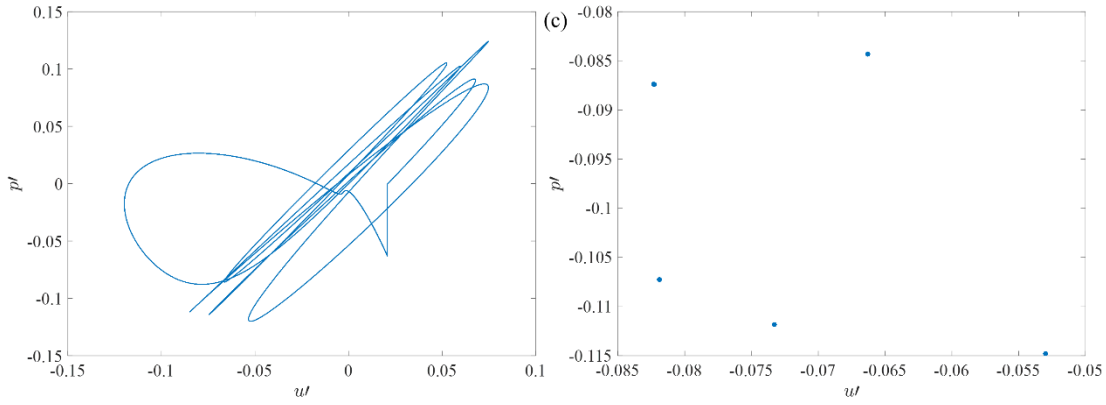
(c)
p′
u′

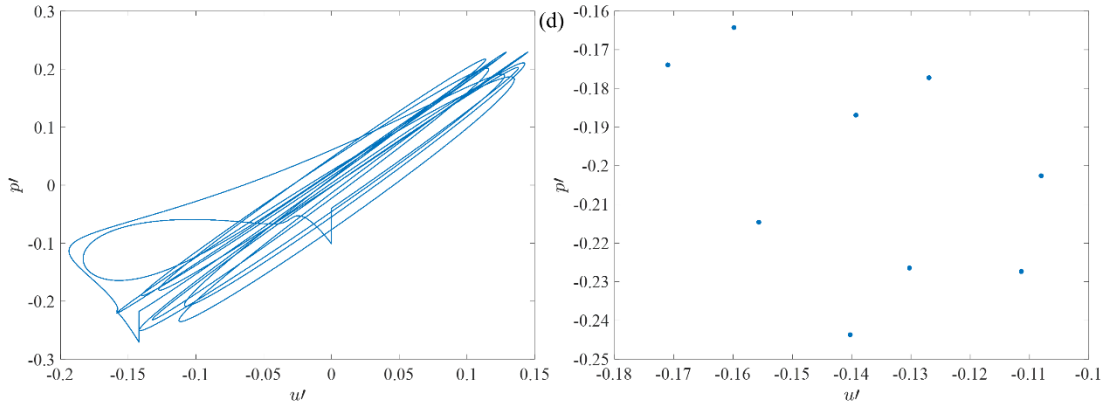
(d)
p′
u′

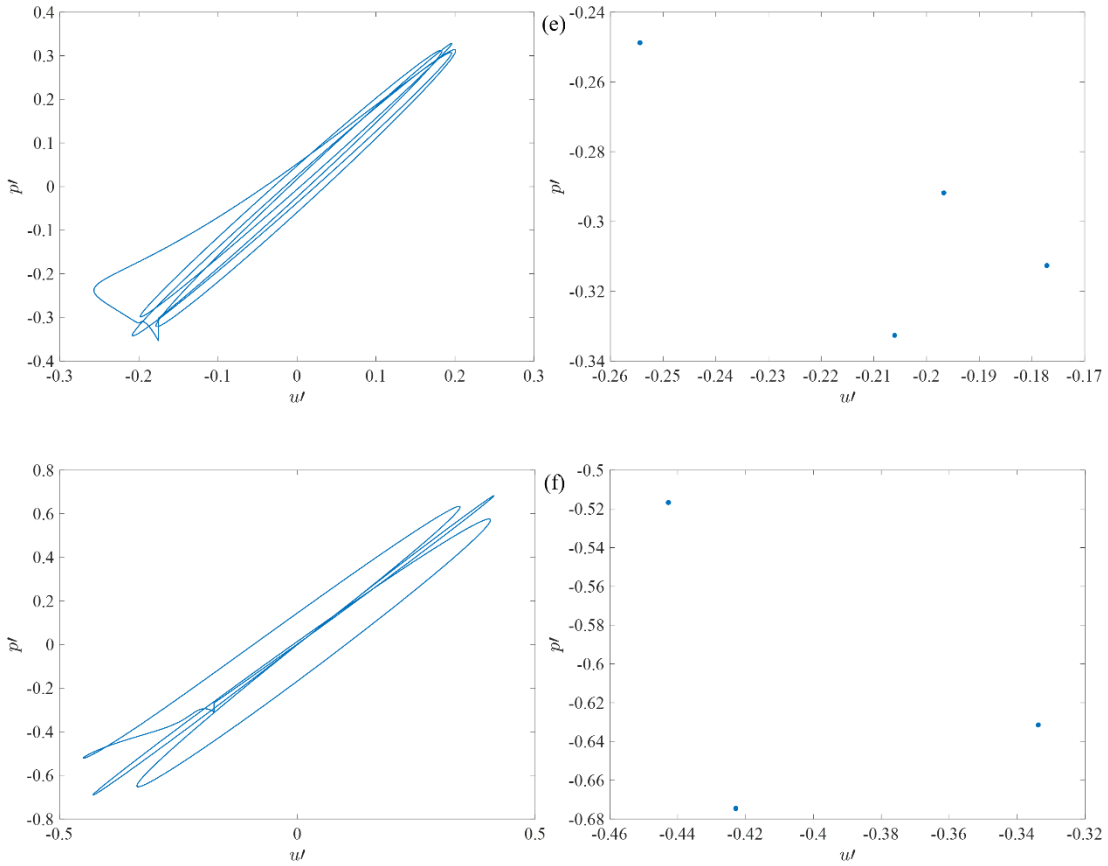

Fig. 6.8 The $p'-u'$ phase diagram at different A and the corresponding Poincaré section (A =(a)0.05, (b)0.1, (c)0.5, (d)1, (e)1.5, (f)3).

Fixed $f_e = 5$, $A = 0.05, 0.1, 0.5, 1, 1.5, 3$ respectively, the results in Fig. 6.9 can be obtained. Figure 6.9 shows the $u'-t$ series and $p'-t$ series at different A. Comparing Fig. 6.9 with Fig. 6.4 (g), it can be seen that the frequency of vortex shedding is almost constant with the change of amplitude A, at this frequency $f_e = 5$. Interestingly, it can be seen that the amplitude of u' under these amplitudes of excitation (A) is almost the same as that without excitation. While, the amplitude and of frequency of p' increases with the increase of the amplitude of excitation.

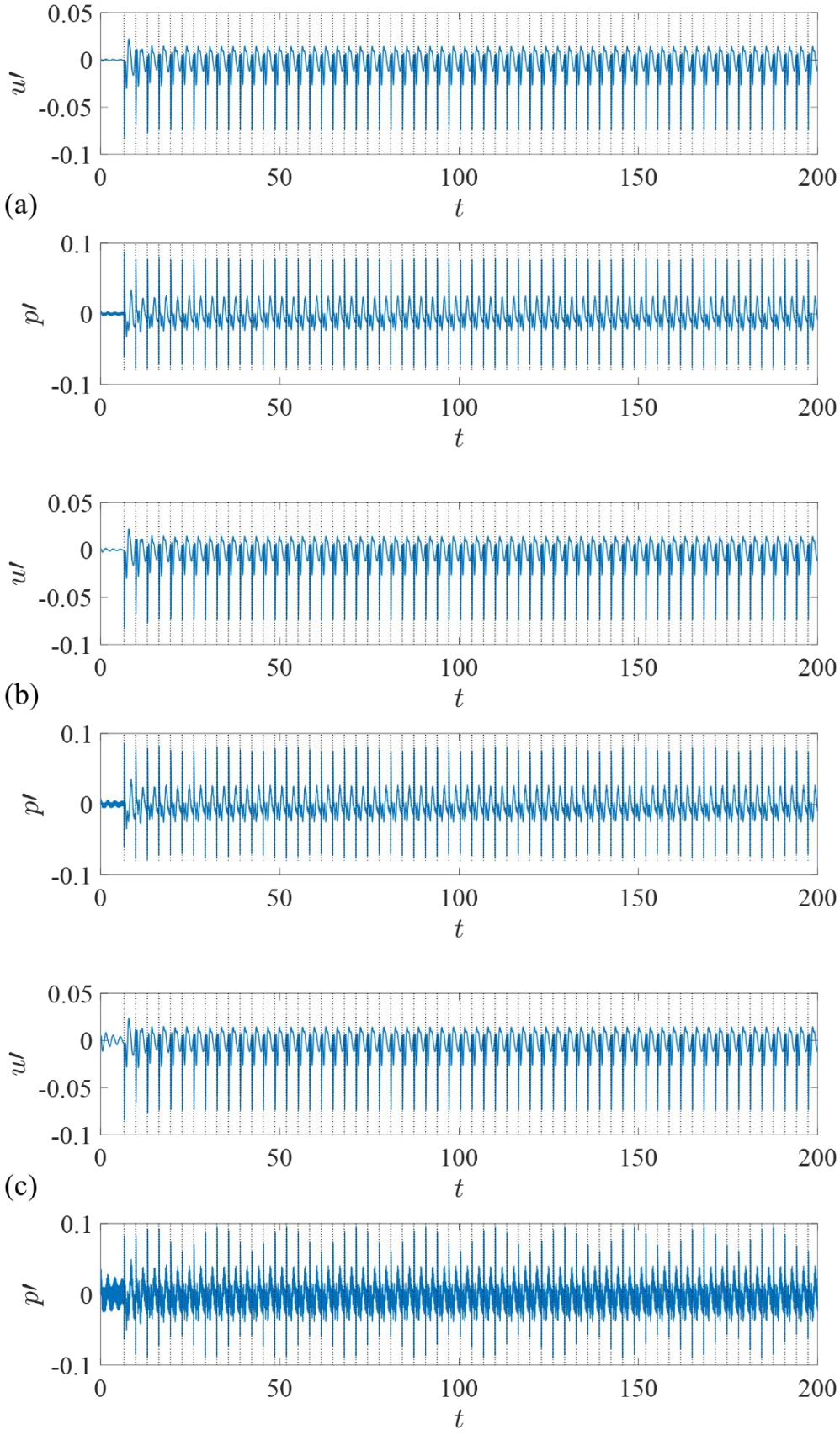
0.05
0
-0.05
-0.1
u′
0
50
100
150
200
t
(a)
0.1
0
-0.1
p′
0
50
100
150
200
t
0.05
0
-0.05
-0.1
u′
0
50
100
150
200
t
(b)
0.1
0
-0.1
p′
0
50
100
150
200
t
0.05
0
-0.05
-0.1
u′
0
50
100
150
200
t
(c)
0.1
0
-0.1
p′
0
50
100
150
200
t

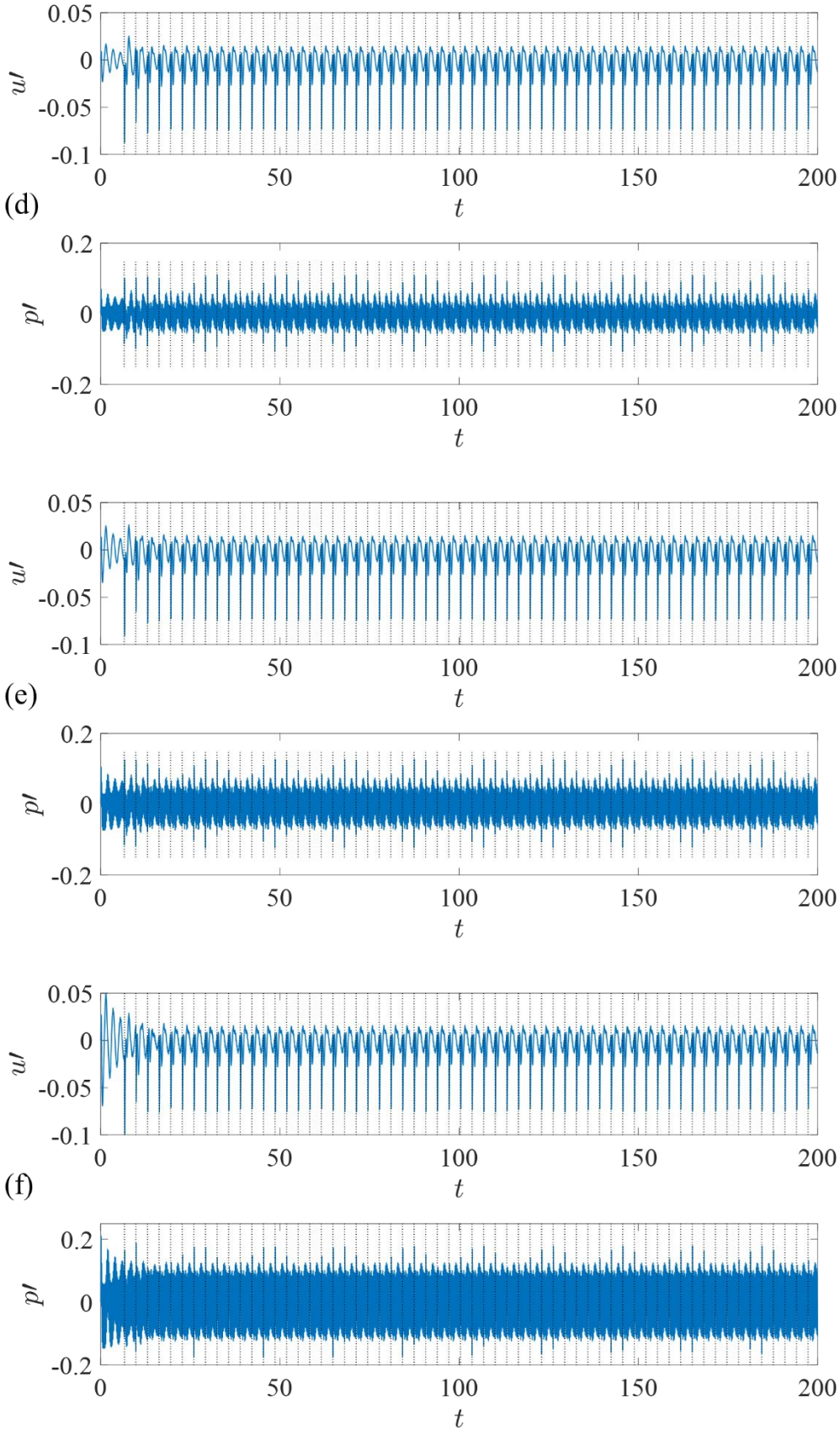

Fig. 6.9 The $u' - t$ series and $p' - t$ series at different A (A =(a)0.05, (b)0.1, (c)0.5, (d)1, (e)1.5, (f)3).

Figure 6.10 shows the $p'-u'$ phase diagram under different A, at $f_e=5$ and the corresponding Poincaré section. In Fig. 6.10, the pictures on the left is the $p'-u'$ phase diagram, and the pictures on the right is the Poincaré section, which is taken at intervals of $1/f_e$. In Fig. 6.10, with the increase of time, the points on the Poincaré section will eventually form a closed curve, which indicates that the system of thermoacoustic oscillation has a quasi-periodic solution. It can be seen that the system is always quasi-periodic oscillation, with the increase of the amplitude of excitation. But the width of the torus in the $p'-u'$ phase diagram increases, as the amplitude of excitation increases.

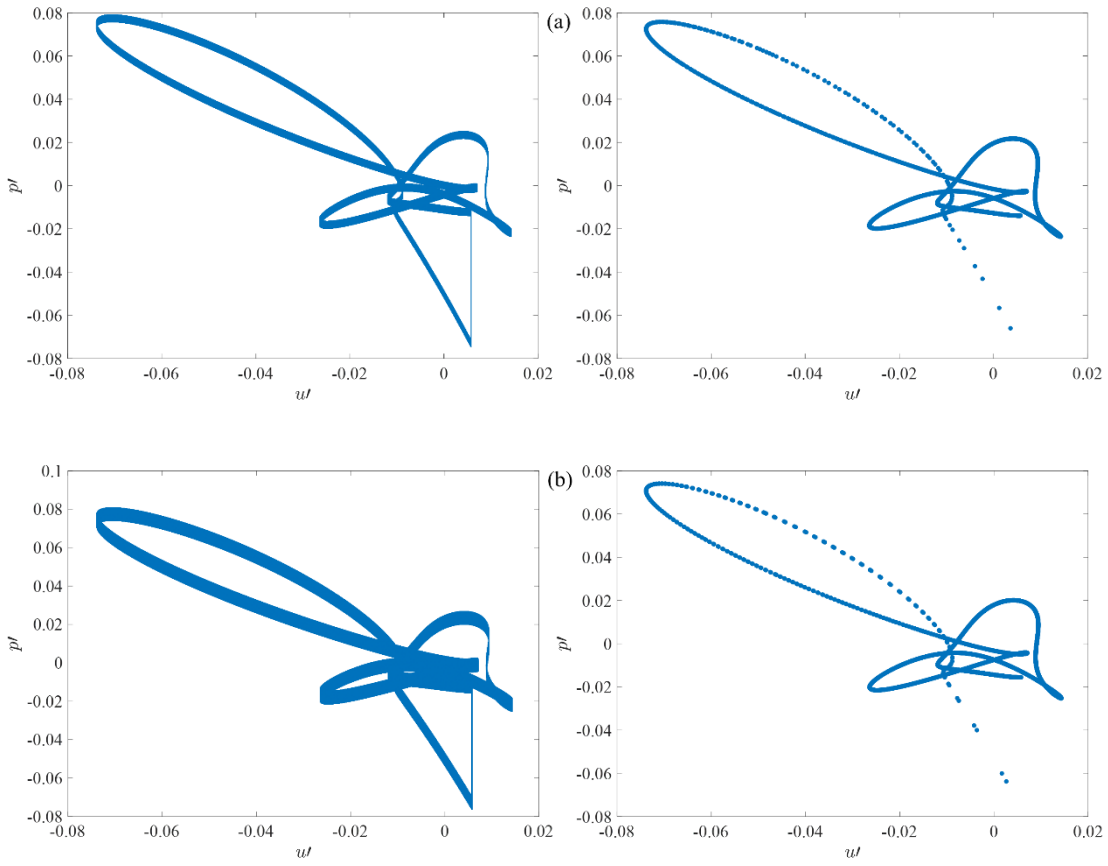

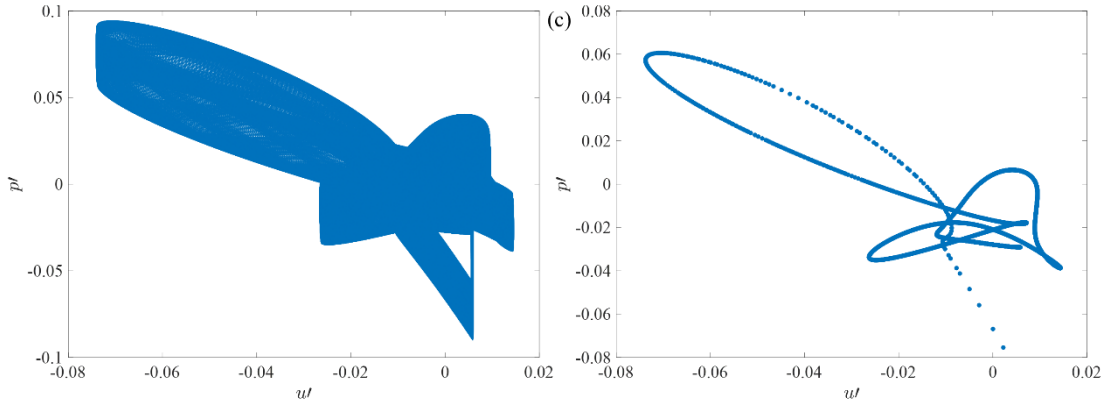
(c)
p′
u′

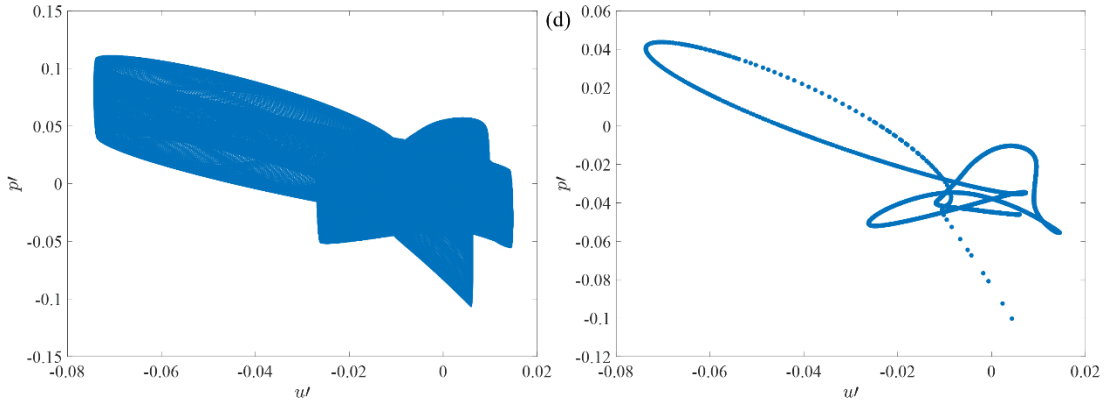
(d)
p′
u′

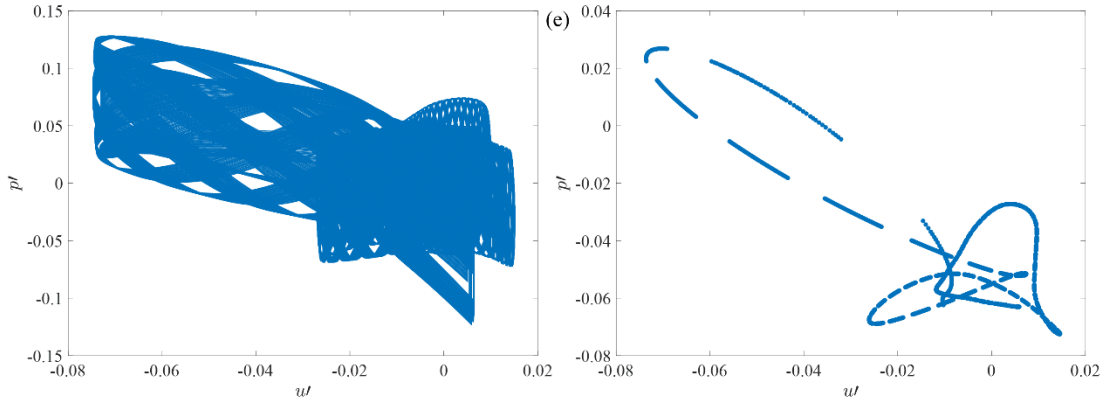
(e)
p′
u′

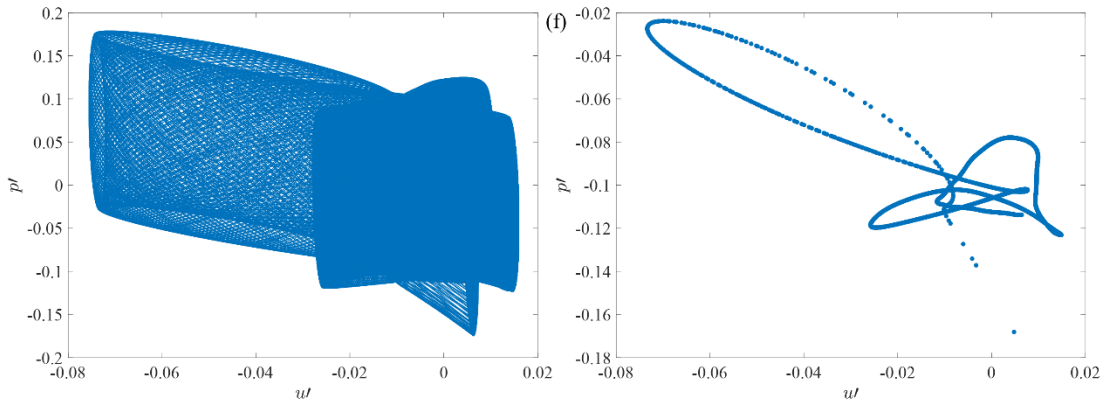
(f)
p′
u′

Fig. 6.10 The $p' - u'$ phase diagram at different A and the corresponding Poincaré section (A =(a)0.05, (b)0.1, (c)0.5, (d)1, (e)1.5, (f)3).

The influences of the amplitude and frequency of sinusoidal excitation on the thermoacoustic system is preliminarily studied in this section. Further research is needed in the future.

Chapter 7 Conclusions

Based on the thermoacoustic model involving vortex shedding proposed by Matveev and Culick, the vortex shedding model is introduced to establish the governing equations of thermoacoustic oscillation. Then, the governing equations are reduced to a series of ordinary differential equations by Galerkin method and solved numerically. The pressure and velocity fluctuations of the acoustic field are obtained. The influence of u_0 on the thermoacoustic oscillation of the system and the vortex-acoustic lock-in behavior in the thermoacoustic oscillation are studied in detail. Furthermore, the influences of fluctuation of upstream velocity in combustor on the thermoacoustic oscillation is studied. Besides, the influences of external harmonic excitation on the thermoacoustic system is also studied. The main conclusions of this study have been drawn as follows,

(1) The thermoacoustic oscillation system involving vortex shedding is very sensitive to the initial conditions and is a typical nonlinear dynamic system. The slight difference of initial perturbation leads to different nonlinear effects, and the system presents multi-solution characteristics.

(2) As u_0 increases, the frequency of steady vortex shedding (f_{s0}) increases, but the amplitude of pressure fluctuation does not necessarily increase continuously. With the increase of u_0, the circulation of shedding vortex and the intensity of heat release increase, and the amplitude of pressure fluctuation generally increases. However, the amplitude of pressure fluctuation repeats a similar structure that first decreases and then increases in each small region during the change of u_0.The phase difference between the moment of vortex impact and combustion and the pressure fluctuation affects the change of amplitude. At the maximum point of the change of amplitude, the vortex impact and combustion occurs at the peak of pressure oscillation, which strengthens the oscillation and is in agreement with Rayleigh's criterion.

(3) The thermoacoustic oscillation of the model under different u_0 presents the

phenomenon of vortex-acoustic frequency lock-in. Finally, the thermoacoustic system will oscillate periodically by integer (f_p/f_s) multiple of the frequency (f_s) of the vortex impinging, that is, the frequency lock-in with the number of revolutions f_p/f_s. In this study, a triangle region of vortex-acoustic frequency lock-in with f_s/f_p of 1, 1/2, 1/3, 1/4, 1/5, 1/6, 1/7 and 1/8 is formed. This phenomenon can be regarded as an important feature of periodic combustion oscillation.

(4) When the frequency of fluctuating mainstream velocity is a positive integer multiple of the frequency of steady vortex shedding, the actual frequency of vortex shedding is strictly equal to the frequency of steady vortex shedding, and the segmented frequency-locked region appears near the frequency. In each frequency-locked region, the frequency of vortex shedding strictly monotonically increases with the increase of the frequency of fluctuating mainstream velocity, while the frequency of vortex shedding almost does not change between the frequency-locked regions.

(5) The thermoacoustic oscillation of the system can be controlled by the fluctuation of mainstream velocity. When the frequency of fluctuating mainstream velocity is positive integer times of the frequency of steady vortex shedding, the intensity of the thermoacoustic oscillation is significantly weaker than that when the mainstream velocity is stable. If the frequency of fluctuating mainstream velocity is greater than the multiple frequency of the frequency of steady vortex shedding, and is in the frequency–locked region, the amplitude of thermoacoustic oscillation will be further decreased. As the frequency of fluctuating mainstream velocity develops towards high frequency, the frequency-locked region becomes wider and wider, and the higher frequency of fluctuating mainstream velocity in frequency-locked region is more likely to reduce the amplitude of thermoacoustic oscillation.

(6) The thermoacoustic oscillation of the system has periodic and quasi-periodic solutions under external sinusoidal excitation. The thermoacoustic oscillation of the system can be controlled by choosing the frequency and amplitude of the external excitation reasonably.

References

[1] Zinn B T, Lieuwen T C. Combustion Instabilities: Basic Concepts. Combustion Instabilities in Gas Turbine Engines: Operational Experience, Fundamental Mechanisms, and Modeling, 2005, 210: 3-26.

[2] Jacob E J. A Study of Nonlinear Combustion Instability. doctoral dissertations, 2009.

[3] Culick F E C. Combustion Instabilities in Liquid-fuelled Propulsion Systems. 1988.

[4] Rayleigh, J S W. The Theory of Sound. Vol. 2, Dover, New York, 1945.

[5] Annaswamy A M, Ghoniem A F. Active Control of Combustion Instability: Theory and Practice. IEEE Control Systems Magazine, 2002, 22(6): 37-54.

[6] Crocco L, Cheng S I. Theory of Combustion Instability in Liquid Propellant Rocket Motors. Butterworths Scientific Publications, London, 1956.

[7] Yang V, Kim S I, Culick F. Triggering of Longitudinal Pressure Oscillations in Combustion Chambers. I: Nonlinear Gasdynamics. Combustion Science and Technology, 1990, 72(4-6): 183-214.

[8] Josef, M, Wicker, et al. Triggering of Longitudinal Combustion Instabilities in Rocket Motors: Nonlinear Combustion Response. Journal of Propulsion and Power, 1996, 12(6): 1148-1158.

[9] Balasubramanian K, Sujith R I. Thermoacoustic Instability in a Rijke Tube: Non-normality and Nonlinearity. Physics of Fluids, 2008, 20: 044103.

[10] Subramanian P, Mariappan S, Sujith R I, et al. Bifurcation Analysis of Thermoacoustic Instability in a Horizontal Rijke Tube. International Journal of

Spray and Combustion Dynamics, 2010, 2(4): 325-356.

[11] Dang N N, Zhang Z Y, Zhang J Z. Stability Switching Behavior of Thermoacoustic Oscillation in Rijke Tube. Acta Physica Sinica, 2018, 67(13): 134301.

[12] Rogers D E, Marble F E. A Mechanism for High-Frequency Oscillation in Ramjet Combustors and Afterburners. Journal of Jet Propulsion, 1956, 26(6): 456-462.

[13] Hegde U G, Reuter D, Daniel B R, et al. Flame Driving of Longitudinal Instabilities in Dump Type Ramjet Combustors. Combustion Science and Technology, 1987, 55(4-6): 125-138.

[14] Poinsot T J, Trouve A C, Veynante D P, et al. Vortex-driven Acoustically Coupled Combustion Instabilities. Journal of Fluid Mechanics, 1987, 177: 265-292.

[15] Sterling J D, Zukoski E E. Nonlinear Dynamics of Laboratory Combustor Pressure Oscillations. Combustion Science and Technology, 1991, 77(4-6): 225-238.

[16] Cohen J, Anderson T. Experimental Investigation of Near-blowout Instabilities in a Lean, Premixed Step Combustor. 34th Aerospace Sciences Meeting and Exhibit, Reno, January 15−18, 1996, p819.

[17] Speth R L, Altay H M, Hudgins D E, et al. Vortex-driven Combustion Instabilities in Step and Swirl-stabilized Combustors. 46th AIAA Aerospace Sciences Meeting and Exhibit, Reno, Nevada, January 7–10, 2008, p1053.

[18] Bauwens L, Daily J W. Flame Sheet Algorithm for Use in Numerical Modeling of Ramjet Combustion Instability. Journal of Propulsion and Power, 1992, 8(2): 264-270.

[19] Najm H N, Ghoniem A R. Modeling Pulsating Combustion Due to Flow-Flame Interactions in Vortex-stabilized Pre-mixed Flames. Combustion Science and

Technology, 1993, 94(1-6): 259-278.

[20] Menon S, Jou W H. Large-eddy Simulations of Combustion Instability in an Axisymmetric Ramjet Combustor. Combustion Science and Technology, 1991, 75(1-3): 53-72.

[21] Angelberger C, Veynante D, Egolfopoulos F. LES of Chemical and Acoustic Forcing of a Premixed Dump Combustor. Flow Turbulence and Combustion, 2000, 65: 205-222.

[22] Wan S W, He G Q, Shi L. Large Eddy Simulation of Active Control on Low Frequency Combustion Instabilities in a Dump Combustor. Journal of Solid Rocket Technology, 2011, 34(1): 32-37.

[23] Matveev K I, Culick F E C. A Model for Combustion Instability Involving Vortex Shedding. Combustion Science and Technology, 2003, 175(6): 1059-1083.

[24] Tulsyan B, Balasubramanian K, Sujith R I. Revisiting a Model for Combustion Instability Involving Vortex Shedding. Combustion Science and Technology, 2003, 181(3): 457-482.

[25] Matveev K I. A Model for Acoustic Instabilities Induced by Vortex Shedding in Ducts. ASME 2003 International Mechanical Engineering Congress and Exposition Washington, DC, November 15−21, 2003, p119.

[26] Nair V, Sujith R I. A Reduced-order Model for the Onset of Combustion Instability: Physical Mechanisms for Intermittency and Precursors. Proceedings of the Combustion Institute, 2015, 35(3): 3193-3200.

[27] Seshadri A, Nair V, Sujith R I. A Reduced-order Deterministic Model Describing an Intermittency Route to Combustion Instability. Combustion Theory and Modelling, 2016, 20(3): 441-456.

[28] Singaravelu B, Mariappan S. Stability Analysis of Thermoacoustic Interactions in Vortex Shedding Combustors Using Poincaré Map. Journal of Fluid Mechanics, 2016, 801: 597-622.

[29] Singaravelu B, Mariappan S. Criterion for Vortex Acoustic Lock-on in Combustors with Backward Facing Step. Fifteenth Asian Congress of Fluid Mechanics Kuching, November 21–23, 2017, p12.

[30] Chakravarthy S R, Sivakumar R, Shreenivasan O J. Vortex-acoustic Lock-on in Bluff-body and Backward-facing Step Combustors. Sadhana, 2007, 32(1-2): 145-154.

[31] Kaplan D, Glass L. Understanding Nonlinear Dynamics. Springer Science & Business Media, 1997.

[32] Hirsch M W, Smale S, Devaney R L. Differential Equations, Dynamical Systems, and an Introduction to Chaos. Academic press, 2012.

[33] Thompson J M T, Stewart H B. Nonlinear Dynamics and Chaos. John Wiley & Sons, 2002.

[34] Strogatz S H. Nonlinear Dynamics and Chaos with Student Solutions Manual: With Applications to Physics, Biology, Chemistry, and Engineering. CRC press, 2018.

[35] Guckenheimer J, Holmes P. Nonlinear Oscillations, Dynamical Systems, and Bifurcations of Vector Fields. Springer Science & Business Media, 2013.

[36] Heckl M A. Nonlinear Acoustic Effects in the Rijke Tube. Acta Acustica united with Acustica, 1990, 72(1): 63-71.

[37] Dotson K W, Koshigoe S, Pace K K. Vortex Shedding in a Large Solid Rocket Motor Without Inhibitors at the Segment Interfaces. Journal of Propulsion and

Power, 1997, 13(2): 197-206.

[38] Sterling J D, Zukoski E E. Nonlinear Dynamics of Laboratory Combustor Pressure Oscillations. Combustion science and technology, 1991, 77(4-6): 225-238.

[39] Chakravarthy S R, Shreenivasan O J, Boehm B, et al. Experimental Characterization of Onset of Acoustic Instability in a Nonpremixed Half-dump Combustor. The Journal of the Acoustical Society of America, 2007, 122(1): 120-127.

[40] Kashinath K, Waugh IC, Juniper MP. Nonlinear Self-excited Thermoacoustic Oscillations of a Ducted Premixed Flame: Bifurcations and Routes to Chaos. Journal of Fluid Mechanics, 2014, 761: 399-430.

[41] Kashinath K, Li LKB, Juniper MP. Forced Synchronization of Periodic and Aperiodic Thermoacoustic Oscillations: Lock-in, Bifurcations and Open-loop Control. Journal of Fluid Mechanics, 2018, 838: 690-714.

[42] Gopalakrishnan E, Sujith R. Effect of External Noise on the Hysteresis Characteristics of a Thermoacoustic System. Journal of Fluid Mechanics, 2015, 776:334-353.

Acknowledgments

I am very grateful to everyone who has helped me in the past four years for successfully finishing this dissertation and graduating on time. My deepest gratitude goes foremost to the professors including Prof. Deguchi, my supervisor in Tokushima University, and Prof. Zhang, my supervisor in Xi'an Jiaotong University for their constant encouragement and guidance at all the time. I am also very grateful to the members of our laboratory and the staff of Tokushima University, especially Muramoto san, Kamimoto san and Asada san. During my study in Japan, they gave me a lot of help in my study and life. And I am also great thanks to my parents for their support all the time. Finally, I am deeply grateful to my motherland.